LASER FABRICATION OF HIGH-K DIELECTRICS FOR HIGH CURRENT CATHODES

by

Nicholas Michael Carl Jordan

A dissertation submitted in partial fulfillment
of the requirements for the degree of
Doctor of Philosophy
(Nuclear Engineering and Radiological Sciences)
in the University of Michigan
2008

Doctoral Committee:

Professor Ronald M. Gilgenbach, Co-Chair
Professor Yue Y. Lau, Co-Chair
Associate Professor John E. Foster
Assistant Professor Jamie D. Phillips

To all those loved and lost.

ACKNOWLEDGEMENTS

I would like to begin by thanking Professor Gilgenbach and Professor Lau. I stumbled into graduate school without doing any research into how to pick a school, project, or advisor, and I was extremely fortunate to end up where I am now. As I went through school and listened to other students (at U of M and elsewhere) lament their graduate school experience, I realized just how lucky I was. I didn't apply anywhere except the plasma group at Michigan, and if could do it all over again I would do exactly the same thing.

We are blessed to have both a top-tier theorist and top-tier experimentalist to guide us. And as an added bonus for the experimental guys, Professor Lau writes up theories that we can (usually) understand. His ability to quickly solve complex problems from first principles will never cease to amaze me. I think it's best summarized by a conversation I had at an interview, where the interviewer asked me if I liked to do theory or experiment. I asked if he meant simulation-type theory or "Professor Lau-type" theory. He just laughed and said that no one is able to do "Professor Lau-type" theory.

Prof. G's style of mentorship let me develop the ability to direct my research, while always giving me someone to ask if I didn't know which direction to go. Even when I had no idea what I was doing, he always made me feel like I had the ability to get it done. I also don't think there is anyone more dedicated to taking care of his students. We don't have to spend time and energy worrying if we'll have to teach a class for funding, and his "lifetime job placement service" is equally helpful.

On that topic I can't say enough good things about the support Prof. G and Prof. Lau have given me. I naively believed that what you know is more important in a job search than who you know, and I've just been very fortunate to

know these two people. The employment assistance they have both provided, not only to me but to Kat as well, has been above and beyond anything I could have asked for.

My other committee members, Professor Foster and Professor Phillips, also deserve many thanks for the help they've given me, particularly towards the end of this long Ph.D. journey. I appreciate the constructive criticism, and many insightful discussions on semiconductors and plasma processing. In particular, all the discussions of semiconductors and thin films were very helpful, as that is not an area our group is familiar with, and often helped me realize just how much I still need to learn about that subject.

I would also like to thank the many grad students I've worked with here at U of M, both past and present. The fact that I use Mike Jones' thesis as a reference manual sums up how instrumental he was in getting me started in grad school. I don't think I will ever meet a nicer guy than Will White, and I hope our paths cross again sometime in the future. I also appreciate the spectroscopic help from Mark Johnston, the laser and optics help from Trevor Strickler, and the fact that there are still a few Bogdan heads stuck to our ceiling. Yoshi Hidaka also deserves great thanks for answering my incessant plasma physics questions, and teaching me everything I know about Japan and Japanese culture.

I'd like to also thank Matt Gomez and Jake Zier for stealing my optical cleaning solution (I know you have it), forcing me to upgrade to something that would actually clean them. Without Brad Hoff leading the current generation of MELBA runs, I doubt my thesis would even have been possible. Your microwave expertise is greatly appreciated, as is all the time spent running these cathodes. While I've only worked with Dave French for a year, he already has helped me out quite a bit. I'm not sure I would have made it through those 12 hour spectroscopy runs without you. The labs laser systems couldn't be in better hands. Another important member of our lab, Mark Perrault, also deserves many thanks for all the work he does to keep the lab running smoothly on a day-to-day basis.

The fact that I am even writing this thesis is a huge testament to the support my family has given me my entire life. I owe every aspect of who I am now to the way you've raised me, and I'm extremely thankful that I will always be someone who looks forward to family gatherings. In particular, mom and grandmas, thank you for all the sacrifices you made to give me a head start in life. There is no doubt in my mind that grandma daycare is the best childhood a kid could have. Mom, it's taken me a long time to realize how hard it must have been to raise us while working a full-time job. You always made it look so easy that we just took it for granted, but I have the utmost respect for what you've accomplished.

The highlight of my graduate career was undoubtedly when I took NERS 571. With all due respect to Landau Damping and line integrals, meeting my wife, Kat, will always be the most memorable part of plasma theory. There are so many things to thank you for, but most of all, thank you for just being who you are. I never dreamed I would find someone with all the wonderful qualities you possess, and I look forward to living out the rest of my years at your side.

I would also like to thank all of the sponsors of this work. I was supported by an Applied Materials graduate fellowship, American Nuclear Society graduate scholarships, and funding from the Air Force Office of Scientific Research and the AFOSR- Multi-University Research Initiative (AFOSR-MURI). Additional research funding was also received from L-3 Communications, Northrop Grumman Corp. and Air Force Research Labs. I owe great thanks to these organizations for giving me an opportunity to finish college with no student loans to repay.

TABLE OF CONTENTS

LIST OF FIGURES

LIST OF TABLES

LIST OF APPENDICES

LIST OF ABBREVIATIONS

AFRL	Air Force Research Laboratory
ALF	ablation line focused
BLUE	filing name for magnet current data from magnetron tests
BNC	Berkeley Nucleonics Corporation
C-L	Child-Langmuir
C-V	capacitance-voltage
CCD	charge-coupled device
CKE	copper knife edge
DC	direct current
DiCoat	dielectric coated
EHF	extra high frequency
ELF	extra low frequency
EMAL	University of Michigan Electron Microbeam Analysis Laboratory
ENTC	filing name for MELBA entrance current data
FEA	field emitter array
HPM	high power microwaves
ICCD	intensified CCD
IED	improvised explosive device
MELBA-C	Michigan Electron Long Beam Accelerator - Ceramic
MIO	metal island only
MOJ	metal oxide junction
MPOV	filing name for microwave power data from the “V” waveguide of the magnetron
MPOX	filing name for microwave power data from the “X” waveguide of the magnetron
MPOW	filing name for microwave power data from the “W” waveguide of the magnetron
NIST	National Institute of Standards and Technology
PAL	projection ablation lithography
PEAR	filing name for endloss current data, measured by a Pearson coil
PI	Princeton Instruments
PSI	Pulse Sciences International (now L-3 Comm. PSI)
PSS	polished stainless steel
RF	radio frequency
RPM	revolutions per minute
SCL	space charge limited
SEE	secondary electron emission
SEM	scanning electron microscopy

TFA	time-frequency analysis
TWT	traveling wave tube
UM	University of Michigan
UV	ultraviolet
VOLN	filing name for MELBA voltage data
XEDS	x-ray energy dispersive spectroscopy
XRD	x-ray diffraction

CHAPTER 1
INTRODUCTION

The radio frequency (RF) spectrum spans 11 orders of magnitude, from Extra Low Frequency (ELF) at 3 Hz, to Extra High Frequency (EHF) at 300 GHz [NTIA]. Microwave radiation occupies the upper third of this spectrum, from 300 MHz to 300 GHz [Poz98], and is produced by a myriad of devices, including gyrotrons, klystrons, traveling wave tubes, and magnetrons. The uses for this radiation are even more numerous, ranging from the mundane task of reheating leftovers, to the mission-critical detection of enemy aircraft with radar. The microwave regime above 100 MW peak power is typically dubbed “high power microwaves” (HPM), and extends into peak powers as high as 15 GW [Ben07].

1.1 HPM Applications

An active area of research on HPM is the development of sources for directed energy applications. The remote neutralization or detonation of improvised explosive devices (IEDs), is another application currently in development. In a similar effort, HPM devices have been deployed to jam and predetonate proximity-fused munitions. These shells are fused to detonate at a specific distance from their target, and can be triggered by an appropriate microwave signal. To protect aircraft against surface-to-air missiles during takeoff and landing, another HPM system, dubbed Vigilant Eagle, is being developed for ground-based deployment at airports [Ben07]. Outside the realm of directed energy, HPM devices are also used for power beaming [Nal78], space propulsion [Par04], and plasma heating applications [Pra04].

Within the HPM arena, relativistic magnetrons are among the most mature, tunable, and robust devices available. Currently capable of efficiencies

approaching 30%, relativistic magnetron simulations [Lem99, Lem00] have shown that they are theoretically capable of 55% efficiencies, far from the 80+% efficiencies of conventional magnetrons, but still a high efficiency HPM source [Ben07]. Additionally, relativistic magnetrons have high average power (1 GW peak, 6 kW average), an important advantage for certain applications.

Pulse shortening is a common problem among HPM devices, and is one of the causes of their reduced energy efficiency. While voltage sources with microsecond pulse length are available, they still only generate microwave pulses 100's of ns in length. If the microwave pulse is short compared with the voltage pulse, one method of increasing the efficiency is to induce microwave oscillation earlier in the applied voltage. This can be done by a variety of methods, including cathode priming [Jon04a], microwave priming [Nec05, Pen05, Whi05], and magnetic priming [Hof07, Jon04b, Nec03]. Among other cathode developments, this thesis will present another form of cathode priming.

1.2 Electron Emission Mechanisms

One of the most important components of a relativistic magnetron is the cathode, the electron source. Current is emitted radially from a cylindrical cathode, by a combination of many emission processes. We review here the mechanisms of electron emission from thermionic, field emission, explosive emission, and secondary electron cathodes.

1.2.1 Thermionic Cathodes

Thermionic, or "hot," cathodes are heated to cause thermionic emission, according to the Richardson-Dushman equation:

$$j\left[A/cm^2\right] \cong 120T^2 \exp\left(-\frac{e\phi_w}{k_B T}\right) \tag{1.1}$$

where T is the temperature in °K, k_B is Boltzmann's constant, and ϕ_w is the work function [Ric23]. Cathodes may be resistively heated by passing current through the cathode, or can be heated directly by an external e-beam [Her87] or laser

source [Bar01]. Resistive heating may occur in the University of Michigan (UM)/Titan magnetron if large currents are drawn through thin metal filaments on the cathode surface [Jon05].

1.2.2 Field Emission Cathodes

Field emission, or "cold," cathodes rely on electron tunneling at sufficiently high surface electric fields. Their emission is governed by the Fowler-Nordheim equation:

$$J\left[A/cm^2\right] = A_{FN}\left(\frac{\beta V}{D}\right)^2 \exp\left[-\frac{B_{FN} D}{\beta V}\right]$$
$$A_{FN} = \frac{1.4\times10^{-6}}{\phi}\exp\left[\frac{9.87}{\sqrt{\phi}}\right] \qquad B_{FN} = 6.53\times10^{-7}\sqrt{\phi} \tag{1.2}$$

where ϕ is the work function in eV, *D* is the gap in cm, *V* is the voltage in Volts, and β is the field enhancement factor.

The fields are often enhanced by surface geometry or composition, and that enhancement is represented by β in Eqn. (1.2). Work at UM by M. C. Jones used small surface ripples and ridges on the all-metal Projection Ablation Lithography (PAL) cathode to enhance field emission [Jon04c]. A refinement of this concept has been employed by J. Booske at the University of Wisconsin with the invention of the Copper-Knife-Edge (CKE) cathode [He07]. Experiments with the CKE cathode have carefully monitored the emission current to investigate predictive models of Fowler-Nordheim current density.

The cesium iodide coated carbon fiber cathode developed by D. A. Shiffler at Air Force Research Laboratory (AFRL), utilizes both the geometric field enhancement of its narrow carbon fibers and the reduced work function of its CsI coating to stimulate electron emission. Tests of this cathode in a planar diode have yielded improved reproducibility and uniformity, low plasma generation, and no decrease in durability (compared to uncoated carbon fiber cathodes) [Shi00, Shi01a, Shi01b, Shi02a, Shi02b, Shi04a, Shi04b, Shi04c, Shi07].

Low-voltage Spindt field emitter arrays (FEAs) are a type of field emission cathode which has been pursued with great interest in recent years [Gam93]. Recent experiments with FEAs, by D. R. Whaley at L-3 Communications Electron Devices, have produced currents of up to 4 A/cm^2 at applied voltages of only 30 V. The resulting electron beam has been used to drive a traveling wave tube (TWT), producing 18 W of RF power at 4.1 GHz with 13 dB gain and 16.7% circuit efficiency [Wha07].

1.2.3 Explosive Emission Plasma Cathodes

Similar to field emission cathodes, explosive emission plasma cathodes also require very high surface fields, as the cathode forms plasma through breakdown of gases, contaminants, or metallic microfibers on the cathode surface [Mil98]. Once plasma is formed, it will become the source of electrons, and will emit according to the Space Charge Limited (SCL) Child-Langmuir (C-L) law (for a cylindrical geometry):

$$I[A] \approx 14.68 \times 10^{-6} \frac{LV^{3/2}}{r_p \beta^2} \tag{1.3}$$

where L is the effective emission length, r_p is the anode radius, and β is a function of the anode radius and effective cathode radius [Lug96].

Perhaps the most ubiquitous explosive emission design consists of cotton fiber, velvet, or felt glued to the desired emission region of the cathode. These cathodes have good emission uniformity and produce current densities on the order of kA/cm^2, but are very susceptible to damage during operation [Adl85, Hin85].

1.2.4 Secondary Electron Emission Cathodes

Another electron emission mechanism of considerable interest to this work is secondary electron emission. Electrons striking the cathode have a chance to induce electron emission. For certain (material dependent) energy ranges, each electron striking the surface will, on average, result in the emission of more than one electron. A much more detailed review of this mechanism is presented in

Chapter 2. For a more comprehensive review of cathodes in general, see Ch. 9 of [Bar01].

1.3 Scope of Thesis

This thesis will discuss cold cathodes for high power microwave applications in relativistic magnetrons. We will discuss both the Ablation Line Focused (ALF) cathode, designed with sharp surface features for field enhancement, and the Metal Oxide Junction (MOJ) cathode, designed for field enhancement at triple points (a metal-oxide-vacuum interface) and secondary electron emission.

In Chapter 2, we will begin with the theory of field enhancement and electron emission at triple points. We calculate the orbit of the first generation electrons, the seed electrons. It is found that, despite the mathematically divergent electric field at the triple point, significant electron yield most likely results from secondary electron emission when the seed electrons strike the dielectric. The analysis gives the voltage scale in which this electron multiplication may occur. It also provides an explanation on why certain dielectric angles are more favorable to electron generation over others, as observed in previous experiments.

Chapter 3 details the procedures used for fabrication of the ALF and MOJ cathodes. ALF cathodes are fabricated using a KrF excimer laser focused through a cylindrical lens to ablate lines of material from the aluminum or stainless steel cathode surface [Jon05]. A variation of this design, Tri-ALF, creates three distinct emission regions, with the cathode milled out in between and filled with carbon paint. MOJ cathodes use the KrF laser to ablate a hafnium target, creating a hafnium plasma plume, with a 100 mTorr O_2/Ar background. The plume deposits ions, neutrals, and particulate through a screen or mesh onto the cathode, forming dielectric “islands” on the cathode surface. The fabrication of control cathodes (polished stainless steel, dielectric coated, and metal-only) are also presented.

Chapter 4 discusses the experimental configurations used for plasma spectroscopy, as well as the major components of the accelerator and relativistic magnetron. An explanation of the diagnostics associated with cathode voltage, cathode current, magnetic field, and microwave power are also presented. Where applicable, the calibration procedures for these diagnostics are detailed.

Chapter 5 analyzes the cathode surfaces, with additional attention given to the hafnium oxide films used for MOJ cathodes, and a brief discussion of the plasma plumes generated during deposition. ALF cathodes are analyzed with mechanical profilometry, as well as scanning electron microscope (SEM) imaging. The hafnium oxide films are analyzed with SEM, X-ray Energy Dispersive Spectroscopy (XEDS), X-ray Diffraction (XRD), and profilometry. Additionally, film quality is examined through Capacitance-Voltage (C-V) testing.

The results of cathode tests on the UM/Titan relativistic magnetron are presented in Chapter 6. First, we compare the Tri-ALF cathode to ALF-2, its non-priming counterpart. These results focus largely on the microwave properties of the cathode, as improved microwave performance was the crux of its design. Next, we analyze data from the MOJ cathodes, focusing primarily on the emitted current and variations in the baseline results. Finally, we conclude with a summary and appendices in Chapter 7.

CHAPTER 2
ELECTRIC FIELD AND ELECTRON ORBITS NEAR A TRIPLE POINT

2.1 Introduction

The intersection between a metallic surface, a dielectric surface, and the vacuum region is generally known as a triple point [Mil95, Mes89, Bar01]. The triple point, in various settings, occurs naturally in all high voltage insulation systems, high power microwave windows, all oxide cathodes, and cold cathodes with adsorbed contaminants, etc. It has received renewed attention in recent research on novel cathode development [Ums05, Shi05, Jon05] and on RF window breakdown [Neu01, Edm06, Kim06]. In all of the above systems, the triple point has long been considered as the source where the first electrons are produced when a sufficiently strong electric field is present. The electric field at a mathematically sharp triple point could be infinite. This divergent electric field has often been considered to contribute to a significant "field-enhancement factor", leading to field emission of electrons [Ber77, And80, Sch98]. These first generation electrons, or seed electrons, once produced, may undergo rapid multiplication, either through impact ionization of neutrals [Gil86, Cun99], or through secondary emission if these seed electrons strike the dielectric surface with a sufficiently high energy [Vau93, Hac59]. Near the triple point, it has been speculated that "a single electron released from the cathode electrode can initiate a secondary emission avalanche" [And80].

Electron emission in the immediate vicinity of a triple point, under realistic conditions, is not easy to model. The work function is usually not accurately known. Neither is the electric field distribution, which depends not only on the

work function, but also on the local field enhancement factor, which itself may be strongly modified by the presence of space charge [Lug02, And94]. Each of these factors brings in tremendous uncertainties in the emission current density, as they all enter exponentially in the Fowler-Nordheim relation (for field emission [Fow28]) or the Richardson-Dushman-Schottky equation (for field-enhanced thermionic emission [Ric23]). Even numerical simulation of emission physics in an idealized geometry might be difficult [Mil07, Pet05]. The divergence of the electric field at the triple point requires demanding resolution in numerical simulation, which becomes particularly challenging when electron dynamics is included.

Bergeron [Ber77] considered the flashover mechanism that is initiated from the triple point of an insulator exposed to a high voltage. He concentrated mainly on the secondary electron emission in regions sufficiently far away from the triple point and, strickly speaking, he omitted the triple point altogether. Schachter [Sch98] considered electron emission from the metallic surface near a triple point according to the Fowler-Nordheim equation. He paid special attention to the local field enhancement factor, but omitted the electron dynamics altogether. Perhaps more significantly, he neglected the inevitable secondary electron emission on the dielectric that is concomitant to the specific geometry that he considered. Anderson and Brainard [And80] surveyed various scenarios of surface flashover mechanisms. They concentrated mainly on plasma formation on the dielectric surface which was assumed to be already positively charged to some significant degree. Thus, they paid little attention to the seed electrons. As we shall show in Section 2.5, the consideration of the seed electrons might explain why certain dielectric angles are more susceptible to flashover than others.

In this chapter, we examine the electric field in the immediate vicinity of the triple point. We also compute the electron trajectory subject to such an electric field. In particular, we consider the scale of the electric field, and the impact energy of the electron onto the dielectric, so that a seed electron is likely to initiate multiplication of electrons by secondary emission [Vau93, Hac59]. We

pay close attention to the mathematically divergent electric field at the triple point, in particular to a distance of order microns, or less, from the singularity. Thus, our work focuses on the fate of the seed electrons and pertains to the first generation of electron multiplication at the triple point [Jor07b]. We do not consider the space charge effects, nor field enhancement due to dielectric charging, nor do we consider the Fowler-Nordheim coefficients which model material properties in field emission. We simply assume that an electron is released from the metal surface (cathode) with essentially zero initial energy, and ask under what condition this electron would be likely to initiate secondary electron multiplication when it strikes the dielectric surface. This work provides a partial explanation for electron emission from the metal-oxide junction and ablation line focused cathodes presented in this thesis. It also holds relevance to the projection ablation lithography cathode [Boo07, Jon04, Jon05, Jor07], and our interest in rf window breakdown [Edm06, Kim06, Neu01].

While our calculation of the seed electron assumes a DC, electrostatic field for the triple point, it is valid under rf condition also. The justification for this is that we are looking at the immediate vicinity of the triple point, over a spatial scale length much less than the free space wavelength, in which case the rf field may be approximated by the electrostatic field. [The Helmholtz equation (wave equation in frequency domain) reduces to the Laplace equation (electrostatic field equation) when the region of interest is much less than the free space wavelength.] Moreover, the electron's time of flight is usually much less than the rf period. Thus the use of the electrostatic field suffices in the consideration of dynamics of a seed electron that is released from the immediate vicinity of a triple point. The present analysis of the seed electron therefore also applies to a pulsed voltage. In fact, the initiation mechanism plays a more important role in short voltage pulses than long voltage pulses [Mil95, And80, Det73].

In Section 2.2, we present the vacuum field for a general triple point geometry, where the angles subtended by the metal, dielectric, and vacuum, are arbitrary [Chu04]. The triple point geometries analyzed by Bergeron [Ber77] and by Schachter [Sch98] are recovered as special cases. In Section 2.3, we

analyze the electron trajectory for the Bergeron geometry [Figure 2.2b], and determine the condition under which a seed electron likely produces secondary electrons on impact with the dielectric. The scaled parameters are determined. In Section 2.4, we give a numerical example which illustrates why negative angles of θ (defined in Figure 2.2 below) are more likely to produce secondary electron emission than positive θ by a seed electron, a trend consistent with the well-known practices in high voltage insulation. Concluding remarks are given in Section 2.6.

2.2 Electric Field in the Immediate Vicinity of a Triple Point

The immediate neighborhood of a triple point may be considered as two-dimensional, with the metal-vacuum interface on the positive x-axis [Figure 2.1]. The dielectric-vacuum interface lies at an angle θ from the positive y-axis, measured from the counterclockwise direction, and the metal-dielectric interface lies at an angle α from the positive x-axis, measured from the clockwise direction. Thus, the angle subtended by the vacuum is $p_v = \theta + \pi/2$, the angle subtended by the metal is $p_m = \alpha$, and the angle subtended by the dielectric is $p_d = 2\pi - p_v - p_m = 3\pi/2 - \theta - \alpha$. These angles of θ and α are consistent with those used by Bergeron [Ber77] and Schachter [Sch98], respectively. The geometry considered by Bergeron corresponds to $\alpha = \pi$ (i.e., a metal half-space, see Figure 2.2), and the geometry considered by Schachter corresponds to $\theta + \alpha = \pi/2$, (i.e., a dielectric half-space), with data presented mainly for $\alpha = \pi/6$.

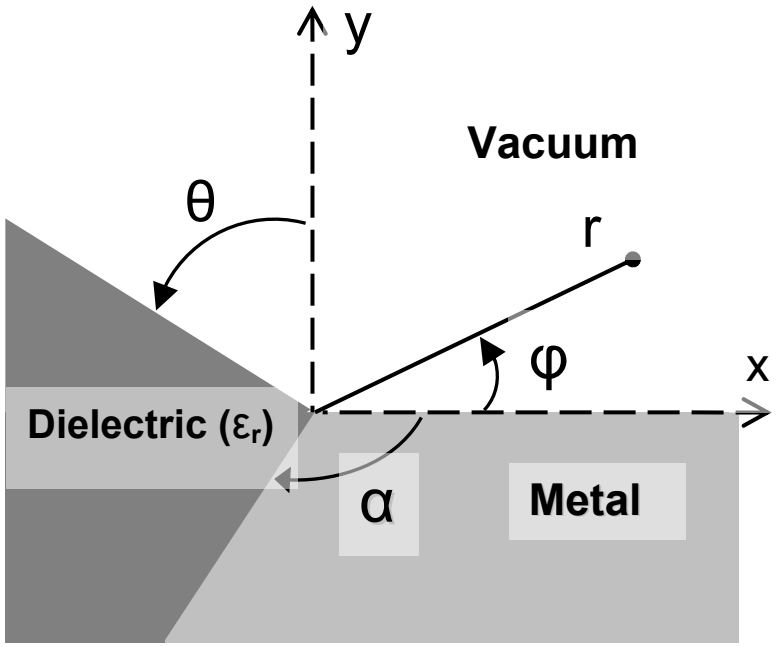

Figure 2.1 A general two-dimensional triple point. The directions of positive angles are shown.

We assume that the potential, Φ, is zero on the metal in Figure 2.1, and is positive at large y. The electrostatic potential in the vacuum region may be constructed from the fundamental solution in cylindrical coordinates (r, ϕ),

$$\Phi(r,\varphi) = r^{\nu}\sin(\nu\varphi); \qquad 0 < \varphi < \pi/2 + \theta \tag{2.1}$$

where ν is the index to be determined. Equation (2.1) is the imaginary part of the analytic function z^{ν} in the cut z-plane ($z = x + iy = re^{i\phi}$), and therefore is a solution to the Laplace equation there. In the dielectric region [Figure 2.1], this fundamental solution reads,

$$\Phi(r,\varphi) = r^{\nu}\frac{\sin\left\{\nu\left[\varphi-(2\pi-\alpha)\right]\right\}}{\sin\left\{\nu\left[(\pi/2+\theta)-(2\pi-\alpha)\right]\right\}}\sin\left[\nu(\pi/2+\theta)\right]; \qquad \frac{\pi}{2}+\theta < \varphi < 2\pi-\alpha \tag{2.2}$$

which ensures continuity of Φ on the boundaries of the dielectric. Continuity of $\varepsilon\partial\Phi/\partial\phi$ at the dielectric-vacuum interface then leads to the determinantal equation for the index ν in the potential distribution,

$$\varepsilon_r \cot\left[\nu\left(\frac{3\pi}{2}-\alpha-\theta\right)\right]\tan\left[\nu\left(\frac{\pi}{2}+\theta\right)\right] = -1 \tag{2.3}$$

where ε_r is the relative dielectric constant of the dielectric. Once the index ν is obtained from a specification of ε_r, α and θ, the radial dependence of the electric field is r^{δ} for both the radial and azimuthal components [cf. Eq. (2.8) below], where the electric field index δ is,

$$\delta = \nu - 1 \tag{2.4}$$

The electric field at the triple point diverges if δ is less than zero, and converges (to zero) if δ is larger than zero. The electric field in the entire vacuum region is a constant if δ = 0, or ν = 1, in which case this constant electric field is parallel to the y-axis [cf., Eq. (2.1)]. This occurs when tan p_d = ε_r cot θ, where p_d = 3π/2 – θ – α is the angle subtended by the dielectric [Figure 2.1]. This is easily derived from Eq. (2.3) after setting ν = 1.

Several limiting cases may be established. As ε_r approaches infinity, the argument of the cotangent factor in Eq. (2.3) approaches π/2, yielding,

$$\nu = \frac{1}{3 - 2(\alpha + \theta)/\pi}; \qquad \varepsilon_r \to \infty \tag{2.5}$$

which reduces to ½ for the geometry considered by Schachter, α + θ = π/2. In the limit of ε_r = 1, it is easy to show from Eq. (2.3) that

$$\nu = \frac{1}{2 - \alpha/\pi}; \qquad \varepsilon_r \to 1 \tag{2.6}$$

Eq. (2.6) is independent of θ, as expected from Figure 2.1 in the ε_r = 1 limit. It is also the same as that given by [Sch98].

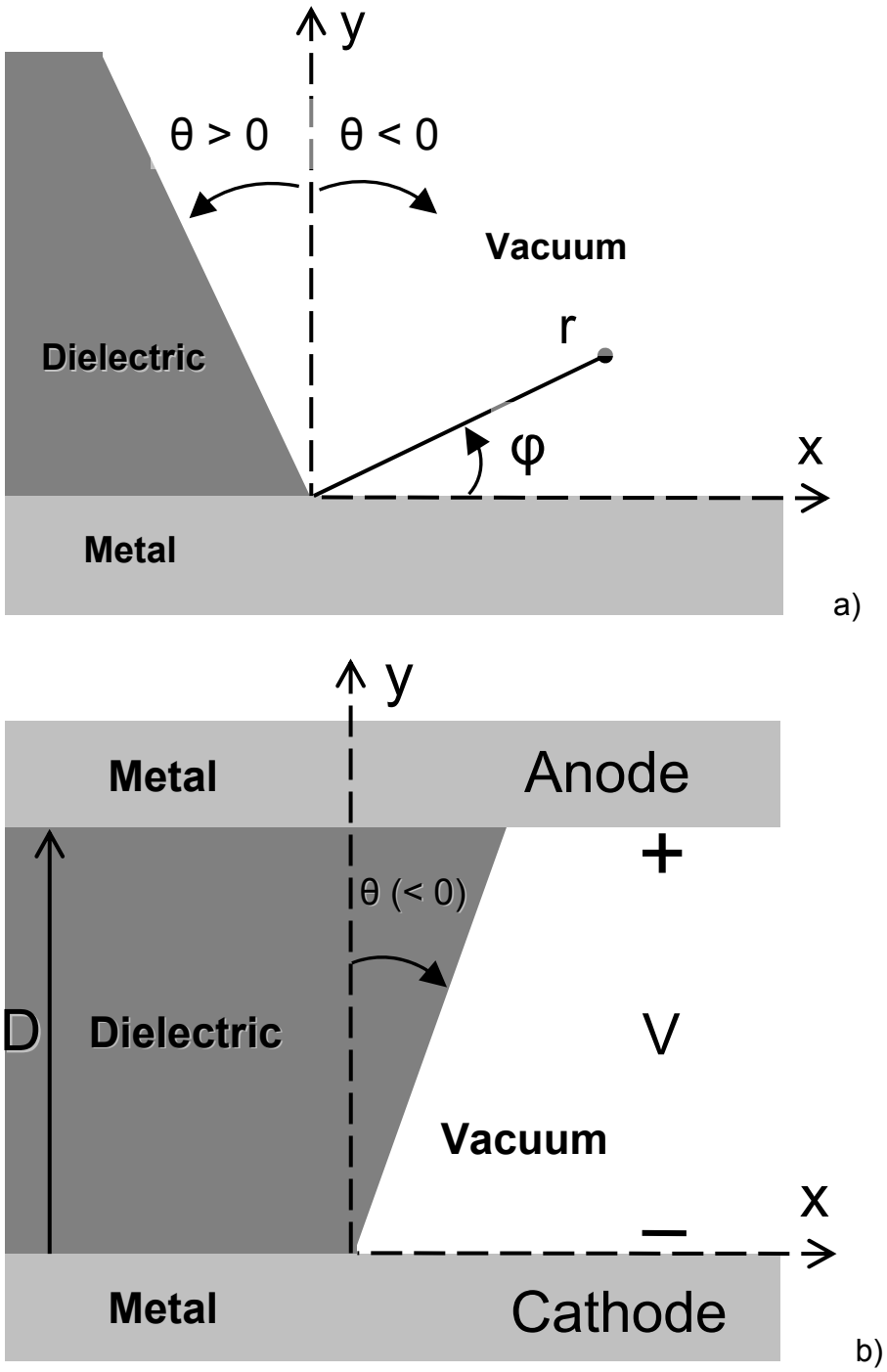

Figure 2.2 (a) A two-dimensional triple point with a half-space metallic surface. (b) An anode-cathode gap with voltage V and separation D. The angle θ illustrated in (b) is negative.

In the geometry studied by [Ber77], on which we shall concentrate henceforth, we take $\alpha = \pi$ (Figure 2.2). The electric field index δ, obtained from solving Eq. (2.3) and using Eq. (2.4), is shown in Figure 2.3 as a function of θ at

various values of ε_r. It is seen that δ and θ have the same sign. Thus, the electric field at the mathematically sharp corner is infinite (zero) when θ < 0 (θ > 0). For θ = 0 and $\pi/2$, a constant, uniform electric field exists in the vacuum region (i.e., δ = 0, or ν = 1), as is expected of the geometry for these angles [Figure 2.2b]. Shown in Figure 2.3b are the magnified graphs for small values of θ. Also shown in Figure 2.3a,b by the dashed lines is the asymptotic approximation of δ for small θ,

$$\nu = 1 + \delta, \qquad \delta \cong \frac{2\theta}{\pi}\left(\frac{\varepsilon_r - 1}{\varepsilon_r + 1}\right); \qquad \alpha = \pi, \qquad |\theta| << 1 \tag{2.7}$$

which is readily derived from Eq. (2.3). The smallness in the magnitude of δ at small values of θ (θ < 0) suggests that the divergent electric field at the mathematically sharp corner of a triple point leads to a relatively mild field enhancement factor in the immediate vicinity of the triple point. The asymptotic expression (2.7) will also be useful to estimate the range of the angle θ most likely for secondary electron multiplication [see Eq. (2.15) below].

As just stated, the electric field at the triple point diverges (converges) for negative (positive) values of θ. More significantly, for negative values of θ, the electric field orientation encourages an electron released from the metallic surface to strike the dielectric [Figure 2.4a], whereas the electric field for positive values of θ tends to repel such an electron from the dielectric surface [Figure 2.4b]. Despite the crudeness of such a model, this observation appears to be consistent with the experimental trends that negative θ has a stronger tendency toward electron multiplication and flashover at the triple point than positive θ [Mil95, Ber77, Gil86, Det73].

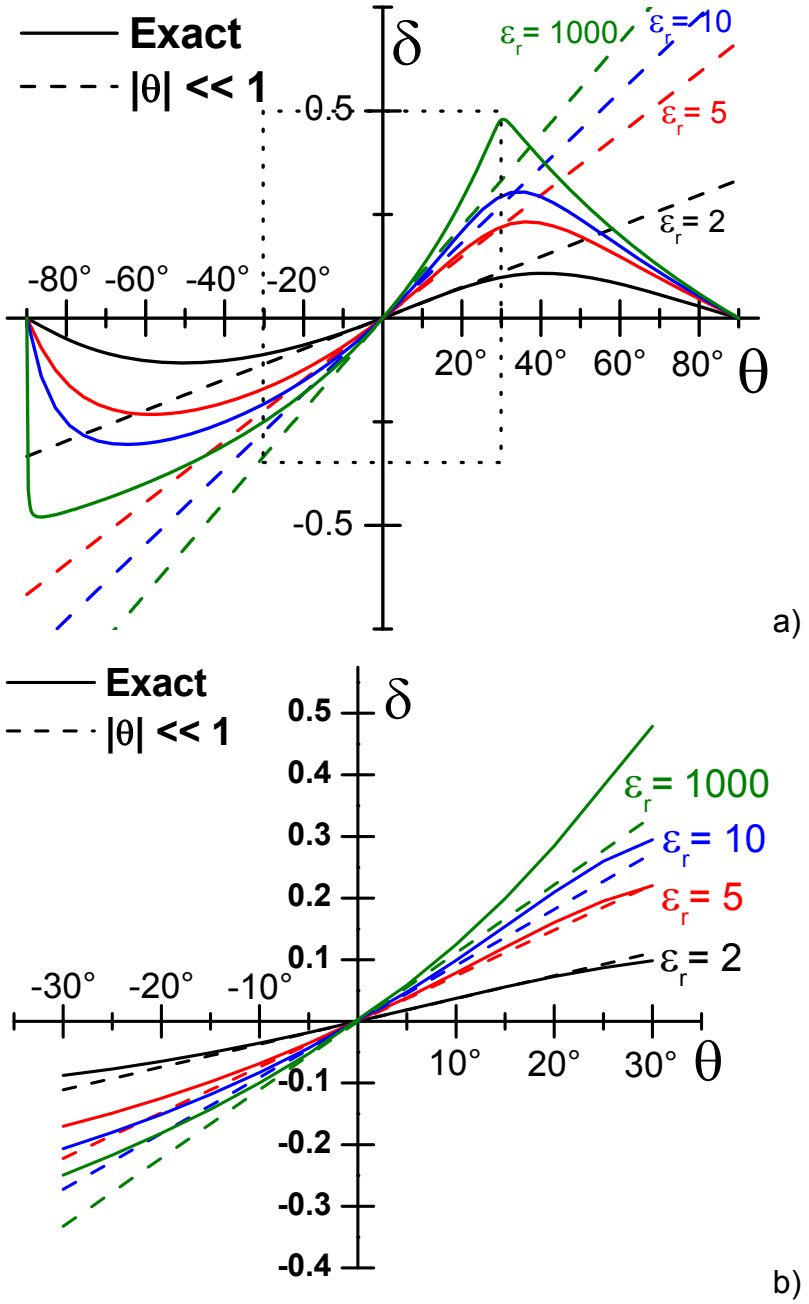

Figure 2.3 (a) The electric field index, δ, as a function of θ for various values of ε_r. (b) magnification of the boxed area in (a). The dashed curves show the analytic approximations for small θ, Eq. (2.7).

To explore the orbits of the seed electrons for positive and negative values of θ, we consider Bergeron's idealized geometry [Figure 2.2b]. The cathode is located at y = 0, the anode is located at y = D and is held at a voltage V with respect to the cathode. The dielectric with θ < 0 is illustrated in Figure 2.2b. In

the immediate vicinity of the triple point, i.e., r << D, the electric field E = -grad (Φ) is expected to be of the form [cf. Eqs. (2.1), (2.4)],

$$\mathbf{E} = -E_0 \left(\frac{r}{a}\right)^{\delta} \left[\mathbf{r}\sin(\nu\varphi) + \boldsymbol{\varphi}\cos(\nu\varphi)\right] \tag{2.8}$$

where E_0 and a are the scale factors for the electric field and distance, which we shall determine shortly for Figure 2.2b. Expressing the unit vectors **r** and $\boldsymbol{\phi}$ in Cartesian coordinates, **r** = **x**cosϕ + **y**sinϕ and $\boldsymbol{\phi}$ = -**x**sinϕ + **y**cosϕ, and using Eq. (2.4), we may re-write Eq. (2.8) in Cartesian coordinates,

$$\mathbf{E} = -E_0 \left(\frac{r}{a}\right)^{\delta} \left[\mathbf{x}\sin(\delta\varphi) + \mathbf{y}\cos(\delta\varphi)\right] \tag{2.9}$$

which we shall use in the integration of orbit of a seed electron. Note that Eq. (2.9) may be written in the compact form, $E_x + iE_y = -iE_0(z^*/a)^{\delta}$, where $z = x + iy = re^{i\phi}$ is the complex variable (not to be confused with the z-axis) and the asterisk denotes the complex conjugate. Equation (2.9) shows that the x-component of the electric field changes sign with δ, and therefore with θ from Figure 2.3. This explains the crucial difference in the orientations of the electric fields in Figure 2.4 between positive and negative θ.

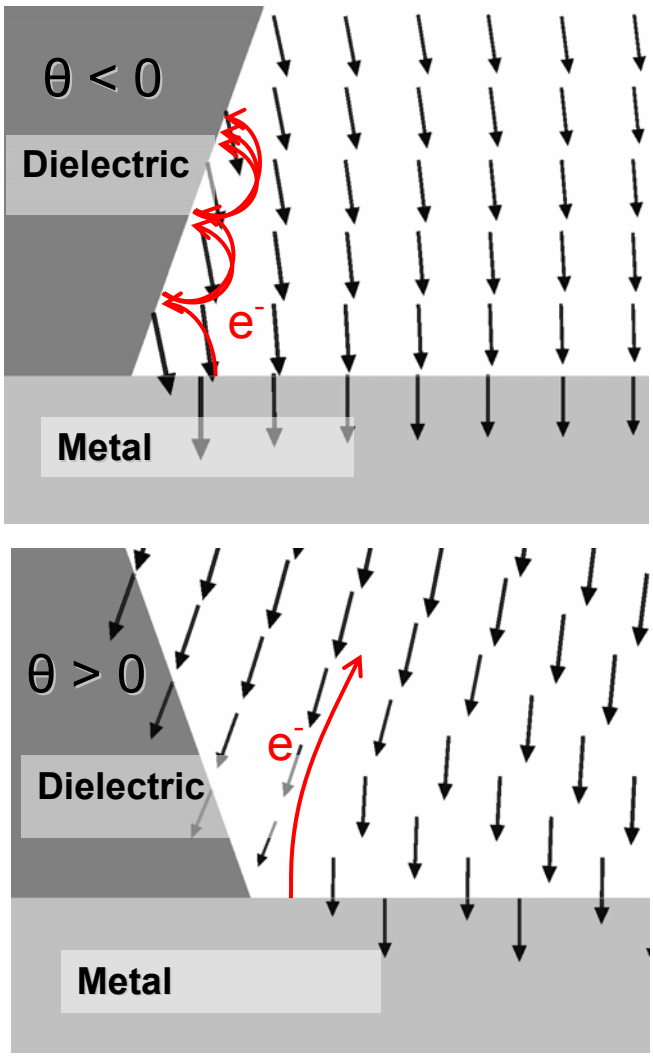

Figure 2.4 Electric fields for θ < 0 (a), and for θ > 0 (b), obtained from a numerical code. Note that the electric field attracts a seed electron to the dielectric in (a), but repels a seed electron from the dielectric in (b).

On the cathode surface, ϕ = 0, r = x [Figure 2.2a], and the cathode electric field becomes $E = -yE_0(x/a)^{\delta}$. The field enhancement factor is $(x/a)^{\delta}$. To find E_0 and a, we simply compare this approximate cathode surface electric field with that obtained numerically from an electrostatic solver for the geometry shown in Figure 2.2b. Sample electric fields in the vicinity of the triple point, obtained by D. M. French [Jor07b] are shown in Figure 2.4 for θ < 0 and θ > 0. The numerical calculations of the electric field were done with the electrostatic solver in commercially available Ansoft Maxwell 2D software [Ans07]. In Figure 2.4, the geometry used was the parallel plate system (Figure 2.2b) of horizontal length 10

cm, anode-cathode gap D = 1 cm, and a potential difference V = 1 volt. To give a sense of scale, the vertical extent of the dielectric shown in Figure 2.4 is 2 mm. Using this code, the electric field far away from the triple point in the vacuum portion of the gap was found equal to V/D, as expected. To model the case of infinite relative permittivity that will be presented in Figure 2.5, the relative permittivity (ε_r) of the dielectric was set at 10,000. This approximation is valid since the change in the electric field values calculated over ε_r ranging from 1000 to 100,000 was less than 0.5%. (The value of δ for ε_r = 1000 was shown in Figure 2.3).

The vertical electric field on the cathode surface, E_y, is shown in Figure 2.5, whose data were extracted from the electrostatic code and normalized for general values of D and V for the geometry shown in Figure 2.2b. Figure 2.5a,b show data for negative values of θ (θ = -5.71° and -19.79°) and Figure 2.5c,d show data for positive values of θ (θ = 5.71° and 19.79°). Also shown in Figure 2.5 is the approximate surface electric field modeled by Eq. (2.9) using the constants,

$$E_0 = V / D, \qquad a = D \tag{2.10}$$

We see from Figure 2.5a,b that, for θ < 0, the approximation (2.10) is valid for a distance even up to x = D from the triple point along the metal cathode surface, over a large range of ε_r and θ. For θ > 0, this approximation is acceptable for

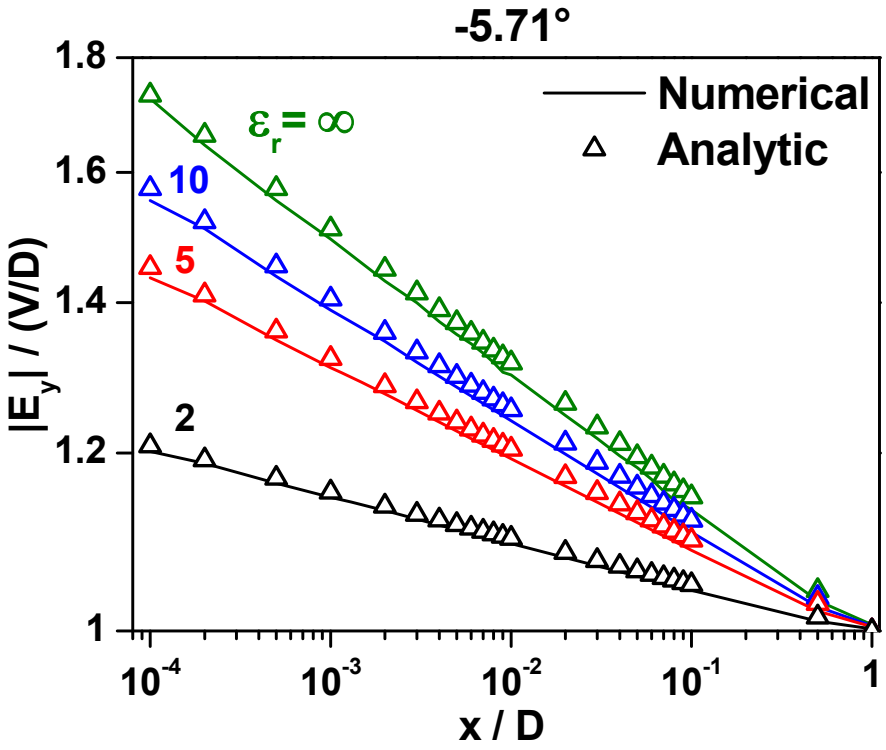

a)

Figure 2.5 Comparison of the cathode surface electric field, obtained from a numerical code, with the analytic approximation, Eqs. (9) and (10), for the geometry of Figure 2.2b: (a) θ = -5.71°, (b) θ = -19.79°, (c) θ = 5.71°, and (d) θ = 19.79°. <Continued on the follow pages>.

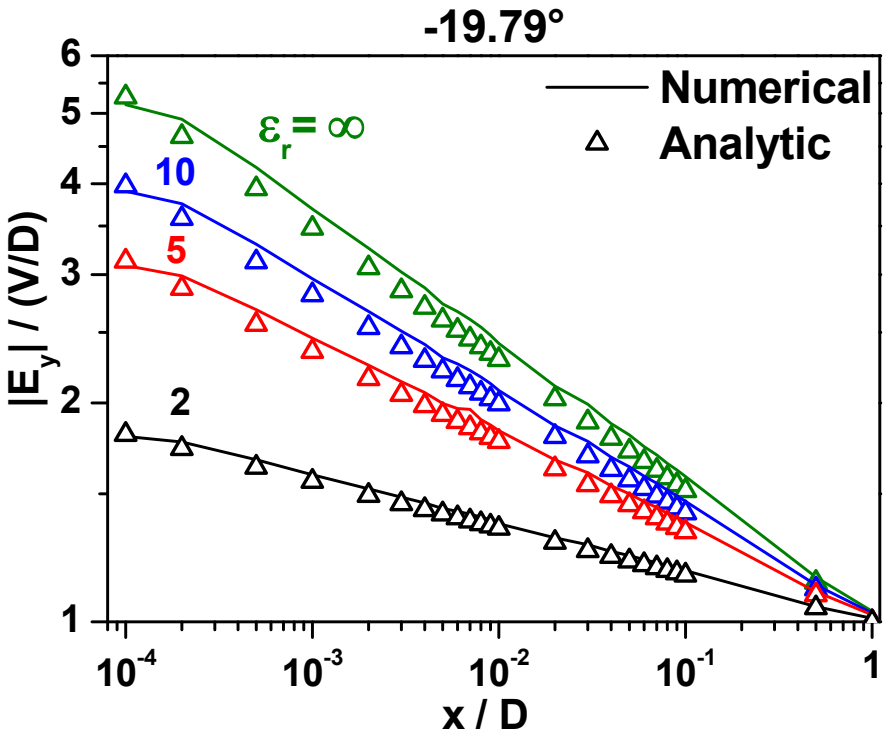

b)

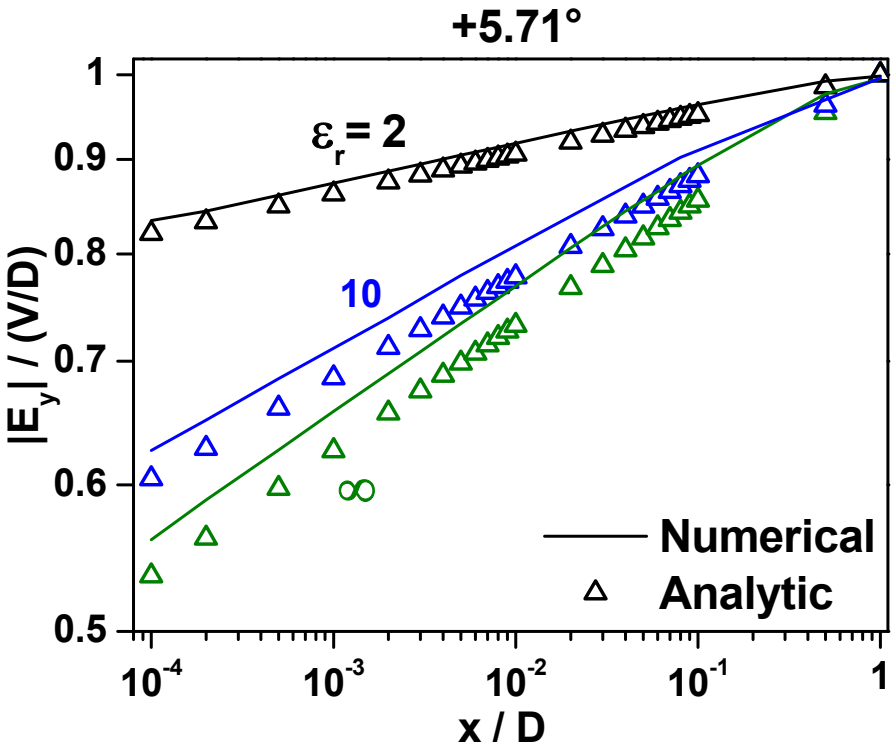

c)

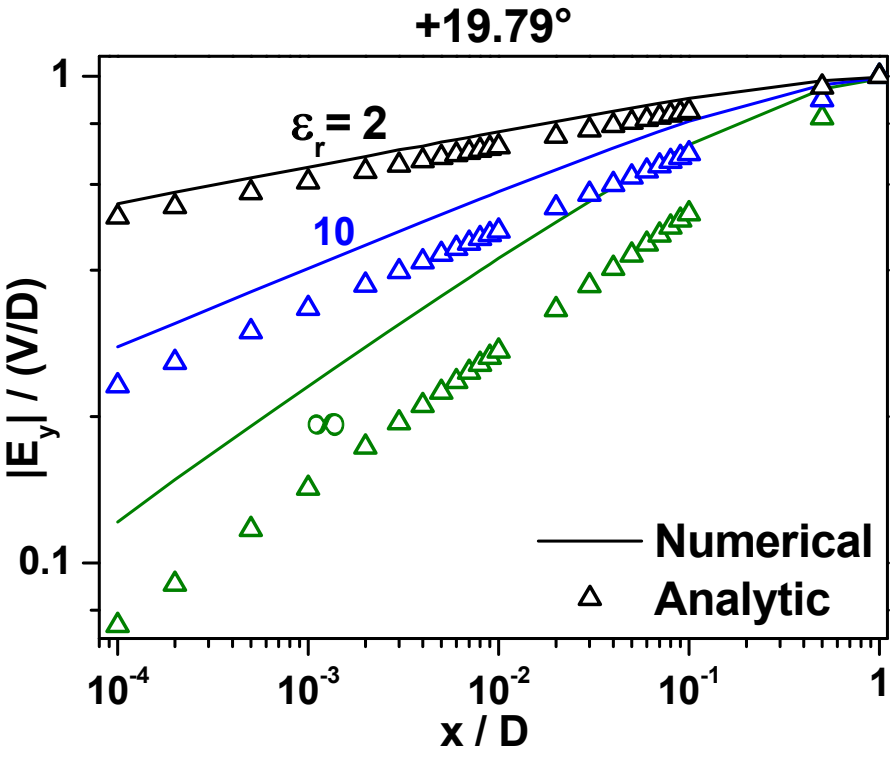

d)

small values of θ, (θ = 5.71°, Figure 2.5c) at all values of ε_r but is only fair for larger, positive value of θ, (θ = 19.79°, Figure 2.5d). Equation (2.10) becomes a poorer approximation for large, positive values of θ probably because of the

more pronounced effects of the vacuum region in Figure 2.2b. The discrepancies may arise from the assumed constant [Eq. (2.10)] or from the assumed form of the solution [Eq. (2.9)], or a combination of the two. Thus, particle trajectories computed from the approximate analytic electric field, to be reported below, will be less accurate for large, positive values of θ. Fortunately cases with large positive θ are of lesser interest to the present study. Note that the field enhancement factors displayed in Figure 2.5 are relatively mild even at a location very close to the triple point (x/D = 0.0001), the maximum field enhancement factor being only 5.2, occurring for θ = -19.79°, and ε_r = ∞ [Figure 2.5b]. For the orbital study of a seed electron given in Sections 2.3 and 2.4, we shall simply use the approximate electric field given by Eqs. (2.9) and (2.10) for the geometry shown in Figure 2.2b.

2.3 Trajectory of a Seed Electron

Since the electric field in the θ < 0 case attracts an electron to the dielectric surface [Figure 2.4a], an electron released from the cathode near the triple point always strikes the dielectric even if this seed electron has a zero initial velocity. The θ > 0 case is entirely different. The electric field tends to repel electrons from the dielectric surface [Figure 2.4b]. An electron released from the cathode must possess some initial velocity in the negative x-direction for it to impact onto the dielectric surface. Thus, we consider these two cases, θ < 0 and θ > 0, separately in this section.

2.3.1 θ < 0

For the case θ < 0, a seed electron released from the cathode surface at (x, y) = (x_0, 0) with zero initial velocity will always strike the dielectric surface. In particular, we are interested in the impact energy of this seed electron to assess its likelihood in releasing a secondary electron, thereby initiating an avalanche process on the dielectric surface. The electron trajectory is most conveniently represented in complex form,

$$\frac{d^2 z}{dt^2} \equiv \frac{d^2 (x+iy)}{dt^2} = -\frac{e}{m}\left(E_x + iE_y\right) = i\frac{eV}{mD}\left(\frac{z^*}{D}\right)^{\delta} \tag{2.11}$$

where we have used Eq. (2.9) and the sentence that follows, as well as the approximation, Eq. (2.10). The initial condition, at time t = 0, for this seed electron is $z = x_0$, $dz/dt = 0$.

This seed electron's normalized trajectory, $\zeta = \zeta(\tau)$, is governed by the following non-dimensional equation and initial conditions,

$$\ddot{\zeta} = i(\zeta^*)^{\delta}, \qquad \zeta(0) = 1, \quad \dot{\zeta}(0) = 0 \tag{2.12}$$

where $\zeta = z/x_0$ and a dot denotes a derivative with respect to the normalized time $\tau = t/t_0$ with the time scale t_0 given by,

$$t_0 = \sqrt{\frac{mD^2}{eV}\left(\frac{x_0}{D}\right)^{1-\delta}} \tag{2.13}$$

Note that the normalized Eq. (2.12) has only one dimensionless parameter, the electric field index δ, which depends only on ε_r and θ [Figure 2.3]. Thus, a specification of ε_r and θ completely determines the trajectory of any seed electron, regardless of the voltage, gap spacing, and this seed electron's birth place as long as it is in the immediate vicinity of the triple point [Figure 2.2b]. This seed electron hits the dielectric surface at the normalized time τ_f, at which the normalized coordinates is ζ_{xf} and ζ_{yf} respectively in the x and y direction, the normalized velocity components are u_{xf} and u_{yf}, and the normalized impact energy is $W_f = u_f^2/2 = (u_{xf}^2 + u_{yf}^2)/2$. The plots of these quantities are shown in Figure 2.6-Figure 2.9 over a wide range of ε_r and θ. For the time being, let us focus on the left portion of Figure 2.6-Figure 2.9, as the initial conditions in Eq. (2.12) apply only to this regime, $\theta < 0$. [The $\theta > 0$ case is treated in the next subsection, 2.3.2].

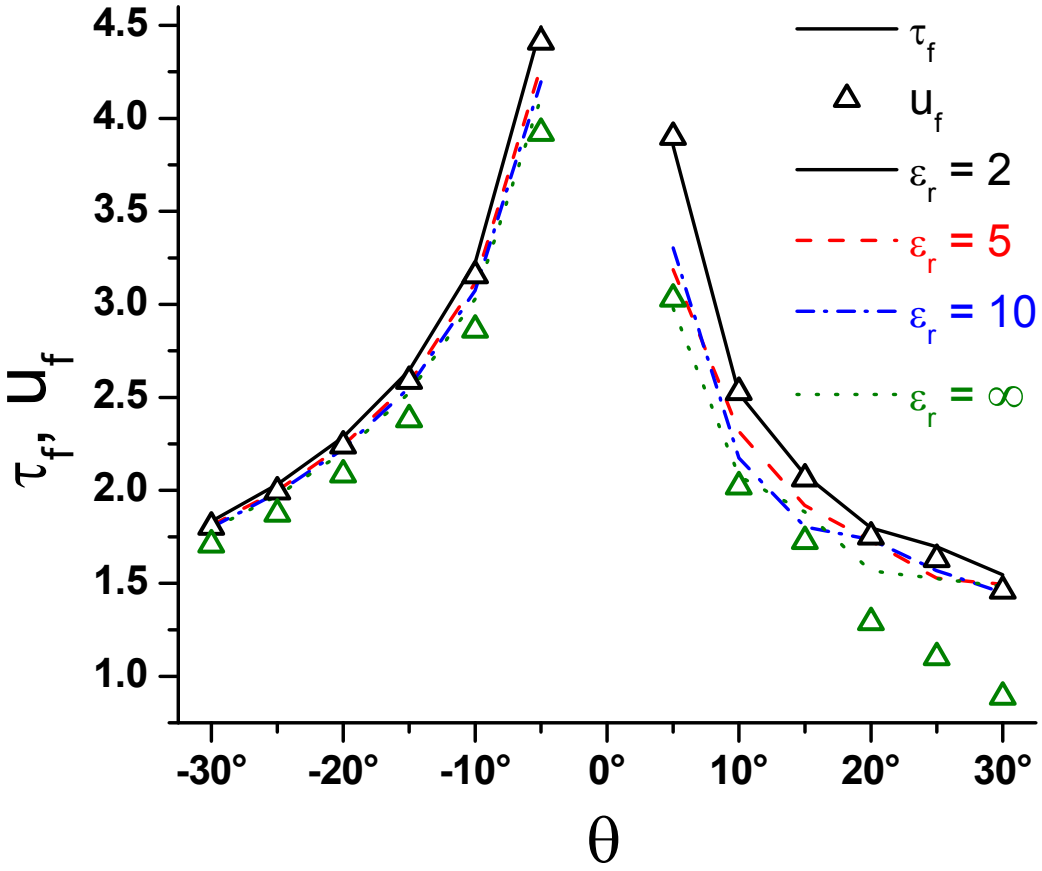

Figure 2.6 The normalized impact time, τ_f, as a function of θ for various values of ε_r (solid and dashed curves). Also shown is the normalized impact speed, u_f (upper triangles for ε_r = 2, and lower triangles for ε_r = infinity).

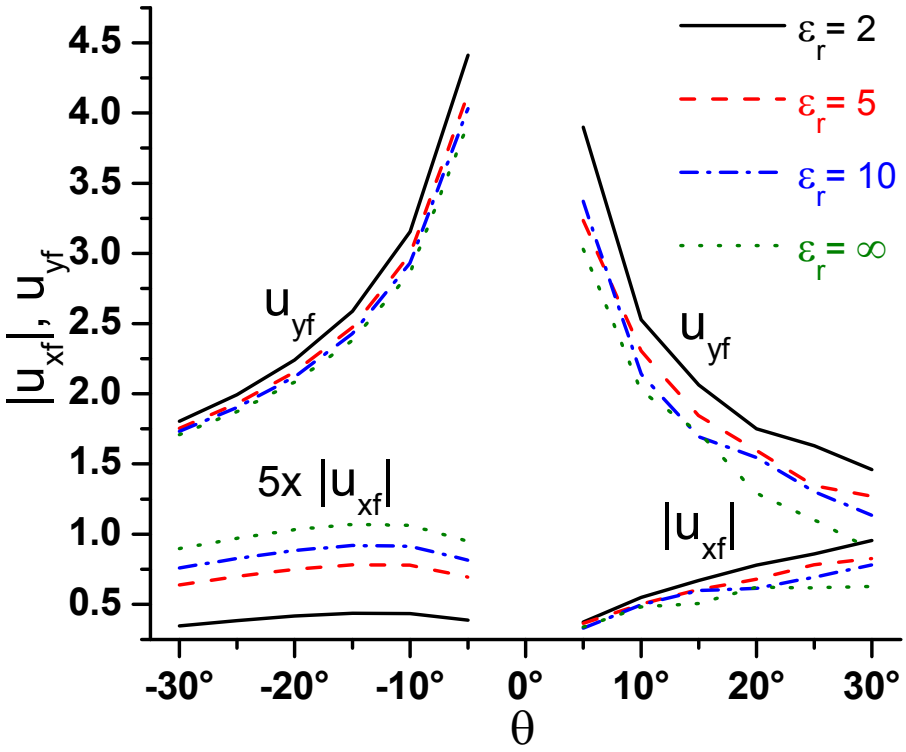

Figure 2.7 The x and y components of the normalized impact velocity as a function of θ for various values of ε_r. The magnitudes of the x-component are shown, for easier comparison with the y-component.

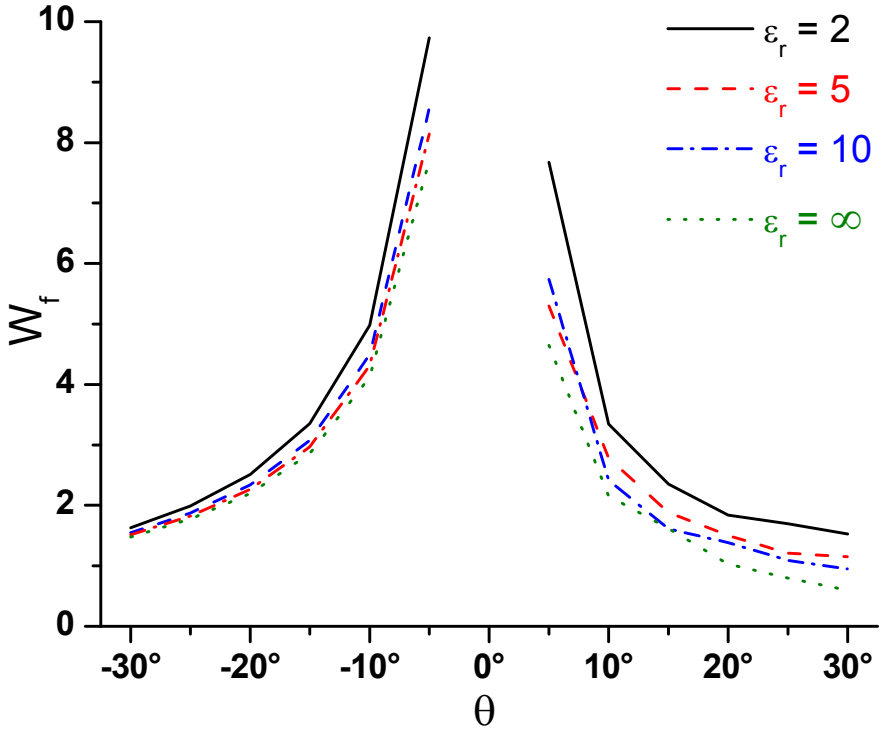

Figure 2.8 The normalized impact energy as a function of θ for various values of ε_r.

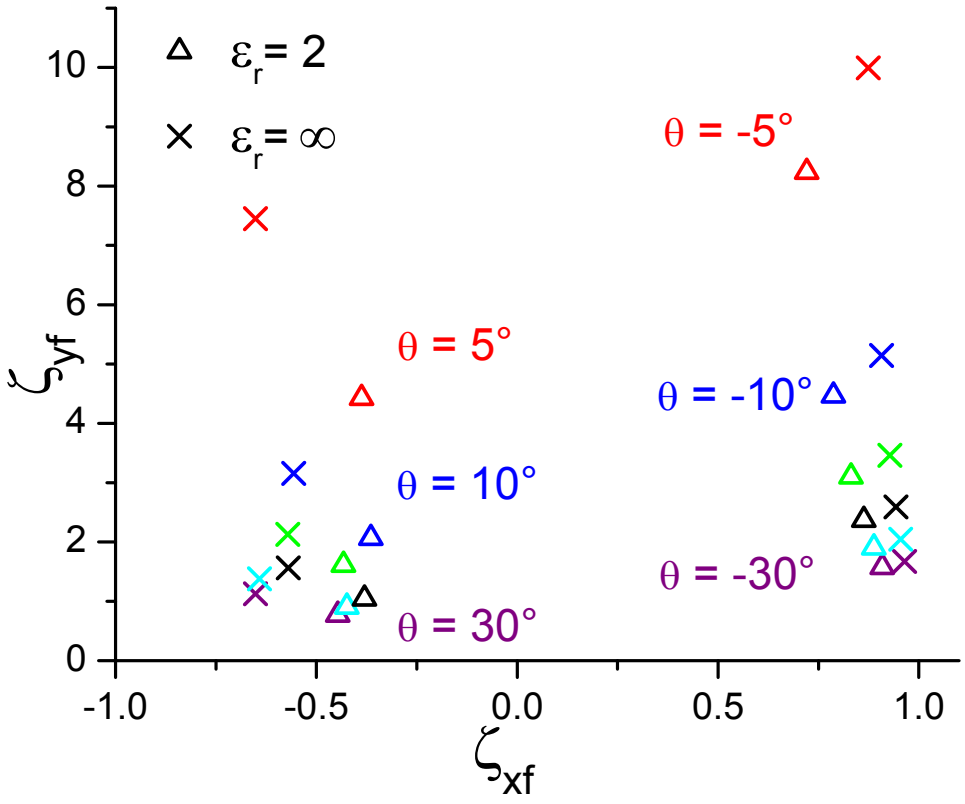

Figure 2.9 The normalized impact coordinates at various θ for ε_r = 2 and ε_r = infinity. From top to bottom, θ = 5°, 10°, … 30° on the left, and θ = -5°, -10°, … -30° on the right.

Figure 2.6 shows that the normalized impact time τ_f and the normalized impact velocity u_f are about equal. This is because the normalized impact velocity u_f is dominated by its y-component u_{yf}, which is much larger than its x-component u_{xf}, as shown in Figure 2.7. When θ is small, the y-directed electric field is dominant and is almost a constant, therefore it gives an almost constant y-acceleration to the seed electron. Thus $u_{yf} \approx u_f$ is approximately proportional to τ_f, the proportionality constant being unity in the normalized coordinates. As θ approaches zero, both τ_f and u_{yf} become large [Figure 2.6 and Figure 2.7] as the dielectric surface is almost parallel to the electron orbit of the seed electron, in which case this seed electron (with zero initial velocity) would travel a long time before it strikes the dielectric. The normalized impact energy, W_f, follows a similar trend [Figure 2.8]. As $\theta \to 0$ ($\theta < 0$), one may very roughly estimate that

$E_{imp} = eV\frac{y_f}{D}$ and $y_f = \frac{x_0}{\tan\theta} \approx \frac{1}{|\theta|}$. From this we may make the approximations $u_f \approx u_{yf} \approx \tau_f \approx \sqrt{\frac{2}{|\theta|}}$ and $W_f \approx \frac{1}{|\theta|}$, as shown qualitatively in Figure 2.6-Figure 2.8.

Note from Figure 2.6-Figure 2.8 that all of these quantities, W_f, τ_f and u_{yf}, are insensitive to the precise values of ε_r. Thus, the use of ε_r = infinity, together with the approximate Eq. (2.7), would provide a useful assessment of a seed electron which now serves as the primary electron for secondary emission on impact with the dielectric surface. Figure 2.9 gives the normalized coordinates of this seed electron when it strikes the dielectric surface. These impact coordinates lie on the dielectric surface.

The dimensional quantities may be expressed in terms of the normalized quantities. They are: impact time $t_f = t_0\tau_f$, impact coordinates $(x_f, y_f) = x_0(\zeta_{xf}, \zeta_{yf})$, and impact velocity $(v_{xf}, v_{yf}) = (u_{xf}, u_{yf})x_0/t_0$. Of most interest is the dimensional impact energy E_{imp}, given by

$$E_{imp} = e(E_0 x_0)\left(\frac{x_0}{D}\right)^{\delta} W_f = eV\left[\left(\frac{x_0}{D}\right)^{1+\delta} W_f\right] \qquad (2.14)$$

Figure 2.3 and Figure 2.8, together with Eq. (2.14), provide a ready assessment of whether secondary emission is likely to occur. A condition for electron multiplication by secondary emission is that E_{imp} lies between E_1 and E_2, the range of impact energy for the secondary yield coefficient to exceed unity [Vau93, Hac59]. (E_1 and E_2 are also known as the first and second cross-over energy, respectively, in the secondary electron yield curve [Figure 2.10]. E_1 is typically of order a few tens of eV, whereas E_2 may exceed several keV, depending on the incident angle of the primary electron and on the roughness of the surface.

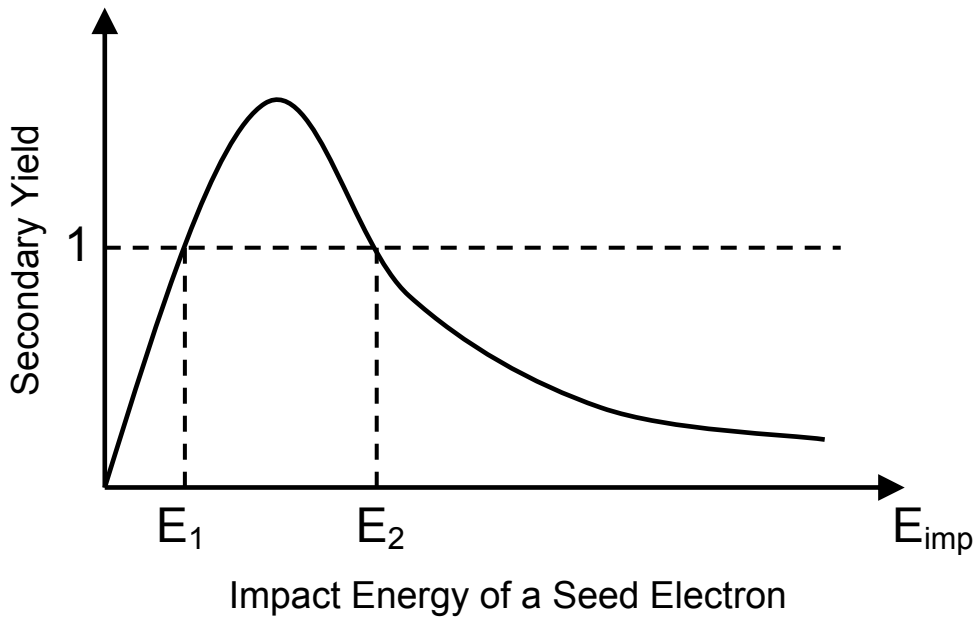

Figure 2.10 Sample secondary electron yield curve.

Numerical examples and additional general representations of E_1 and E_2 may be found, respectively, in Table 1 of [Kis98] and Fig. 3 of [Ang98].)

The electric field at the point of impact on the dielectric surface is also of interest. Its magnitude, and the ratio of the tangential component (E_t) and normal component (E_n), predicts the accessibility of secondary electron multiplication. From Eq. (2.8), the magnitude of the electric field on the dielectric surface at the point of impact is given by $E_0(r_f/D)^{\delta}$ where $r_f = x_0 (\zeta_{xf}^2 + \zeta_{yf}^2)^{1/2}$. Also, setting $\phi = \theta + \pi/2$ in Eq. (2.8), we obtain the ratio of the tangential to normal component (with respect to the dielectric surface), $E_t/E_n = E_r/E_\phi = \tan[\nu(\theta + \pi/2)] = \tan[(1+\delta)(\theta + \pi/2)]$. The numerical example shown in Section 2.4 illustrates that when the magnitude of the electric field falls in the 1MV/m – 10MV/m range, secondary electron multiplication is quite readily accessible over a wide range of dielectric materials and geometries.

We estimate in Section 2.5 below [cf. Eq. (2.18)] the range of angles θ,

$$0 > \theta > -9.1° \times \left(\frac{\varepsilon_r + 1}{\varepsilon_r} \right) \times \sqrt{\frac{E_{0m}/(1eV)}{E_1/(40eV)}} \qquad (2.15)$$

which most likely produces secondary electron avalanche on the dielectric by a seed electron. In Eq. (2.15), E_{0m} (of order a couple eV's) is the perpendicular

energy with which a secondary electron is ejected from the dielectric surface, and E_1 (typical range between 20 – 100 eV) is the first cross-over energy above which the secondary electron yield exceeds unity [Kis98, Ang98, Vau93, Hac59]. The range of angle given in Eq. (2.15) is remarkably consistent with the shaded curve given in Fig. 8.5 on p. 310 of Ref. 1, which shows data of the breakdown electric field with a short voltage risetime of 3 ns. The last expression on the RHS of Eq. (2.15) also roughly corresponds to the minimum electric field for dielectric breakdown shown in Refs. [Mil95, Ber77, Gil86, Det73].

2.3.2 θ > 0

For θ > 0, the seed electron released from the cathode surface has the tendency of being repelled from the dielectric surface [Figure 2.4b]. Thus, this seed electron will strike the dielectric surface only if it has a sufficiently negative x-component in its initial velocity. To reduce the number of parameters, and to obtain some insight into the order of magnitude, we consider only the seed electron that has a sufficiently large negative x-component in its initial velocity so that it just grazes the dielectric surface. For convenience, this seed electron is still assumed to have a zero initial y-component velocity. The trajectory of this electron, released from $x = x_0$ at t = 0, is then again described by the normalized Eq. (2.12), except that the last initial condition is replaced by $\dot{\zeta}(0) = u_{xo}$, where u_{x0} (< 0) is the normalized initial tangential velocity required for this seed electron to just barely touch the dielectric surface. Figure 2.11 shows this initial velocity as a function of θ (θ > 0) for various values of ε_r.

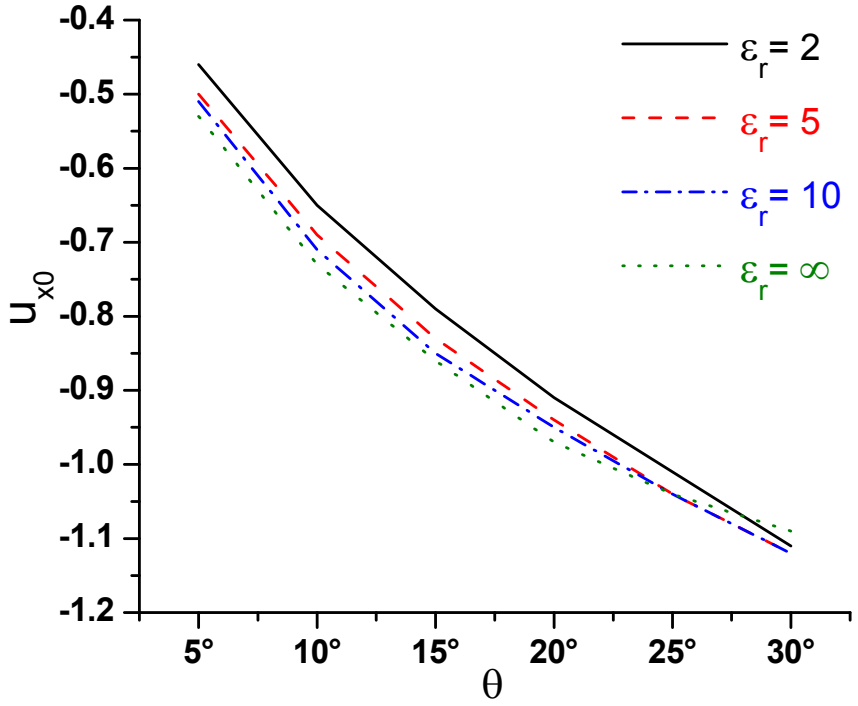

Figure 2.11 The normalized x-component of initial velocity as a function of θ (θ > 0) for the seed electron to just graze the dielectric.

With the initial velocity specified in Figure 2.11, we record the normalized impact time τ_f, the normalized impact coordinates ζ_{xf} and ζ_{yf}, the normalized impact velocity components u_{xf} and u_{yf} , and the normalized impact energy $W_f = u_f^2/2 = (u_{xf}^2 + u_{yf}^2)/2$. The plots of these quantities, for $\theta > 0$, have also been incorporated in the right side of Figure 2.6-Figure 2.9. The right side of Figure 2.6-Figure 2.9, for the case $\theta > 0$, is qualitatively similar to the left side of these figures, for the case $\theta < 0$, with one exception. Note that for $\theta > 15^o$, the initial velocity [Figure 2.11] and the impact velocity [Figure 2.7] have the same order of magnitude, regardless of the value of ε_r. The required x-component of the initial velocity (in magnitude) of the seed electron would have been higher if we include a nonzero y-component initial velocity because in this case, the electron will move further away from the dielectric surface, per unit time. Since few seed electrons could have an initial energy of order 10 eV, this means that it is comparatively less likely to initiate electron multiplication by the seed electrons for θ exceeding 15° or so. This is consistent with the vast experience in the studies of flashover mechanisms, especially for short voltage pulses, where the

role played by the seed electrons is expected to be more dominant than in a long voltage pulse [Mil95, Ber77, And80, Det73]. Using positive dielectric angles, θ, of order 15° at the triple points may then alleviate the flashover problem in high power dielectric rf windows.

2.4 A Numerical Example

In this section, we give a numerical example to show the range of parameters for the analysis outlined in Sections 2.2 and 2.3. Specifically, we set V = 10 kV, D = 1 cm, $E_0 = 10^4$ V/cm, $x_0 = 10\mu$m, and $\varepsilon_r = 2$. We separately consider the θ = -10° and 10° cases.

2.4.1 θ = -10° and ε_r = 2

For θ = -10° and ε_r = 2, we obtain δ = -0.035 [Figure 2.3], $(x_0/D)^{\delta} = 1.27$, $\tau_f = 3.22$ [Figure 2.6], $\zeta_{xf} = 0.91$, $\zeta_{yf} = 5.14$ [Figure 2.9], $u_{xf} = -0.087$, $u_{yf} = 3.16$ [Figure 2.7], $W_f = 4.98$ [Figure 2.8]. For these dimensionless parameters, we obtain the time scale t_0 = 6.68 ps [Eq. (2.13)], velocity scale = $x_0/t_0 = 4.73 \times 10^6$ m/s. At impact on the dielectric surface, the dimensional coordinates is $(x_f, y_f) = x_0(\zeta_{xf}, \zeta_{yf}) = (9.07, 51.4)\mu$m, the impact velocity is $(v_{xf}, v_{yf}) = (x_0/t_0)(u_{xf}, u_{yf}) = (-4.12\times10^5, 4.73\times10^6)$ m/s, and the impact energy is 63.5eV [Eq. (2.14)]. This impact energy exceeds the first cross-over energy (E_1) in the secondary yield curve for most dielectrics. The electric field at the point of impact is 1.2×10^6 V/m [Eq. (2.8)], and the ratio of its tangential to normal component, $E_t/E_n = E_r/E_\phi = \tan[(1+\delta)(\theta + \pi/2)] = 4.4$ in magnitude. This implies a very high probability of avalanche of secondary emission initiated by this seed electron, as explained in the analysis outlined in Section 2.5. This is also in qualitative agreement with the data shown in Fig. 1 of [Ber77] for θ = -10°.

2.4.2 θ = 10° and ε_r = 2

For the second case θ = 10° and ε_r = 2, we obtain δ = 0.038 [Figure 2.3], $(x_0/D)^{\delta} = 0.77$, $\tau_f = 2.52$ [Figure 2.6], $\zeta_{xf} = -0.56$, $\zeta_{yf} = 3.16$ [Figure 2.9], u_{xf} = -

0.11, u_{yf} = 2.52 [Figure 2.7], W_f = 3.3 [Figure 2.8]. For these dimensionless parameters, we obtain the time scale t_0 = 8.6 ps, velocity scale = x_0/t_0 = 1.17 x 10^6 m/s. The electron must possess an initial normalized x-directed velocity, u_{x0} = -0.64 [Figure 2.11], to just graze the dielectric. This corresponds to an initial x-directed energy of 1.57 eV, a reasonable number for the initial energy of secondary electrons, but is perhaps on the high side for a seed electron. At impact on the dielectric surface, this seed electron's dimensional coordinates is $(x_f, y_f) = x_0(\zeta_{xf}, \zeta_{yf})$ = (-5.6, 31.6) μm, the impact velocity is $(v_{xf}, v_{yf}) = (x_0/t_0)(u_{xf}, u_{yf})$ = $(-1.28\text{x}10^5, 2.95\text{x}10^6)$ m/s, and the impact energy is 25.4 eV [Eq. (2.14)]. This impact energy barely reaches the first cross-over energy in the secondary yield curve typically. The electric field at the point of impact is 8.04 x 10^5 V/m [Eq. (2.8)], and the ratio of its tangential to normal component, $E_t/E_n = \tan[(1+\delta)(\theta + \pi/2)]$ = 4.1 in magnitude. But the orientation of the electric field on the dielectric surface in this $\theta > 0$ case discourages further electron multiplication by the seed electron [Figure 2.4b].

The comparison between the θ = -10° and 10° cases show that the seed electron with θ < 0 is far more likely to produce secondary electron emission on the dielectric surface of a triple point. Other ranges of parameters may be similarly considered.

2.5 Preferred Angles for Dielectric Breakdown

We now can estimate the range of angles, θ (θ < 0), in Figure 2.2b which most likely initiates an electron avalanche on the dielectric surface by a seed electron, according to the single particle orbit considerations given in this chapter. Let E_n be the component of the electric field normal to the dielectric surface and E_t be the component of the electric field tangential to the dielectric surface. On the dielectric surface, $E_n = E_\phi$, $E_t = E_r$, and Eqs. (2.4) and (2.8) yield,

$$\frac{E_t}{E_n} = \frac{E_r}{E_\varphi} = \tan[(1+\delta)(\theta+\pi/2)] \cong \frac{\varepsilon_r + 1}{2\varepsilon_r |\theta|}, \qquad |\theta| << 1. \tag{2.16}$$

In writing the last expression of Eq. (2.16), we have assumed $|\theta|$ << 1, used the approximation (2.7) for δ, and expanded the tangent factor for small $|\theta|$.

A seed electron impacting on the dielectric surface may initiate an electron avalanche by secondary emission when the electric field has the orientation shown in Figure 2.4a [Kis98]. Let $E_{0m} = mv_i^2/2$ be the initial energy of a secondary electron associated with its initial velocity component (v_i) that is normal to the dielectric surface. This secondary electron will be accelerated by the tangential electric field, E_t, during its time of flight $T = 2v_i/(eE_n/m)$ before it is attracted back to the dielectric surface by the normal component of the electric field E_n. The tangential velocity gain is $v_t = (eE_t/m)T = 2v_i|E_t/E_n|$, and the impact energy is $E_{imp} = mv_t^2/2 = 4\,E_{0m}\,(E_t/E_n)^2$ where we have ignored the initial energy E_{0m} which is at least an order of magnitude smaller than E_{imp} for cases of interest. For subsequent electron multiplication, E_{imp} should lie between E_1 and E_2 [Figure 2.10], the range of electron impact energy for secondary electron yield to exceed unity [Kis98, Ang98, Neu01]. This condition then reads,

$$E_1 < 4E_{0m}\left(E_t / E_n\right)^2 < E_2 \tag{2.17}$$

Since E_2 is of order several thousand eV's, we may set it equal to infinity in Eq. (2.17). Upon using Eq. (2.16), and remembering θ < 0, Eq. (2.17) then gives the following range of θ that would yield a secondary avalanche by the seed electron,

$$0 > \theta > -9.1° \times \left(\frac{\varepsilon_r + 1}{\varepsilon_r}\right) \times \sqrt{\frac{E_{0m}/(1eV)}{E_1/(40eV)}} \tag{2.18}$$

which is written in practical units in terms of typical values of E_{0m} and E_1. Eq. (2.18) is reproduced as Eq. (2.15) of Section 2.3.1. It gives the range of the angle θ most likely to initiate electron multiplication on the dielectric surface by a seed electron. For example, if we take ε_r = 2.8 (typical for PMMA), E_{om} = 3 eV, and E_1 = 30 eV, the range of Eq. (2.18) is 0 > θ > -25°. This range of angle (dashed red lines) is then in good agreement with the shaded curve shown in

Figure 2.12, which shows data of the breakdown electric field with a short voltage risetime of 3 ns.

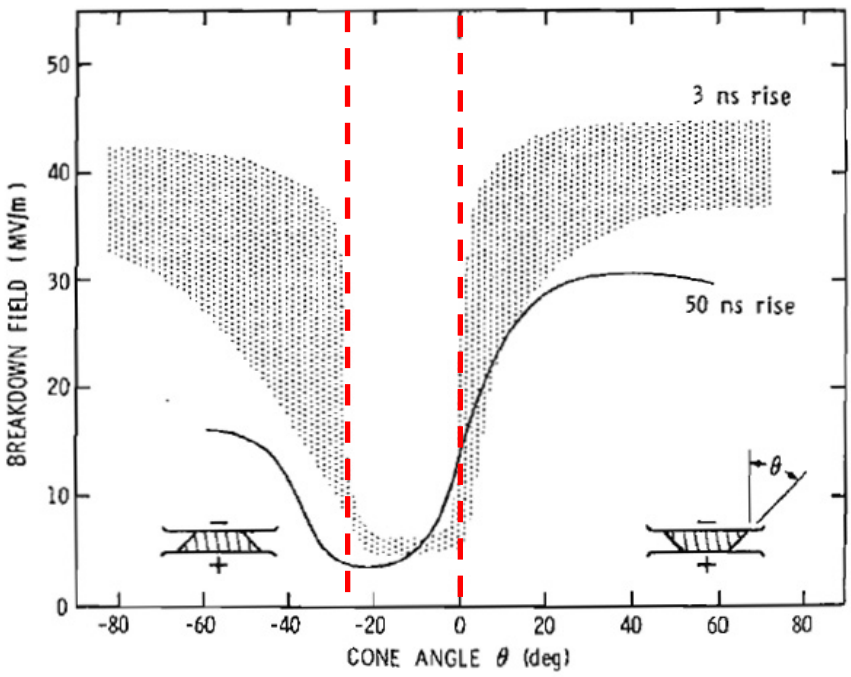

Figure 2.12 Breakdown electric field with voltage risetimes of 3 and 50 ns applied to PMMA insulators [Mil95]. Red lines indicate bounds predicted by Eq. (2.18).

For longer voltage risetimes, the role of initial electrons is less important [Ber77, And80, Det73]. If we assume that a steady state is reached with $E_{imp} = E_1$, one may then argue that the angle given by the last term of the inequality of Eq. (2.18) [which was indeed obtained by setting $E_{imp} = E_1$] may be taken as the angle most likely to observe breakdown. With reasonable numbers inserted into that term, this angle may range between -5° and -30°, in qualitative agreement with the angles for lowest breakdown electric field according to the data presented in Refs. [Mil95, Ber77, Det73, Gil86].

2.6 Concluding Remarks

In this chapter, we analyze the electric field in the immediate vicinity of a triple point, the field enhancement factor there, the electron orbit of a seed electron, and the likelihood of significant electron yield through a secondary electron emission cascade on the dielectric surface. We concentrate on the

generic geometry shown in Figure 2.2b. We estimate the range of the angle θ most likely to produce an avalanche of secondary electron emission [cf. Eq. (2.15)]. This range is found to be consistent with experiments, especially for short voltage pulses. Simple formulas, in analytical and graphical forms, are presented to assess the impact energy of a seed electron, once the gap voltage, gap spacing, dielectric angle, and the birthplace of the seed electron is specified. Numerical examples are given. A formula to assess the range of angles most likely to induce breakdown is presented, and shows good agreement with previously published results for short voltage risetimes.

We find that a seed electron is far less likely to generate secondary emission for positive values of θ because the electric field has a tendency to repel electrons from the dielectric surface, under the assumption that the dielectric surface is not positively charged as in this thesis. Thus, only those seed electrons with a sufficiently large initial velocity toward the dielectric can participate in producing significant secondary yield. The smaller fraction in the velocity distribution of the seed electrons that can participate in secondary electron multiplication may be one reason why a higher voltage can be sustained against dielectric flashover when $\theta > 0$ [And80, Ber77, Det73, Mil95].

While the above results are tantalizing in that they seem to be consistent with the conventional wisdom developed for the triple point, we must stress that they are inferred from the orbit of the first electrons. We have ignored the charging on the dielectric surface which led to field enhancement and to sustained secondary electron cascade for $\theta > 0$. We have not included the initial velocity distribution of the seed electrons, nor have we incorporated the Fowler-Nordheim equation to account for the spatial distribution of these seed electrons released from the immediate vicinity of the triple point. We have also ignored all space charge effects, and we have avoided the extremely difficult analysis of Child-Langmuir law in higher dimensions [Lau01, Lug02], in a metal-vacuum-dielectric assembly. On impact of the dielectric by the seed electron or by subsequent generations of secondary electrons, we have ignored the secondary yield curves, as well as plasma production on the dielectric surface as a result of

desorption and ionization. Thus, we have not considered the spatial and time scale of the full avalanche, nor the effects of background gas pressure and gas composition.

The preliminary analysis given in this chapter seems to suggest that ample secondary electrons may be generated by a seed electron released from the metallic cathode surface of a triple point that is subjected to a sufficiently high voltage. One is led to wonder if an oxide or impurity adsorbed on a metallic cathode surface, forming locally a triple point, effectively amounts to a lower work function than that of the impurity and of the metallic surface. Reduced effective work functions have been reported for dispenser cathodes, in which oxides are impregnated into a metal base in the form of islands [Gil86]. For the case of a single-tip field emitter, the site of an oxide impurity on the surface has also been known to be the location where the major field emission current is drawn [Tur89]. In that case, one might also wonder if the triple point could have played a role in the current emission in the manner studied in this thesis. Thus, while secondary electrons are the main electron sources in certain crossed-field amplifiers [Gil05], they might also have been the main electron source on hot cathodes [Gil86] and cold cathodes [Jon04, Jon05, Jor07] where there are triple points distributed over the cathode surface.

Finally, we briefly comment on the case where there is an external magnetic field (B) which is perpendicular to the x-y plane [Fig. 2.2], as in a crossed-field device. For B = 2.35 kG, the seed electron then has a Larmor radius r_L = ~115 μm for the example given in Section 2.4.1. Thus in this example, the seed electron does not complete a Larmor cycle before it strikes the dielectric. However, for subsequent secondary electrons, we find r_L = 25 μm, with an assumed initial emission energy of a secondary electron at 3 eV. This indicates that a dielectric thickness of 100's of microns (or larger) is capable of secondary electron multiplication in a crossed-field device.

CHAPTER 3
FABRICATION TECHNIQUES FOR CATHODES AND FILMS

As the previous chapter indicates, electrons are emitted at triple point junctions, both through field enhancement and secondary electron emission. While this is a typically a problem in HPM devices, we have sought to use this to our advantage by fabricating cathodes with many triple points along their surface.

To this end, six different MOJ cathodes have been fabricated, and are denoted MOJ-01 through MOJ-06. Two baseline cathodes, metal island only (MIO) and dielectric coated (DiCoat) were also fabricated for comparison with the MOJ series. These cathodes, along with many silicon test samples, were created by focusing a KrF excimer laser onto the surface of a hafnium target in a 100 mTorr O_2/Ar environment. This creates a plasma plume that deposits oxidized Hf through a mask onto the surface of a cathode (or silicon wafer). The cathodes differ in the laser fluence used, as well as the pattern used to mask the cathode surface.

Additionally, five ALF cathodes have been fabricated, denoted ALF-1 through ALF-4, with Tri-ALF as the fifth. The ALF cathodes were fabricated using the same laser, but with the beam focused through a cylindrical lens onto the cathode surface directly. The resulting ablation creates ~1.5 cm long trenches in the cathode surface (Figure 5.1). The ablation is performed in air, so the ablated material re-deposits on the sides of the trenches, creating many sets of peaks and valleys in the cathode surface (Figure 5.2).

3.1 Excimer Laser Configuration

Fabrication of all cathodes and films was performed using a Lambda Physik Compex 205 excimer laser, with a pulse length of 20 ns and wavelength of 248 nm when using KrF as the lasing medium. The laser's internal voltage ranges from 18-26 kV, resulting in output pulse energies of 0-600 mJ.

The output energy of the excimer laser increases non-linearly with the applied voltage, as measured by the laser's internal energy monitor, as well as an external Lumonics 50D-171 energy monitor placed near the beam exit. The laser energy is also seen to decrease with time, and consequently a new gas fill is required to restore full laser energy. Originally the KrF excimer laser was fitted with a solid fluorine source (as well as dedicated Kr, Ne, and He cylinders), which keeps the hazardous fluorine gas in a more stable solid state, and only converts F_2 into the gas phase when a new fill is requested. However, there is considerable cost associated with replacing a solid fluorine source, and solid sources have been largely discontinued by Lambda Physik. The laser was reconfigured to operate with a 280 liter pre-mixed (Spectra Gases) gas cylinder containing 0.085% F_2, 1.68% He, 3.82% Kr, 94.4% Ne, while also requiring a separate neon cylinder as a buffer gas. Due to the hazardous nature of fluorine, the cylinder must use pressure regulators designed for corrosive gases, and must be stored in a gas cabinet with active ventilation systems. For additional protection, a fluorine leak detector and alarm could be installed within the cabinet.

A 2000 liter pre-mix cylinder is projected to last for 10 gas fills, considerably smaller than the 33 fills available from a solid source. However, one distinct advantage of the pre-mix cylinder over a solid source is the longevity of each gas fill. Laser energy as a function of time remains relatively stable for 450,000+ laser pulses, and then rapidly decreases after a certain time has elapsed and/or a certain number of shots have been performed. When gas fills were performed using a solid source, the laser energy would steadily decay, but at an accelerated rate. As such, if it is necessary to operate the laser near its maximum energy output, a pre-mixed cylinder provides a much longer

operational lifetime between gas fills (~500,000 laser pulses compared to ~250,000 for the solid source).

To determine laser fluence at the target, the unobstructed laser beam is measured internally and externally. The beam is then measured after it passes through the laser window and the focusing lens. The laser spot size at the target is measured by ablating a piece of exposed Polaroid film with 1 laser pulse at 100 mJ energy (as measured by the laser's internal energy monitor). Multiplying the reported beam energy by the transmission percentage of the entrance window and lens, and dividing by the measured ablation region, gives the laser fluence (J/cm^2) at the target surface.

$$Fluence = \frac{Beam\ Energy}{Spot\ Size} \times Transmission\,\% \tag{3.1}$$

The transmission characteristics of the entrance window vary considerably with time, ranging from 50 to 90% transmission. Particulate from the ablation process inevitably deposits on the internal surface of the window, reducing its transmittance. To compensate for this time-varying transmittance, the window is periodically measured, cleaned with an optical polishing compound, and then re-measured. The total number of pulses fired by the laser is recorded at this time, and then also recorded again whenever a detailed calculation of the fluence is required. If we know the transmittance of the "clean" window (T_{clean}), the transmittance of the "dirty" window (T_{dirty}), the number of pulses between cleanings (τ_{total}), and the number of pulses since the last cleaning (τ_1), we can interpolate the transmittance using the simple relation given in Eqn. (3.2).

$$Transmittance = T_{clean} - \frac{T_{clean} - T_{dirty}}{\tau_{total}} \times \tau_1 \tag{3.2}$$

Clearly this assumes a linear relationship between laser pulses and window transmittance, and for certain deposition scenarios this may not be accurate, but it gives an estimate that is acceptable for our purposes. The window receives a much thicker coating, per shot, when a flat slab target is used (typically for spectroscopy measurements), compared to a pyramidal target used

for most ablation experiments. If a mixture of these orientations is used between window cleanings, this is likely to introduce the most error into the transmittance estimate.

The generic vacuum chamber setup is shown in Figure 3.1. A turbopump and roughing pump bring the chamber down to vacuum on the mid 10^{-6} Torr scale, as measured by the KJL-G075N Ion Gauge. For oxide deposition, a controlled amount of background gas (20% O_2, 80% Ar) enters into the chamber through a mass flow controller. This is held at a gas pressure of 100 mTorr, as measured by a KJL-6000 thermocouple gauge, connected to the KJL-4500 Ion Gauge controller. Also shown in the figure is a generic substrate, which would either be a hollow cathode tube, a silicon wafer, or a thin metal film. Attached to the substrate, is the high voltage supply occasionally used to supply bias voltage. Unless otherwise specified, no voltage was applied.

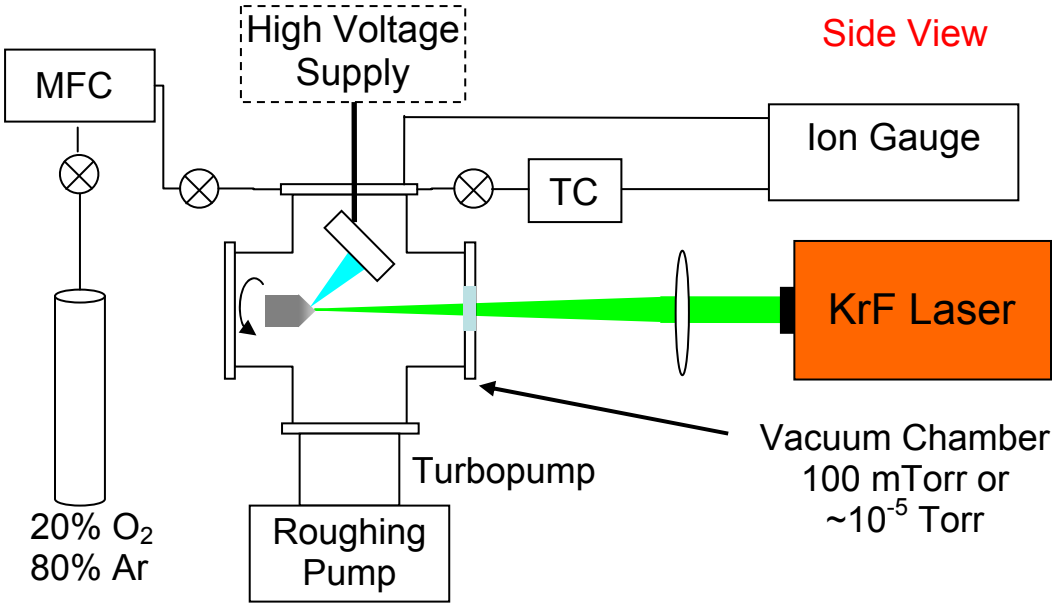

Figure 3.1 Basic experimental configuration for all deposition experiments. Vacuum chamber is held at 100 mTorr (Ar/O_2) or ~10^{-6} Torr, depending on the experiment. HV Supply is not used in most experiments.

3.2 ALF Cathode Fabrication

The Ablation Line Focused (ALF) cathode consists of an aluminum or stainless steel rod with lines ablated around its circumference, Figure 3.2.

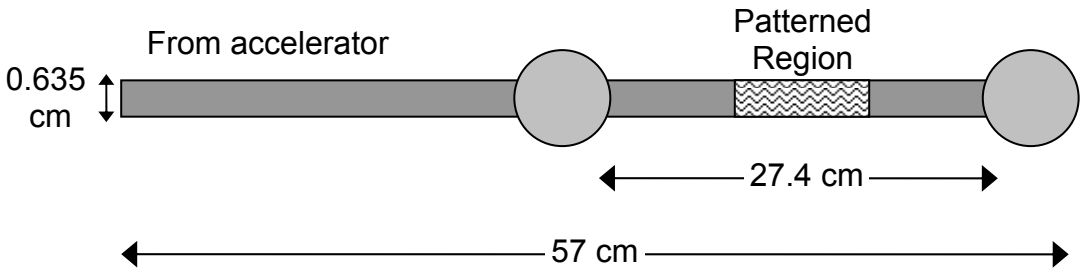

Figure 3.2 Cathode dimensions for all MELBA-C cathodes. Sleeve length for metal oxide junction (MOJ) and ALF cathodes is 27.4 cm as indicated.

Cathodes are fabricated by masking the excimer laser beam to create a 0.8 cm x 1.9 cm rectangle. Masking the beam improves the uniformity by removing low intensity regions of the beam. The beam is then focused through a UV-grade fused silica, cylindrical lens (f=30 cm, 2.5cm x 5.9 cm) onto the surface of the cathode stalk. The resulting beam spot is typically 0.25 mm wide, with some variation depending on the precision of the lens alignment. As shown in Figure 3.3, the cathode is held by a National Aperture MicroMini rotary stage, which is computer controlled via LabVIEW [Appendix C]. This control program allows the user to rotate the cathode, fire the laser, or set up a fixed number of laser shots and rotations. This greatly reduces the time and tedium associated with producing a cathode.

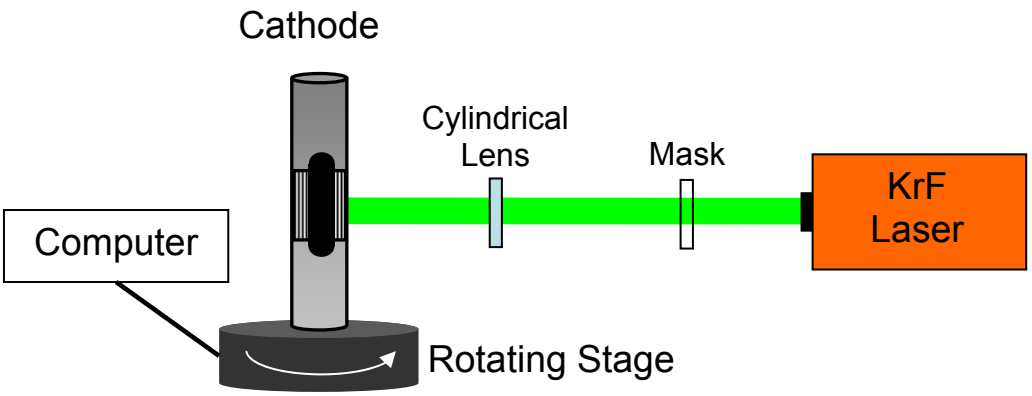

Figure 3.3 Fabrication of Tri-ALF cathode using computer controlled rotary stage.

All ALF cathodes were fabricated in open air. If it became necessary to fabricate them in vacuum conditions, perhaps to reduce oxidation or redeposition, an appropriate rotational feedthrough would be necessary, as the computer controlled stage is not rated for vacuum operation.

3.2.1 Tri-ALF Cathode Fabrication

The Tri-ALF cathode is an extension of the basic ALF design. This form of cathode priming, similar to the Tri-PAL design [Jon05], utilizes 3 distinct emission regions to stimulate electron bunching. In addition, the non-ablated regions are milled out in sections 0.8 cm wide, 6.1 cm long, and 0.3 cm deep, and then covered with carbon paint, Figure 3.4. Both the carbon paint and radius reduction are intended to suppress electron emission in those regions, further enhancing the priming effect. The non-patterned regions of the cathode are a 1.27 cm diameter Al 6061 rod polished with 2500 grit sandpaper.

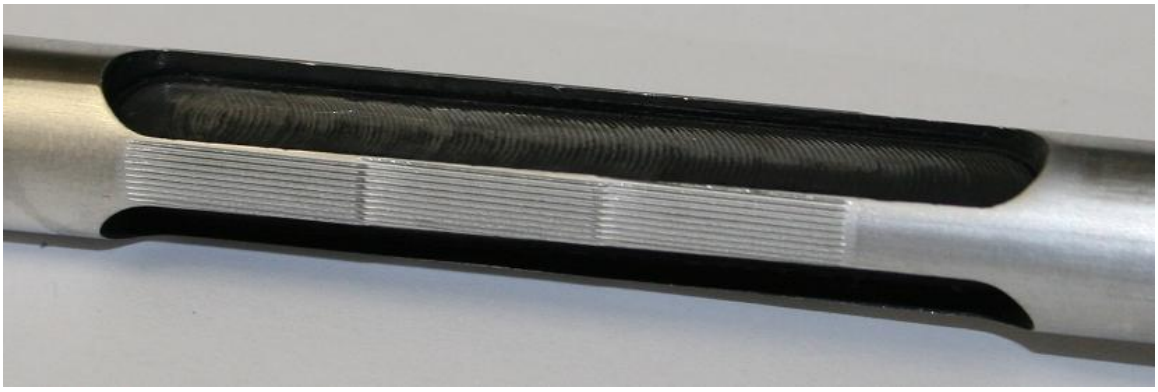

Figure 3.4 Tri-ALF cathode after testing. Only one of three patterned emission regions is visible, each region is 0.5 cm wide and 4.5 cm long.

3.3 Thin Film Deposition

In all thin film deposition experiments the excimer laser was focused by a 30 cm focal length fused silica lens to spot sizes ranging from 0.4 mm^2 to 1.3 mm^2, and entered the vacuum chamber through a fused silica window, as seen in Figure 3.1. Laser pulse repetition rates of 10-15 Hz were employed, and laser energies ranged from 50 to 300 mJ at applied laser voltages of 18-25 kV, resulting in laser fluences between 2 and 40 J/cm^2.

The target used in all hafnium ablation experiments is a 0.25 mm thick hafnium foil, supplied by Alpha Aesar. The purity is 99.5% metals basis, excluding Zr, and contains a nominal Zr concentration of 3%. The purity is quoted as a "metals basis," meaning the metallic content is 99.5% hafnium, but the non-metal (most notably, oxygen) content of the target is unknown. The tip of a pyramidal target is covered with this foil, as seen in Figure 3.5, and the target rotates at approximately 20 RPM. The specific rotational velocity is of little importance, but a rotating target provides a few important benefits. First, it rasters the ablation plume side to side, slightly improving film thickness uniformity. Additionally, it prevents severe localized heating of the target, reducing the rate of material removal and consequently increasing the usable lifetime of the hafnium foil. Typical foil lifetimes at 20 J/cm^2 were on the order of 40,000 pulses.

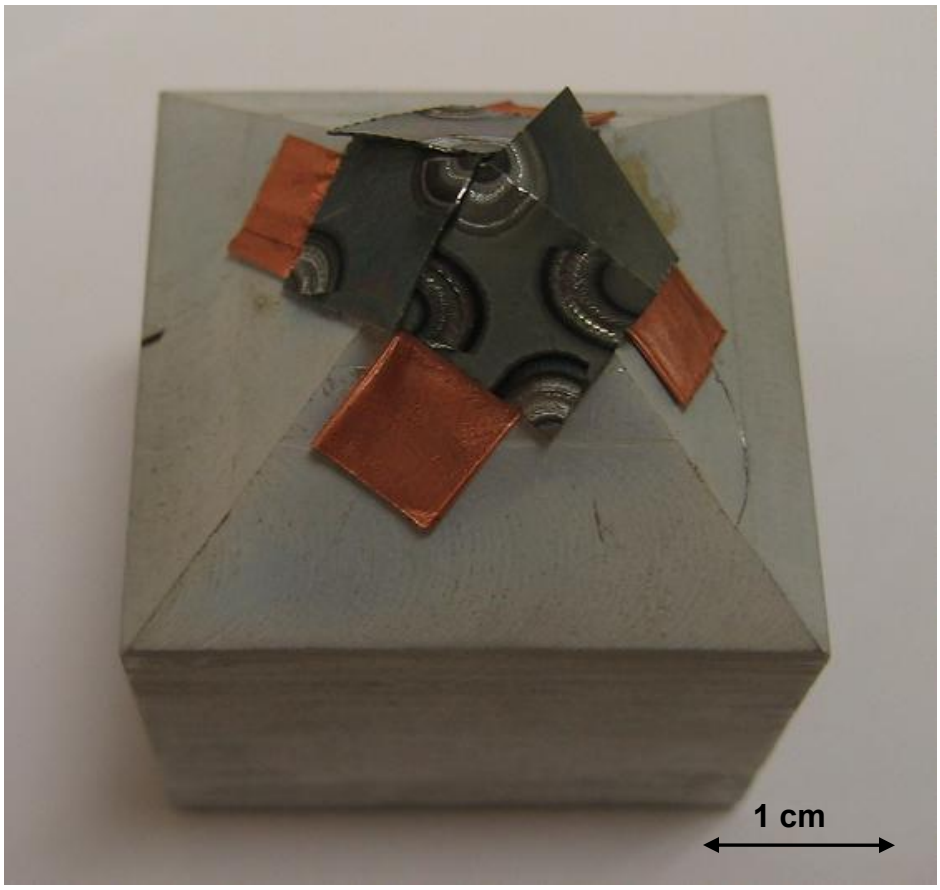

Figure 3.5 Aluminum pyramid target, covered with four pieces of 0.25 mm thick Hf foil.

As the laser pulse strikes the surface of the target, hafnium ions, neutrals, and particulate are ablated. This ablation plume expands and moves away from the target surface, propelled by the initial energy of the ablated material. Except for very extreme laser incidence angles (nearly parallel to the surface), the plume expansion will, primarily, be perpendicular to the target surface (Figure 3.17b) [Chr94].

3.3.1 Thin Films on Silicon

To test properties of the deposited cathode films, it was often impractical to analyze samples on the cathode surface, so test samples were fabricated on silicon wafers, approximately 2.5 cm by 2.5 cm. These wafers were positioned within the chamber, 2-3 cm from the target surface, Figure 3.6.

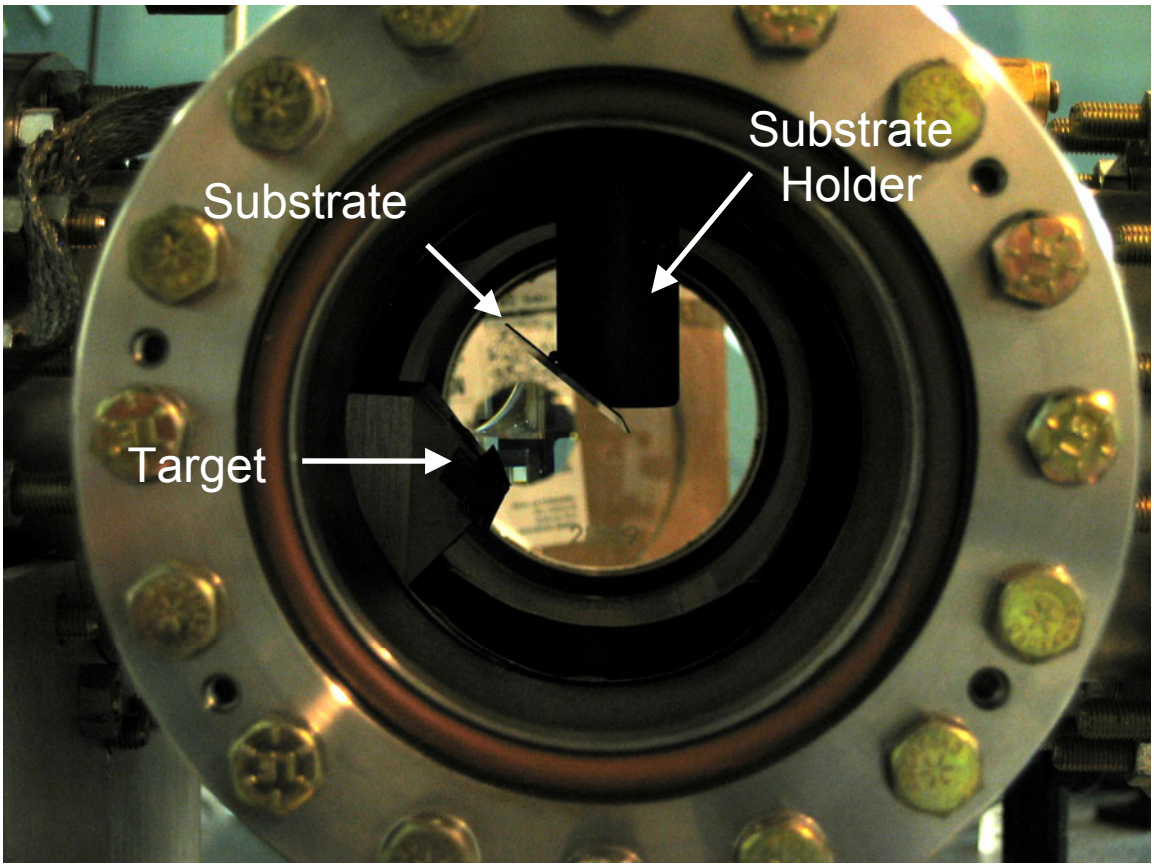

Figure 3.6 Photograph of deposition setup with pyramid target and silicon wafer substrate. Target-substrate gap is 25 mm.

For ion implantation, a negative potential could be applied to the substrate holder. Conversely, a positive potential could be applied to ensure deposition of only neutrals and particulate.

3.3.2 MOJ Cathode Fabrication

Metal oxide junction (MOJ) cathodes consist of a grooved, aluminum support rod surrounded by a stainless steel sleeve, held in place by two spherical electrostatic endcaps. The total cathode length is 57 cm, and the diameter is 1.27 cm. The length of the sleeve portion of the cathode is 27.4 cm, with a sleeve thickness of 0.086 cm, as shown in Figure 3.2. During fabrication, the hollow sleeve is positioned 1.5-3.5 cm from the target surface. The cathode sleeve is suspended from the top of the vacuum chamber (Figure 3.7), and masked by a perforated or woven mesh, as shown in Figure 3.8 and Figure 3.9.

Some oxide will be deposited outside the masked region, but that is easily removed by sandpaper before the cathode is used.

The goal of patterning islands on the cathode was to maximize the number of triple points. Because the triple points occur all along the edges of the islands, we must quantify them as a length-density, or the total length of metal-dielectric-vacuum interfaces per unit area. The woven mesh (Mesh A) has a high theoretical triple point length-density, at 360 mm/cm^2. Due to deposition under the wires, however, the true triple point density was much lower, as discussed in section 3.3.2.1. After the disadvantages of a woven mesh were discovered, we switched to a perforated bronze mesh. Two designs were tested, but they had similar theoretical triple point length-densities, at 130 mm/cm^2 and 160 mm/cm^2 for Mesh B and C, respectively. Though this appears substantially lower, the true triple point density for these meshes, and Mesh B in particular, is very close to the theoretical value, unlike the situation for Mesh A.

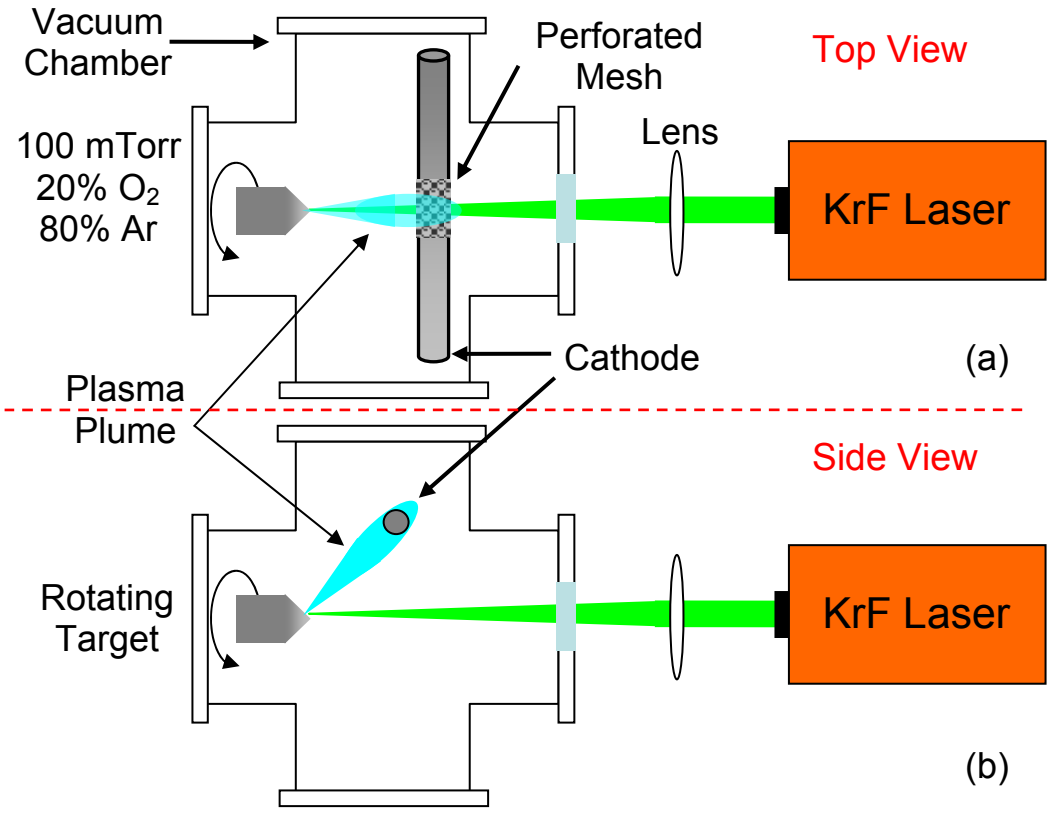

Figure 3.7 Experimental configuration for MOJ cathode fabrication.
(a) Top view of setup. (b) Side view.

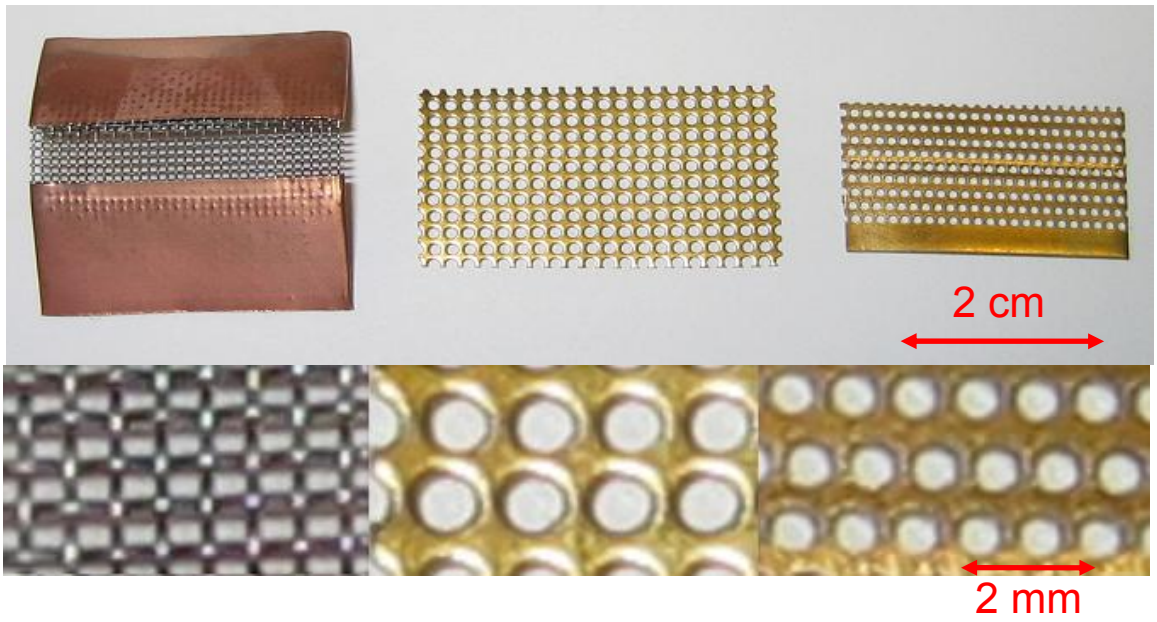

Figure 3.8 Meshes used in fabrication of MOJ cathodes. (Bottom) Close-up. From left: Mesh A, Mesh B, and Mesh C.

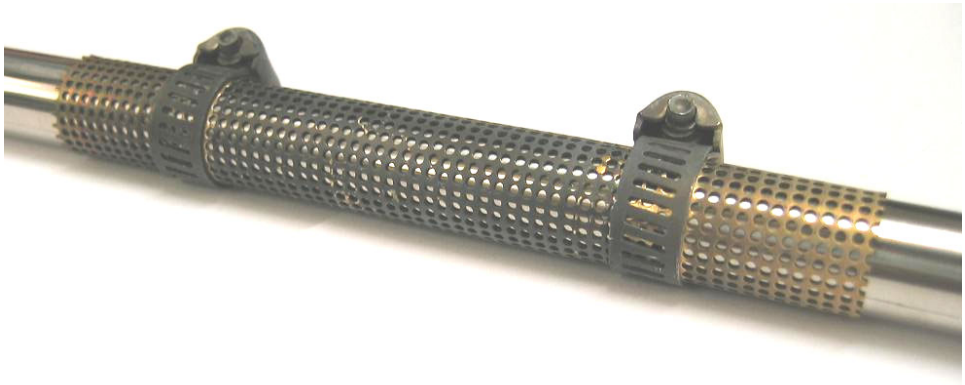

Figure 3.9 Perforated bronze mesh used in fabrication of MOJ cathodes (Mesh B).

While the ablation plume may contact the entire cathode surface, only the region closest to the target receives significant film deposition. To increase the uniformity of the film, the cathode is manually rotated 6-8 times over the course of the deposition. Each time a rotation is made, the vacuum chamber must be opened and then pumped back down to a vacuum on the 10^{-5} Torr scale. If film uniformity was of great importance, a rotating vacuum feedthrough could be installed and the cathode could be continuously rotated during deposition, eliminating any exposure to air during the fabrication process and improving the uniformity of the peak dielectric thickness.

3.3.2.1 MOJ-01 Cathode Fabrication

Unlike all other MOJ cathodes, MOJ-01 was fabricated using a woven mesh screen (Figure 3.8). The screen had 0.6 mm diameter holes, and 54% open area, labeled as Mesh A. The mesh screen was masked off, except for a 0.6 cm by 1.7 cm region, preventing the ablation plume from contacting the cathode surface outside of this small area. The total patterned area was 7 cm^2. The laser fluence was 30 J/cm^2, and 18000 pulses were used per section, resulting in a peak dielectric thickness of 900 nm. The cathode was rotated 8 times, in 45° increments, creating 8 sections. All other MOJ cathodes used 6 sections.

During ablation, because the screen is a woven mesh, collisions within the plasma cause some film to be deposited underneath the wires, reducing the effectiveness of the mask from a theoretical triple point length-density of 360 mm/cm^2 to (at best) 100 mm/cm^2. This effect is easily seen in Figure 3.10, as the dielectric “islands” are actually connected on all four sides. In this figure, the film is deposited on a flat silicon wafer, with the best mesh contact achievable. The “at best” estimate of triple point length-density is based off this figure, but on the actual MOJ-01 cathode the mesh contact was worse and many regions clearly have no dielectric separation whatsoever.

The rainbow pattern on the dielectric islands is due to the variation in dielectric thickness. This creates Newton’s Rings, with certain wavelengths of light experiencing constructive interference as they reflect off the silicon substrate. We use this effect in Chapter 5 to estimate film thickness.

MOJ-01 was ablated using a high laser fluence (30 J/cm^2), which created a large amount of surface particulate, shown in Figure 3.10 and more clearly in Figure 3.11. This particulate results from molten metal that is ejected from the ablation site during the 20 ns laser pulse. Using a shorter pulse laser, or reducing the laser fluence, will reduce the size and quantity of particulate [Chr94].

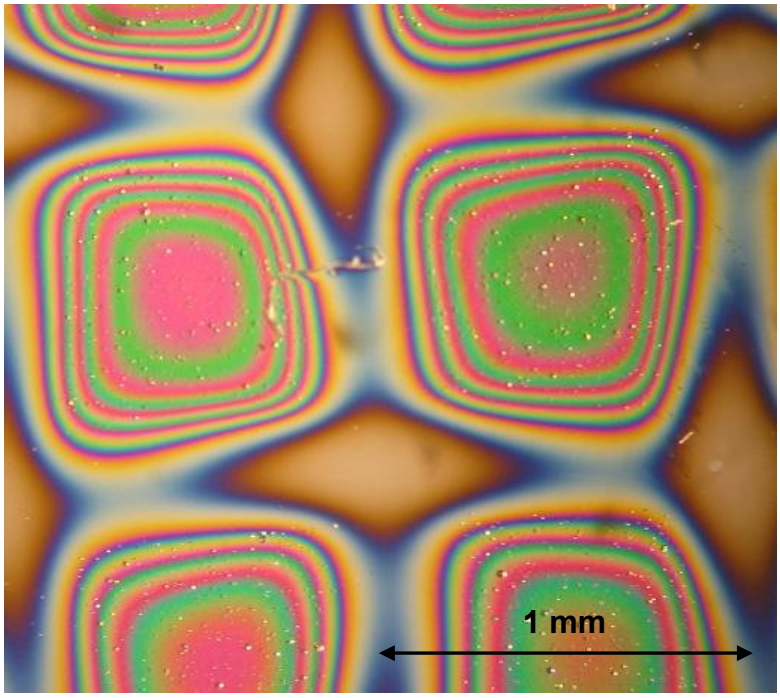

Figure 3.10: MOJ-01 test sample, deposited on silicon using Mesh A. The variation in dielectric thickness creates rainbow colored rings.

By changing the lighting angle during inspection with a light microscope, we can substantially change the image. Figure 3.10 and Figure 3.11 are images of the exact same region on the sample; the only change is the lighting angle. If the lighting angle is reduced below ~15°, the incident light will undergo total internal reflection within the dielectric, scattering only off defects and providing us with an easy method of imaging the surface particulate. From these images, we can also see that the particulate rarely deposits in the regions masked by the wire. This is because the particulate is so massive that collisions in the plasma are not able to deflect it underneath the wire mesh. The lighter ions, however, are able to change course near the cathode surface and deposit under the wires.

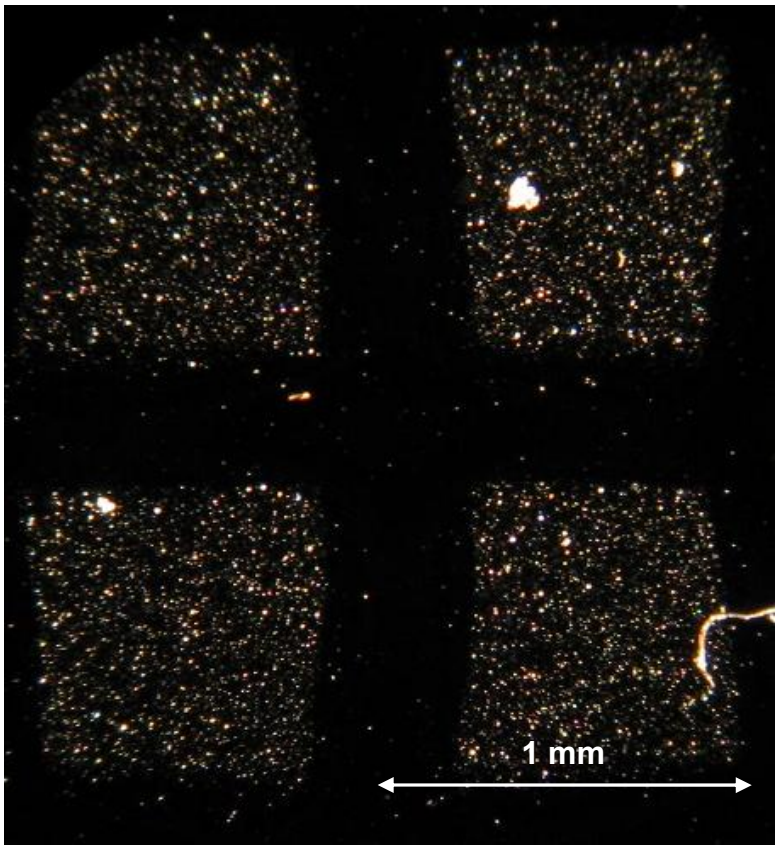

Figure 3.11 MOJ-01 test sample, deposited on silicon using Mesh A. Imaged with low lighting angle to show particulate size, density, and location.

3.3.2.2 MOJ-02 Cathode Fabrication

To improve contact between the mesh and cathode, a perforated bronze mesh (Mesh B) was used for MOJ-02. It was also wrapped completely around the cathode and clamped in place during deposition, as shown in Figure 3.9. This eliminated the need for any additional masking of the cathode during deposition. The screen used for this cathode had 1.2 mm diameter holes, and 37% open area. Switching to a perforated mesh created much more distinct dielectric islands, as shown in Figure 3.12. The laser fluence was also reduced to 1.5 J/cm^2, with 18000 pulses per section, resulting in a peak dielectric thickness of 300 nm. The patterned area was increased to 12 cm^2. This reduction in the laser fluence also greatly reduced the surface particulate, as shown in Figure 3.13. Reducing the fluence also reduced the deposition rate and, consequently, the film thickness.

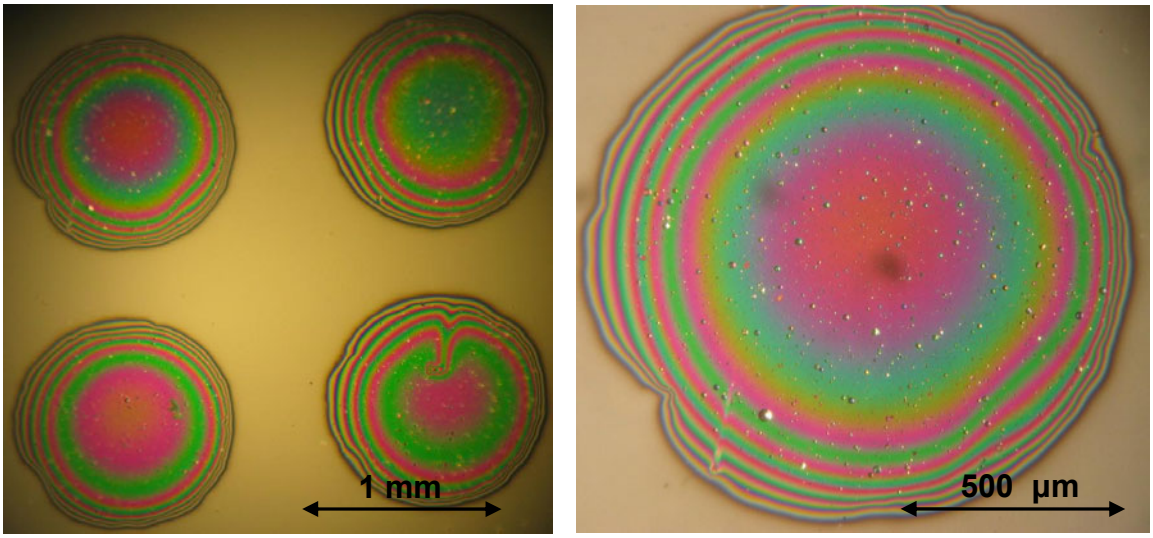

Figure 3.12 MOJ-02 pattern tested on silicon. This cathode shows more distinct dielectric islands than the woven wire mesh.

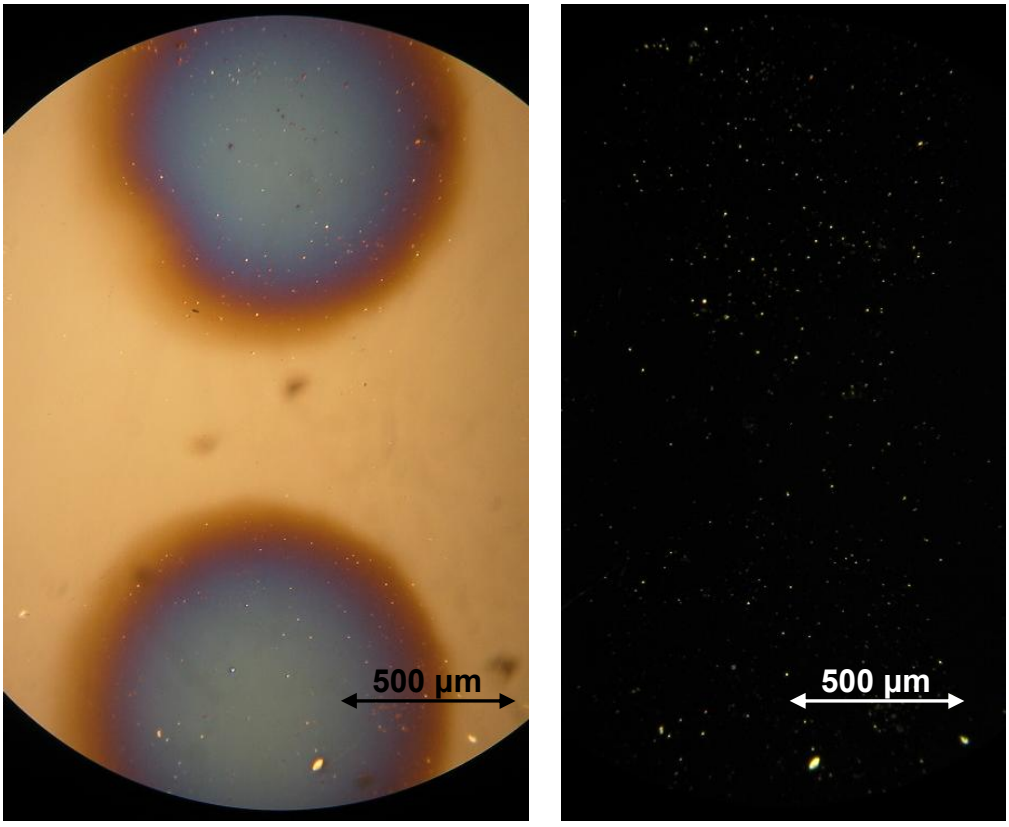

Figure 3.13 MOJ-02 sample deposited on silicon. Shows greatly reduced surface particulate.

3.3.2.3 MOJ-03 Cathode Fabrication

MOJ-03 was fabricated under similar conditions as MOJ-02. A different perforated bronze mesh was used, this one with 0.86 mm diameter holes in an

offset pattern, and 28% open area (Mesh C). This mesh, as shown in Figure 3.8, had two different hole spacings. In each row the holes were close together, but the rows were separated by a greater distance. In areas where the perforated mesh made poor contact with the cathode surface, the dielectric was deposited in rows, rather than distinct islands, Figure 3.14. The laser fluence changed slightly to 3.8 J/cm^2, resulting in a peak dielectric thickness of 450 nm. The patterned area was also increased to 28 cm^2.

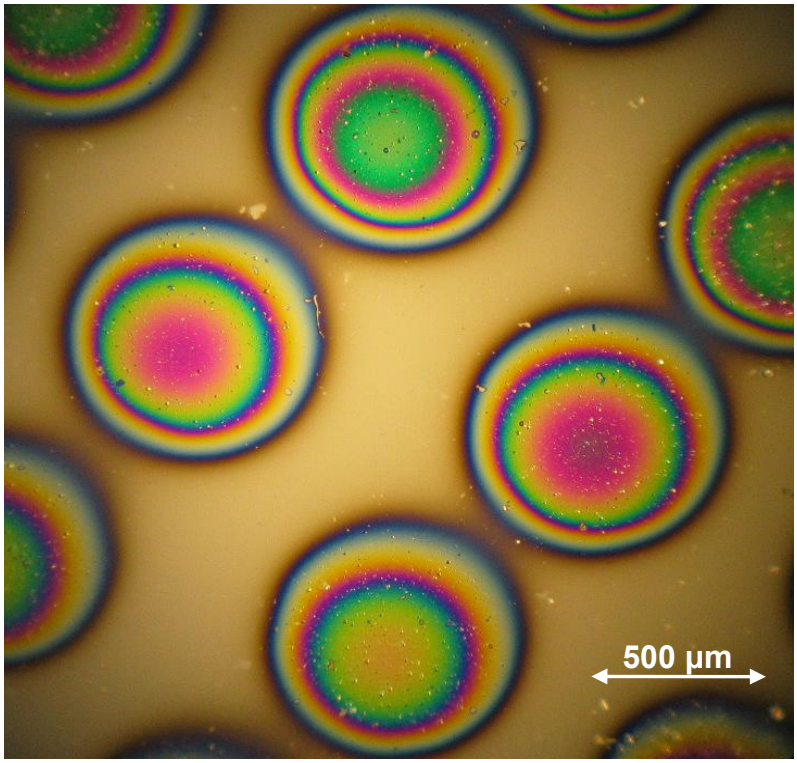

Figure 3.14 MOJ-03 test sample on silicon. This mesh resulted in dielectric rows, rather than distinct islands.

3.3.2.4 MOJ-04 Cathode Fabrication

To test the effects of particulate on cathode performance, MOJ-04 used the same mesh as MOJ-02 (Mesh B), but with a much higher laser fluence of 30 J/cm^2. This mesh was chosen because it produced the most distinct dielectric "islands." The patterned area was also increased to 34 cm^2. The increased laser fluence resulted in a large amount of particulate (Figure 3.15), as well as an increase in dielectric thickness to 900 nm.

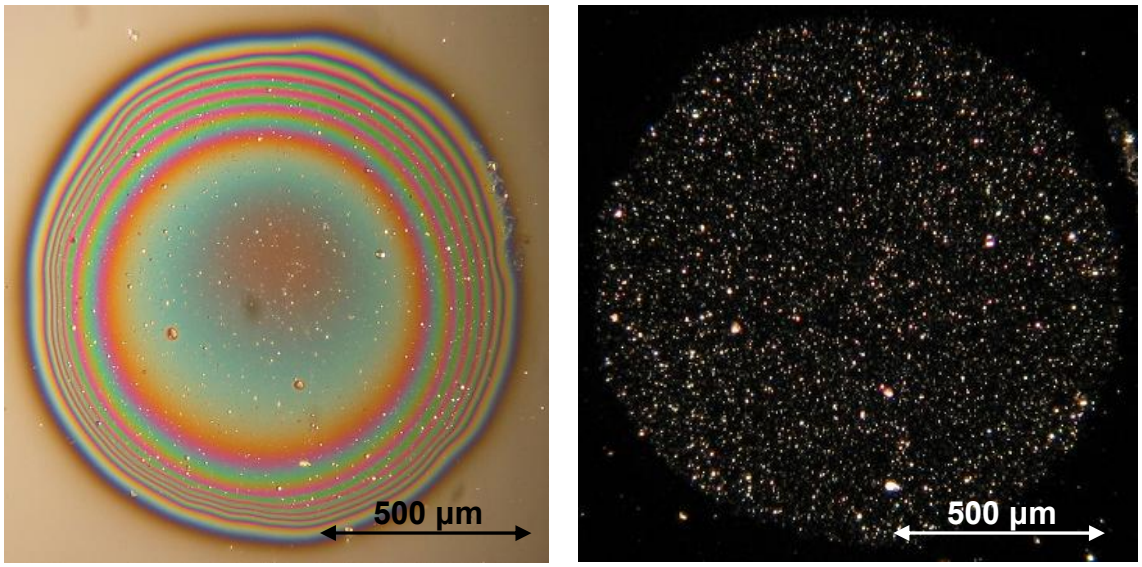

Figure 3.15 MOJ-04 test sample on silicon, using the same mesh as MOJ-02.

3.3.2.5 MOJ-05 Cathode Fabrication

As shown in Chapter 2, negative dielectric angles (defined by Figure 2.2) produce the greatest field enhancement at the triple point, and also provide the best geometries for secondary electron multiplication. For the other MOJ cathodes, collisions in the plasma plume create islands with greater dielectric thickness in the center, resulting in dielectric angles of nearly 90°, estimated from profilometer measurements. In an unsuccessful attempt to create a cathode with more ideal dielectric angles, we used 12 copper tape strips, each 2 mm thick and 7 cm long, to mask the deposition region of the cathode.

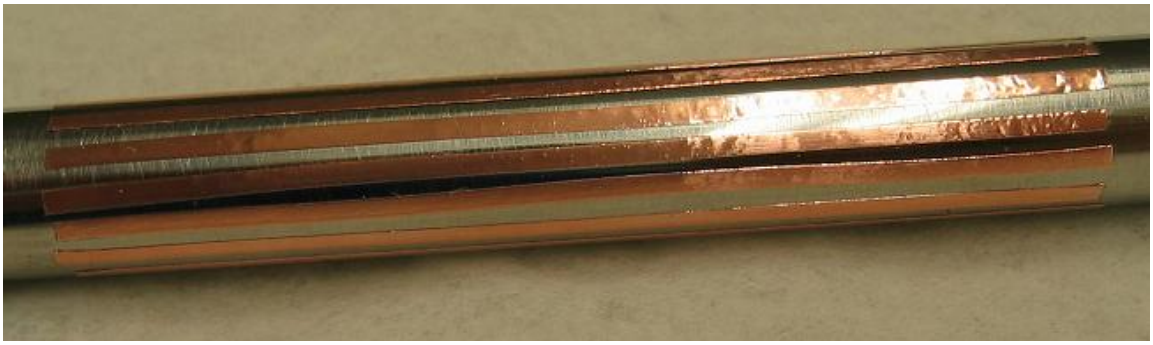

Figure 3.16 MOJ-05 cathode prior to oxide deposition. 12 copper tape strips (2mm x 7cm) encircle the emission region.

Because the copper tape has a lower profile on the surface of the cathode (compared to the bronze mesh) the oxide deposition is slightly more uniform in

the unmasked regions. The resulting dielectric angle, however, was 89°, only an improvement of ~1°. The geometry of the copper strips does, however, provide a lower triple point length-density, at 60 mm/cm^2, smaller than any other MOJ cathode. The cathode was patterned with a laser fluence of 26 J/cm^2, using 4 sections and 18000 pulses per section, resulting in an estimated peak thickness of 900 nm.

3.3.2.6 MOJ-06 Cathode Fabrication

To examine the role of secondary electrons in electron emission for the MOJ cathodes, we fabricated a cathode using a magnesium oxide (MgO) target instead of HfO_2. MgO has a high secondary electron emission (SEE) coefficient, measured in the literature to range from 17-25 [Whe58]. While the SEE coefficient of HfO_2 is unknown, SEM measurements in Chapter 5 qualitatively indicate it is similar to copper, which has a SEE coefficient of ~2 [Bag00].

The cathode was fabricated using Mesh B, at a laser fluence of 7 J/cm^2 and a repetition rate of 10 Hz. The deposition was performed in 6 sections, with 18000 pulses per section, similar to previous MOJ cathodes. To improve mesh contact, the patterned area was decreased to 20 cm^2. The use of an oxide (rather than metallic) target allowed the deposition to be performed in a vacuum of 2x10^{-5} Torr. Because the target was a 1 cm^3 MgO crystal, the standard aluminum pyramid could not be used, and a new target holder was fashioned, as shown in Figure 3.17.

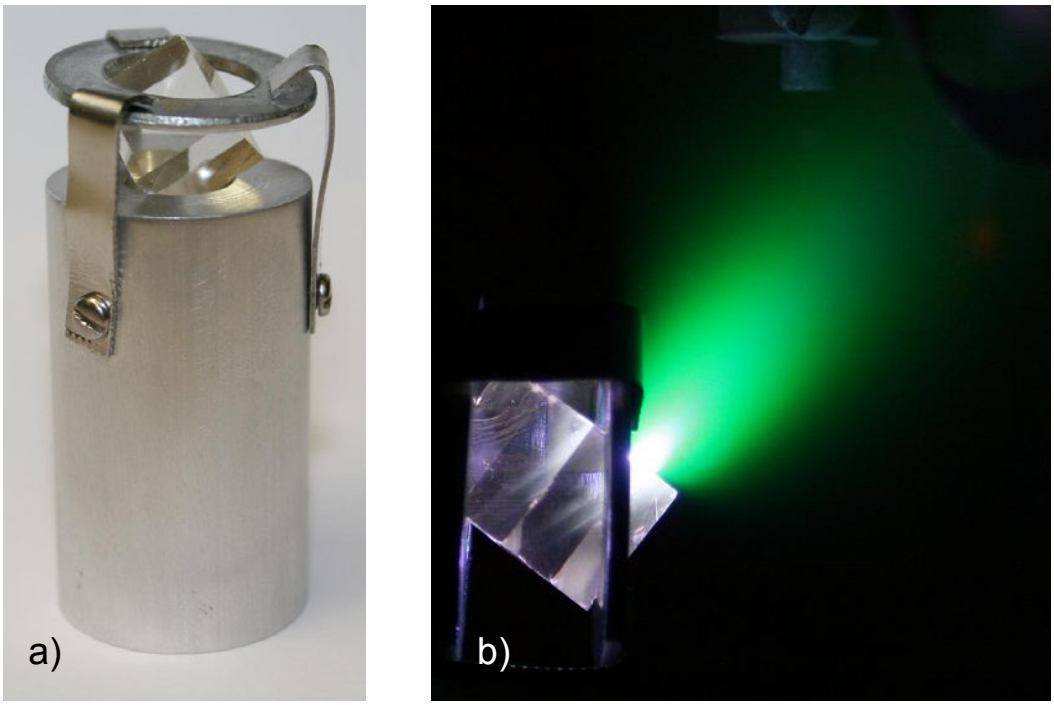

Figure 3.17 (a) Target holder for MgO substrate. (b) 1 cm^3 MgO target and plume during ablation. The cathode is in the upper-right corner, 2.5 cm from the ablation target.

These deposition conditions produced an MgO film with a peak thickness of 900 nm. This thickness is similar to previous MOJ cathodes, despite using much lower laser fluence. This may be explained by the reduced target-substrate gap, which was 2.5 cm, compared to ~3 cm for previous cathodes. A smaller gap provides higher peak thickness, but also decreases the uniformity of the film thickness. Individual dielectric islands showed improved uniformity, easily seen on the left side of Figure 3.18. The entire top of the island has as very similar color (thickness), and the edges show rapid color change. This increase in uniformity is likely because Mg is much lighter than Hf, and is more easily scattered by collisions in the plasma plume.

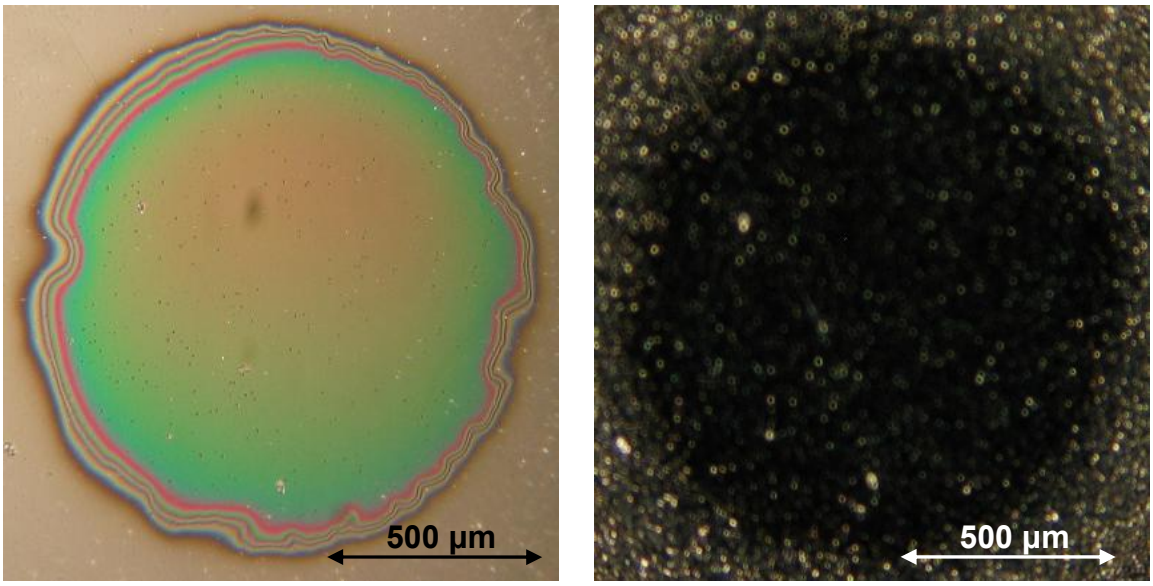

Figure 3.18 A single dielectric island from the MOJ-06 test sample on silicon, using Mesh B. (Left) High lighting angle showing dielectric. (Right) Low lighting angle showing particulate.

3.3.3 Control Cathodes

To test the effectiveness of our cathode patterning techniques, several "baseline" cathodes were fabricated and tested in the relativistic magnetron.

3.3.3.1 Polished Stainless Steel (PSS) Cathode

The most obvious cathode test is that of a sanded T304 stainless steel hollow rod, identical to the substrate used in the fabrication of MOJ cathodes. Type 304 stainless steel is an austenic steel alloy consisting of 0.15% carbon, 2% manganese, 0.045% phosphorus, 0.03% sulfur, 1% silicon, 19% chromium, 9.25% nickel, and 68% iron [Hen07]. Tests of this cathode give an indication of the cold-cathode emission currents obtained without any form of cathode patterning. Fabrication of a PSS cathode is fairly straightforward; 91.4 cm long tubes of T304 stainless steel are cut into 27.4 cm lengths and 2 mm slots are cut into each end. These slots ensure no gas will be trapped inside the hollow cathode when the magnetron is pumped down. When the full cathode is assembled, the slots are covered by the electrostatic endcaps, so they do not affect the cathode's emission properties. The cathodes are rotated in a lathe while being sanded with sandpaper ranging from 600 to 2500 grit, a process that

normally takes 40 minutes. The surface finish shown in Figure 3.19 is the typical end result.

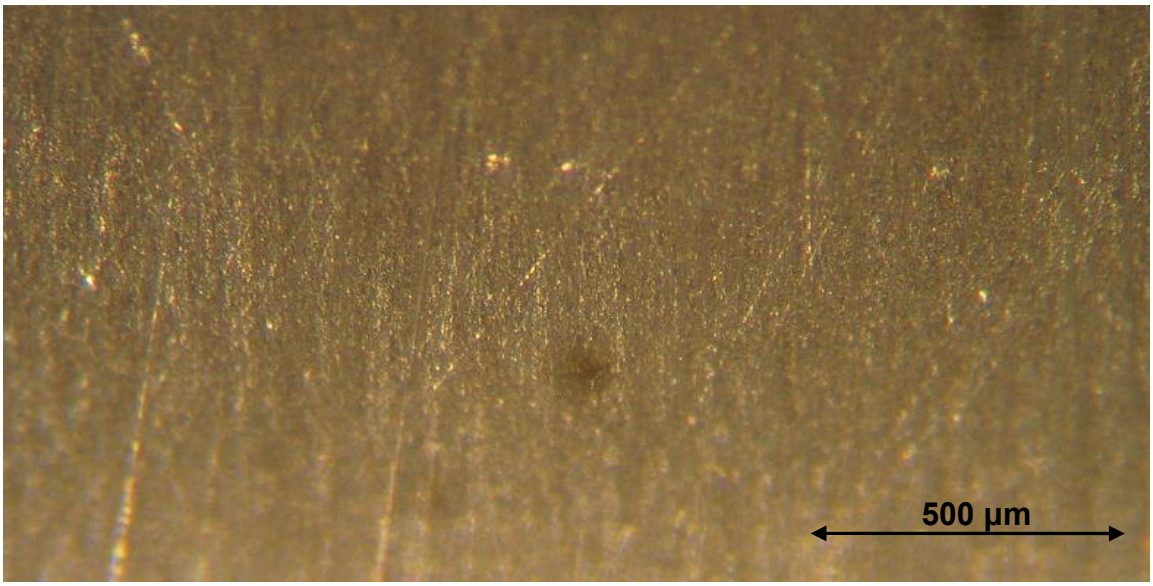

Figure 3.19 Light microscope image of the final surface of a polished stainless steel cathode. This is the typical stainless steel substrate surface finish of all MOJ cathodes before patterning. 20X magnification.

Three of these cathodes were fabricated and tested at various times (Table 6.1); this was done to check if anything had changed in the general magnetron operation or diagnostics.

3.3.3.2 Dielectric Coated Cathode

To ensure that the bulk dielectric was not enhancing electron emission from the MOJ cathodes, a fully dielectric coated cathode was fabricated. The patterned region was 12.5 cm long, resulting in a total patterned area of 50 cm^2. The hafnium oxide film was deposited in 4 sections (compared to 6-8 for MOJ cathodes), at 9000 pulses per section, with a laser fluence of 30 J/cm^2, resulting in a peak dielectric thickness of 500 nm.

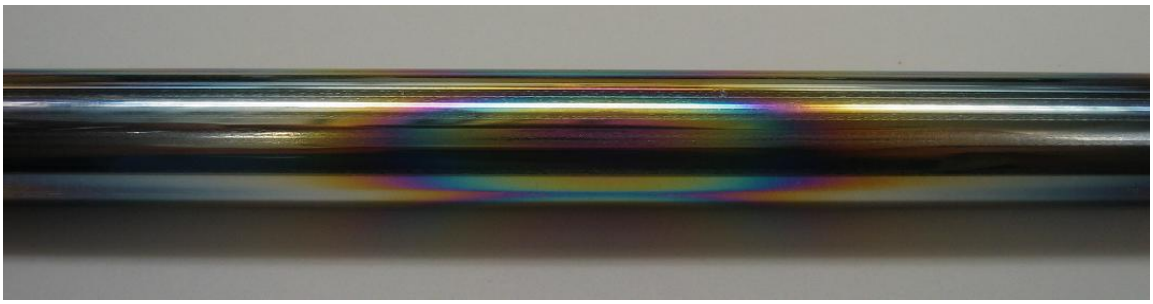

Figure 3.20 Photograph of the patterned region of the dielectric coated cathode. The cathode diameter is 1.77 cm.

3.3.3.3 Metal Island Only (MIO) Cathode

To ensure that the metal particulate was not enhancing electron emission simply by creating field emission sites on the MOJ cathodes, we fabricated a cathode with metal-only islands. This cathode was patterned in a $2x10^{-5}$ Torr vacuum, using Mesh B, with 6 sections, and 12000 laser pulses per section. The laser fluence was 15 J/cm^2, resulting in a peak film thickness of 1000 nm. Despite our best efforts to eliminate the formation of an oxide, a small amount of oxidation can be seen around the edges of each island, Figure 3.21. Hafnium forms a very thin (~1 nm) oxide layer with room temperature exposure to air, and impurities within the hafnium target may also contribute additional oxygen during the deposition process. This thin film, however, should be removed after the first few shots in the magnetron.

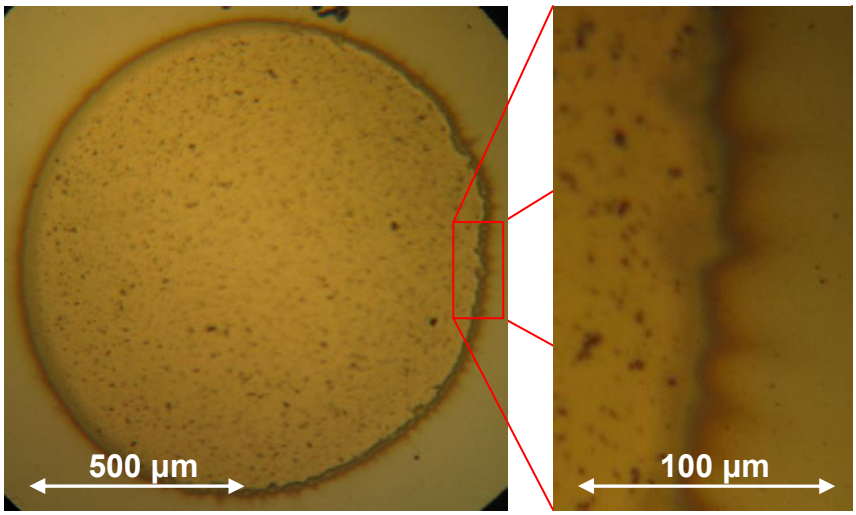

Figure 3.21 Single island on the MIO-1 test sample, deposited on silicon. Zoomed region shows the formation of a thin oxide layer.

Treating the particulate as a hemisphere of metal in conductive contact with the cathode surface, basic electrostatics shows the electric field enhancement, β, is 2 at the tip of each particle.

CHAPTER 4
EXPERIMENTAL CONFIGURATION AND DIAGNOSTICS

The UM/Titan relativistic magnetron, located in the Plasma, Pulsed Power, and Microwave Laboratory at the University of Michigan, is a modified A6 magnetron driven by the Michigan Electron Long Beam Accelerator (MELBA). MELBA is capable of producing voltages of up to -1 MV and pulses up to 1.5 μs long. For the MOJ and ALF cathode tests, however, -300 kV pulses were used, with typical pulse lengths of 300-400 ns. This chapter describes the experimental configuration of the magnetron and accelerator, as well as the configuration and calibration of the relevant diagnostics.

This chapter also details the spectroscopic setup used to acquire the spectra shown in Chapter 5. An Acton -300i spectrometer images plasma plumes ablated from flat hafnium targets. This configuration simulates the conditions used during cathode preparation, allowing us to image the plasma without a complicated optical setup.

4.1 Spectroscopy

Spectroscopy data are obtained by expanding the image of the ablation plume onto the entrance slit of the Acton Research Corporation -300i spectrometer. A 12.5 cm diameter, 34 cm focal length lens is placed between the plume and spectrometer; 42.5 cm from the plume, and 151 cm from the spectrometer. This results in an image magnification of 3.5x at the spectrograph. With a spectrograph slit width of 7 μm, this corresponds to a plume width of 2 μm.

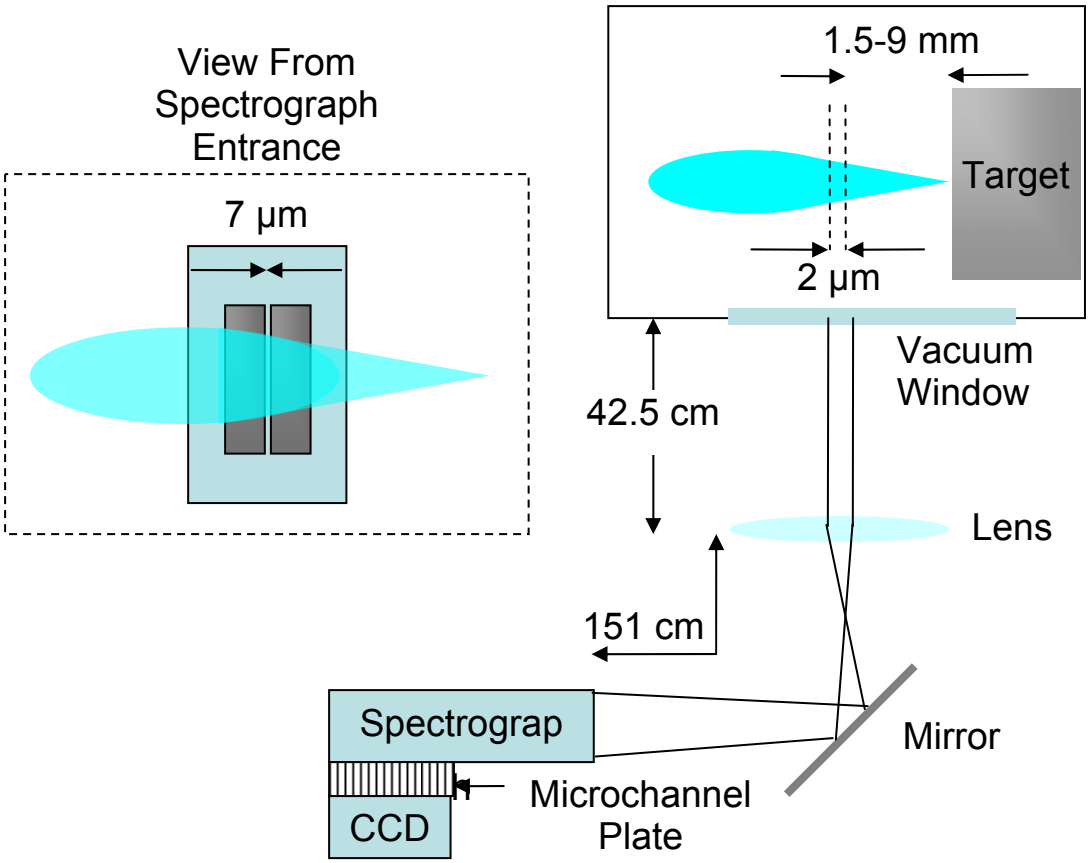

Figure 4.1 Spectroscopy setup, showing the magnification of the ablation plume onto the spectrograph entrance.

As shown in Figure 4.1, the image is reflected off a mirror before entering the spectrograph. It is important that this mirror reflects light perpendicular to the entrance of the spectrograph. If the light enters at an angle, the intensity will be reduced and shifting of the spectral lines may occur.

Images are captured by a Princeton Instruments intensified CCD camera (model # ICCD-576/RB-EM), which is gated by a Princeton Instruments Detector Controller. Gate widths of 50 ns to 10 ms are possible, with 50 ns used for all experiments reported here. The pulse timing is controlled by a BNC 555-4 pulse generator, which triggers the excimer laser and then, after an adjustable delay, triggers the PI Detector Controller to send a gate pulse, Figure 4.2.

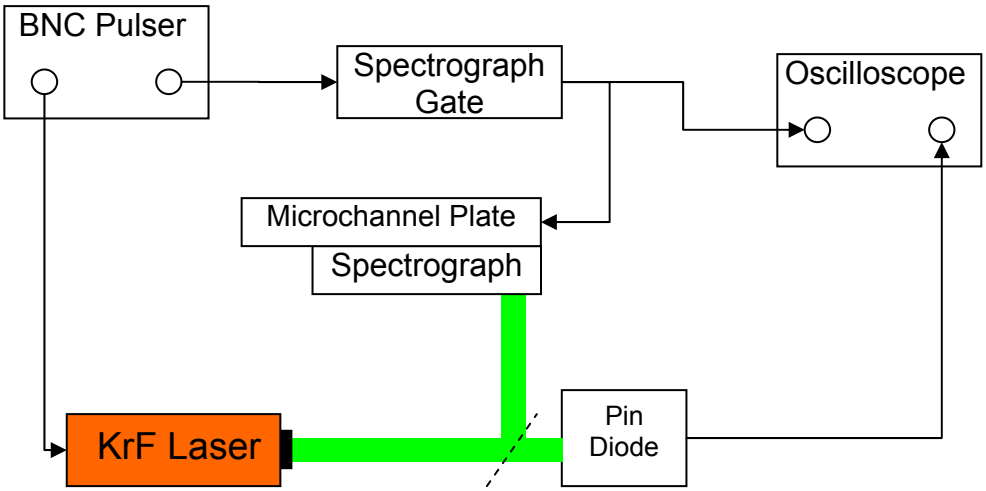

Figure 4.2 Spectroscopy timing and triggering.

Timing is confirmed using a pin diode and the gate pulse, which are both sent to a TDS 3052 oscilloscope, sample traces are shown in Figure 4.3. The pin diode has an additional 45 ns of cable delay, which has been accounted for in Figure 4.3. This figure shows the true spectrograph gate delay (100 ns), which results from a 50 ns delay on the PI Detector Controller and an 1100 ns delay on the BNC 555. The pulse width is 50 ns.

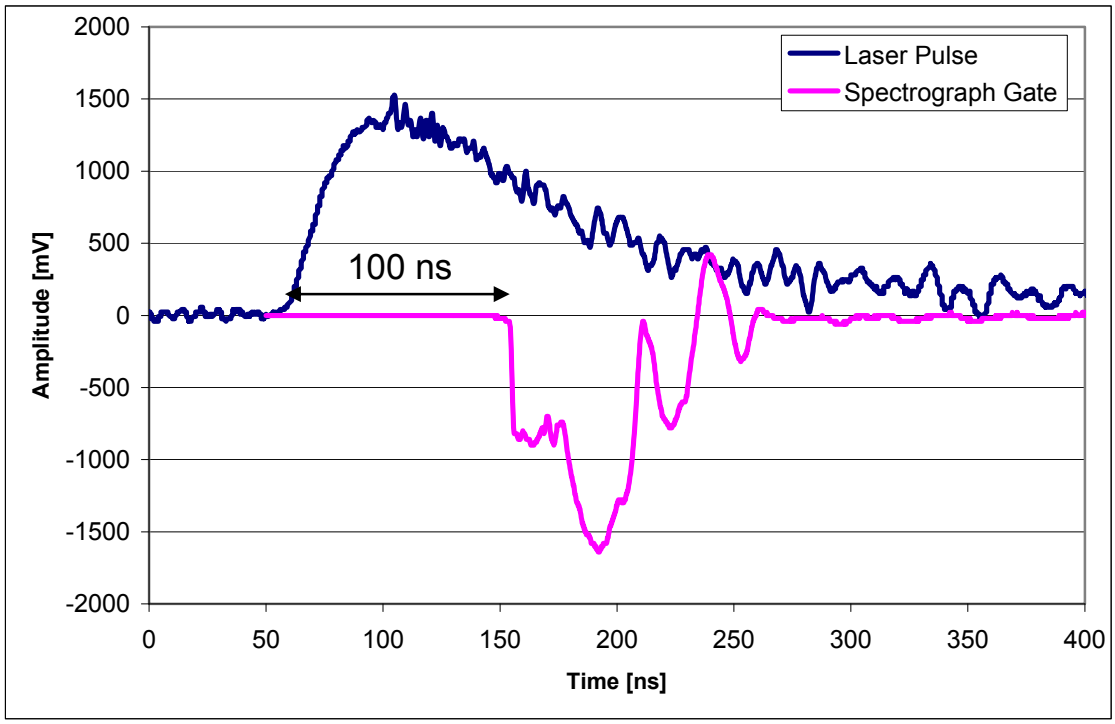

Figure 4.3 Sample pulses for spectroscopy timing showing that 1150 ns of total programmed gate delay gives a 100 ns true delay.

4.2 Relativistic Magnetron

Cathode experiments are performed on a 6-vane modified A6 relativistic magnetron from L-3/Titan Pulse Sciences. This L-band magnetron is driven by the Michigan Electron Long Beam Accelerator (MELBA), generating frequencies on the order of 1 GHz. The rounded anode vanes are 20.5 in length, at an anode radius, r_a, of 3.2 cm. The cathode radius, r_c, is 0.635 cm and the outer cavity radius, r_m, is 8.26 cm, as shown in Figure 4.4.

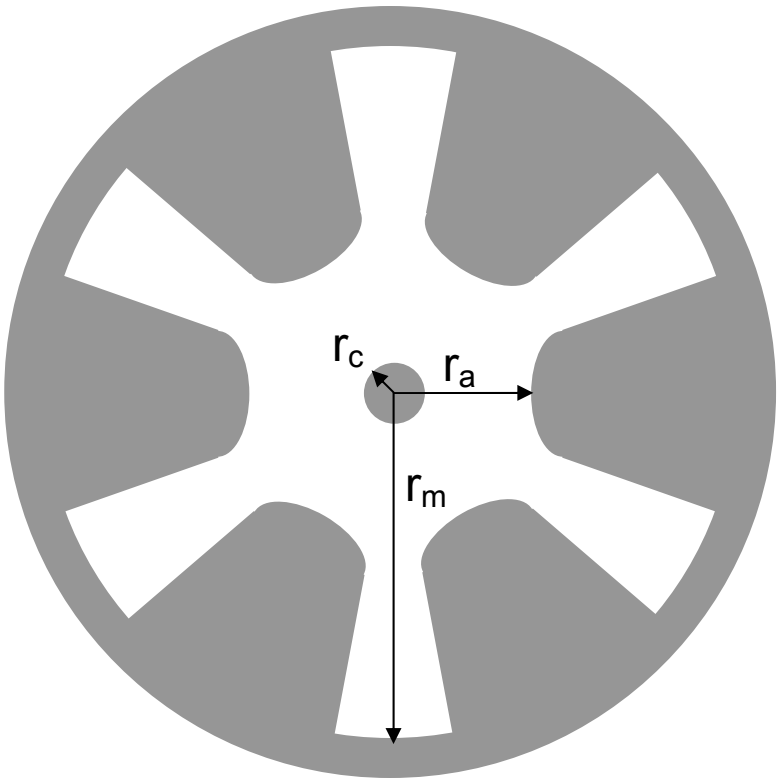

Figure 4.4 Diagram of the on-axis view of the L-3/Titan relativistic magnetron, showing rounded vanes and cavity dimensions.

Figure 4.5 shows a view of the interaction cavity, taken from the end of the magnetron opposite the accelerator. Between each vane is a coupling slot for microwave extraction. Two slots are terminated with steel plates, one slot has a steel plate with a 2" glass viewport, while the other three slots (spaced 120° apart) are covered by 1.1 cm thick Lucite windows.

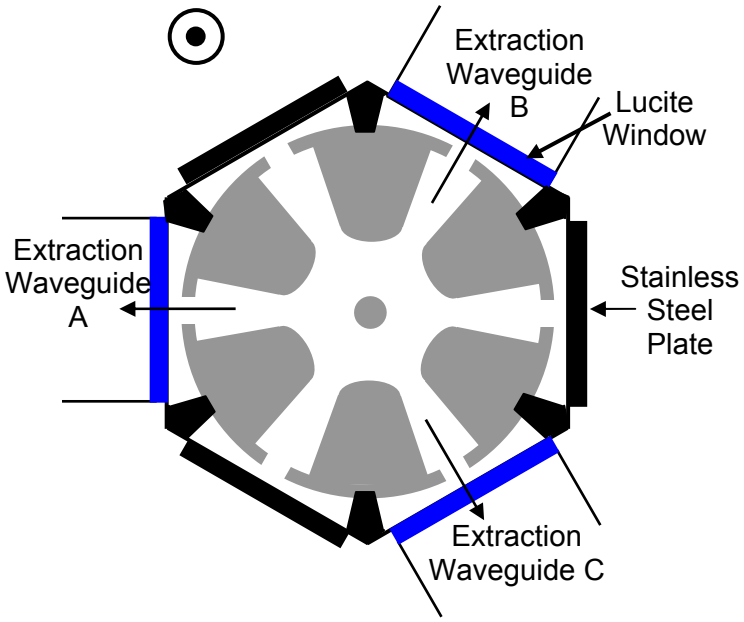

Figure 4.5 Magnetron diagram showing coupling slots and extraction windows.

These windows allow microwave transmission while maintaining the magnetron's internal vacuum. Because of the large microwave powers produced, breakdown can occur across the windows, damaging the windows and leaving electron tracks. An example of a damaged window is shown in Figure 4.6.

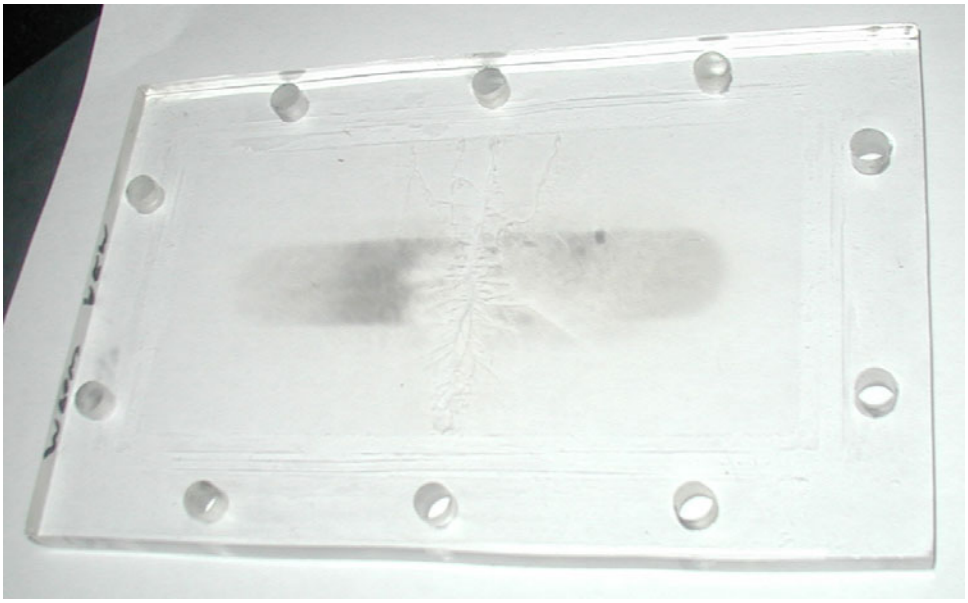

Figure 4.6 Output waveguide window exhibiting breakdown on the vacuum-side of the window. The dark outline shows the size and shape of the magnetron coupling slots.

Attached to all three Lucite windows are L-band waveguides with internal dimensions of 16.51 cm by 8.255 cm. L-band (WR-650) waveguides have a lower cutoff frequency of 0.91 GHz, and are recommended for operation in the 1.12 -1.7 GHz range. Consequently, the typical operational frequency of the UM magnetron is below the recommended range, but above the cutoff frequency. All three waveguides connect to -50 dB microwave power couplers, and then terminate in carbon-coated horsehair loads.

The magnetron, with the MELBA-C ceramic insulator, is held at a typical vacuum pressure on the 10^{-7} torr scale, though pressures as low as 6×10^{-8} torr have been achieved [JON05]. This is achieved with a rotary pump (200 l/min), for initial pumping, coupled with a CTI Cryogenics cryo-pump (1500 l/s).

4.3 Accelerator

MELBA has been used in experiments at the University of Michigan since 1984 [Gil85, Lop03], and at the time of this publication, has fired over 12000 shots. In 2002, the plastic insulator stack was upgraded to a ceramic stack, with over 1900 shots fired since the upgrade. Since the upgrade, MELBA is referred to as MELBA-C. The accelerator components are shown in Figure 4.7, and all components are fully submerged in transformer oil. The 16 capacitors (1 uF, 100 kV) are charged in parallel and discharged in series through the 7 spark gap switches. Two of the 16 capacitors are charged with reverse polarity, and help flatten the voltage pulse in a configuration known as an Abramyan circuit [Abr77, Jon05]. Series resistors, liquid copper sulfate resistors, and filter capacitors comprise the remainder of the accelerator circuit. A circuit diagram is included in Appendix A [Jon05]. Typical pulses produce 1-10 kA of current at -300 kV, with pulse lengths ranging from 200 to 500 ns. MELBA-C is capable of producing pulses 0.1-1.5 μs in length. However, in order to protect the magnetron in the event of plasma closure, the pulse is shortened via an adjustable command crowbar switch to about 0.3-0.5 μs.

a)

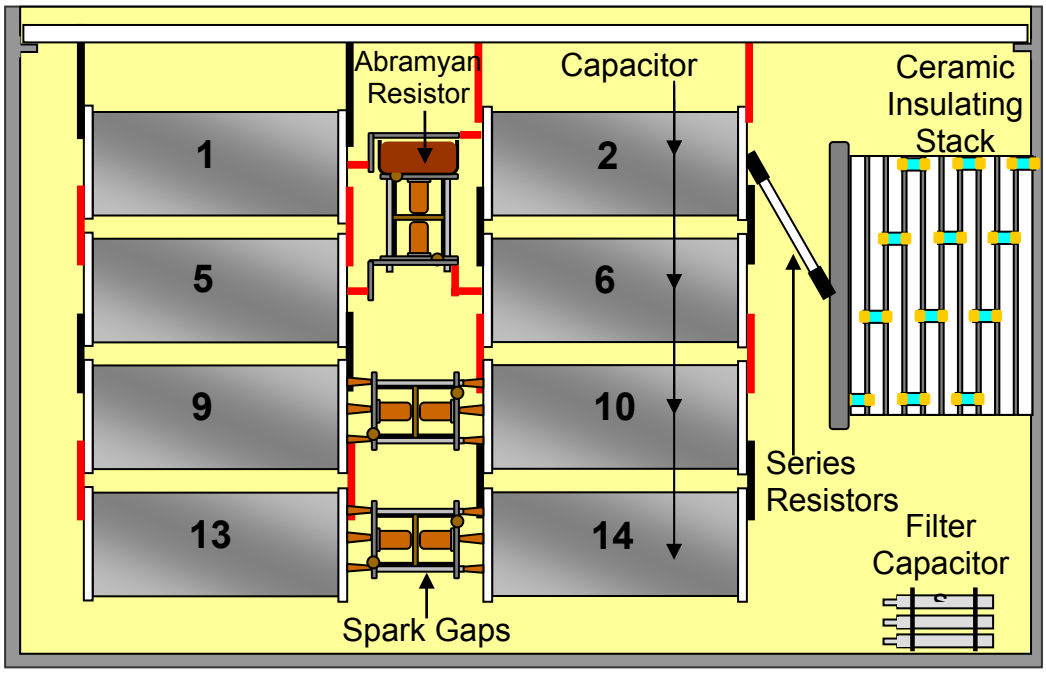

b)

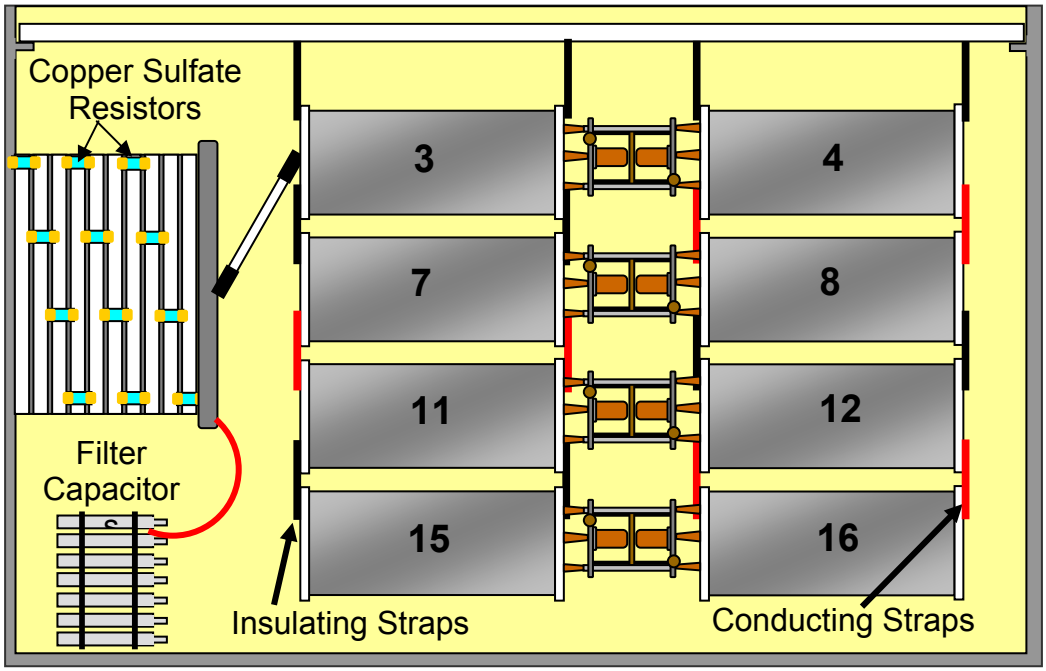

Figure 4.7 Diagram of MELBA-C, showing ceramic insulator stack, filter capacitors, charging capacitors, spark gap switches, series resistors, and the Abramyan resistor a) As seen from the west. b) As seen from the east. [modified image from Jon05]

4.4 Electromagnets

Two pulsed electromagnetic coils, provided by AFRL, produce an axial magnetic field for the magnetron, typically on the order of 2-3 kGauss. However,

due to size constraints and the magnetron geometry, the magnets cannot be placed in a Helmholtz configuration (magnet separation equal to magnet radius), which would produce the most uniform magnetic field between the coils.

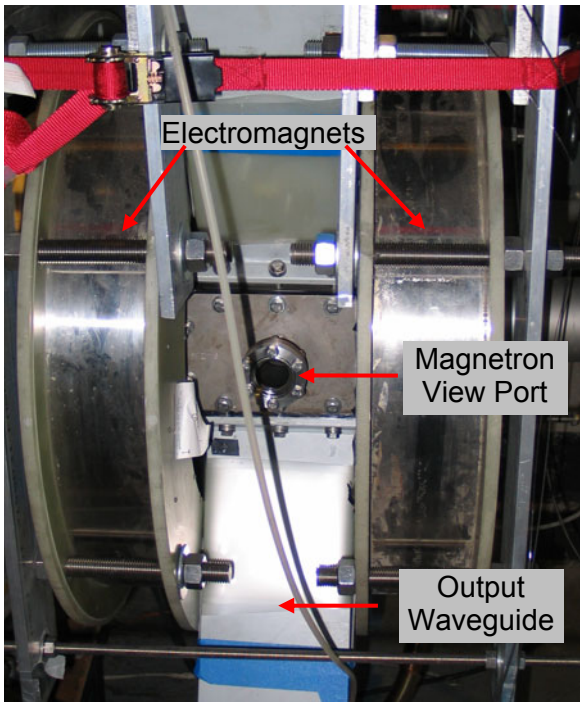

Figure 4.8 Picture of electromagnets and magnetron view port. The magnets make direct contact with the extraction waveguide, defining the minimum separation.

The axial magnetic field, however, remains sufficiently uniform over the interaction region in the center of the magnetron [Lop03]. The magnet is pulsed with 2.8-4.6 kV, generating 600 to 900 A of current and axial magnetic fields of 2.0-3.0 kGauss. Due to eddy currents in the magnetron body (magnetic diffusion), the magnetic field on axis will not be as large as basic solenoid equations would predict, and the peak field is delayed by ~4 ms (compared to the peak current in the coils). To correct for this, calibrations were performed using a Lakeshore 420 Gaussmeter, and the MELBA-C trigger pulse is delayed by 8.2 ms. This ensures the Marx trigger occurs at the maximum magnetic field.

4.5 Diagnostics & Calibrations

For each relativistic magnetron shot, the entrance current, end-loss current, magnet current, and cathode voltage are recorded, as well as the

microwave power in all three extraction waveguides. This section details the setup and calibration of these measurements.

4.5.1 Electrical Diagnostics

4.5.1.1 Cathode Voltage

The cathode voltage is measured via a $CuSO_4$ voltage divider installed on the ceramic insulator stack, inside the oil tank of the accelerator. The probe is designed as a 100,000:1 resistive divider, but this value may change if air bubbles form near any of its electrodes. This effect is easily noticed during MELBA-C runs, as the measured voltage can change dramatically, sometimes appearing to increase beyond the Marx erection voltage.

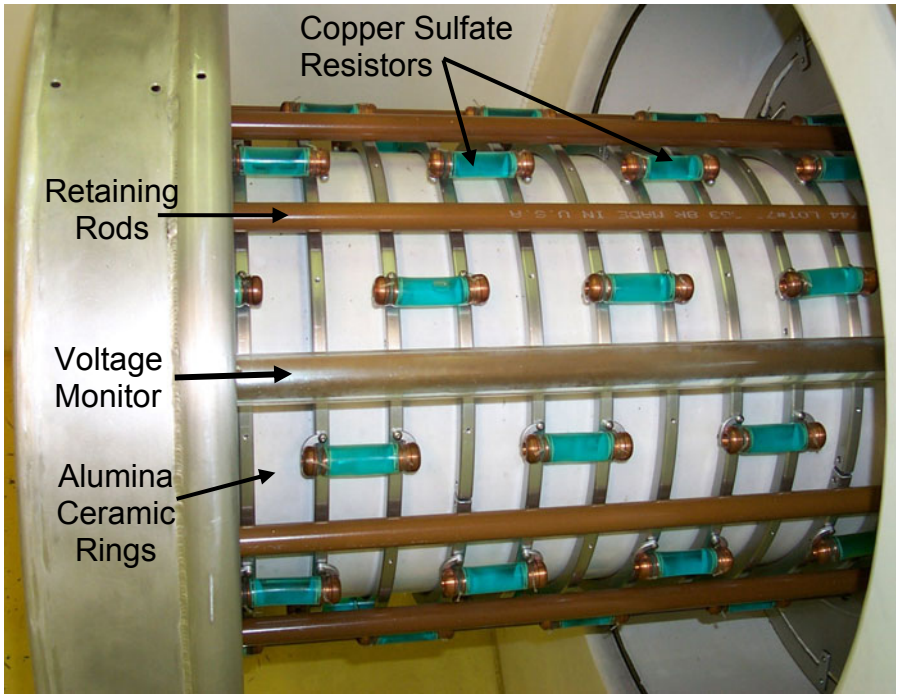

Figure 4.9 MELBA-C ceramic insulating stack with copper sulfate resistors and voltage monitor.

To calibrate the high voltage probe, a circuit was constructed as shown in Figure 4.10. The cathode stalk was biased with high voltage pulses, produced by the BWH pulser, a double-module Febatron. These pulses ranged in magnitude from 28 to 41 kV. This voltage was then directly measured with a North Star PVM-5 high voltage probe, and recorded on a nearby scope. The cathode voltage was simultaneously measured by the standard screen room

setup. All scope channels in the screen room were terminated in 50 Ω and 10x attenuators, consistent with the setup for all MELBA-C shots. Comparing the two measured voltages gives a calibration constant of 84.6 kV/V, as shown in Figure 4.11.

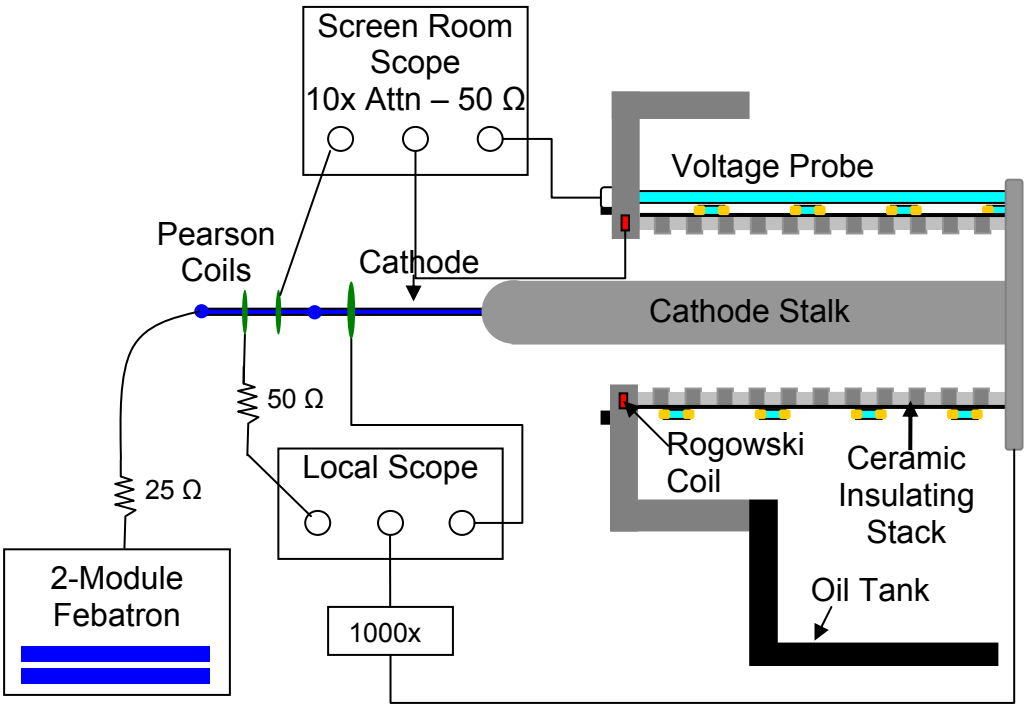

Figure 4.10 Experimental circuit for current and voltage calibrations.

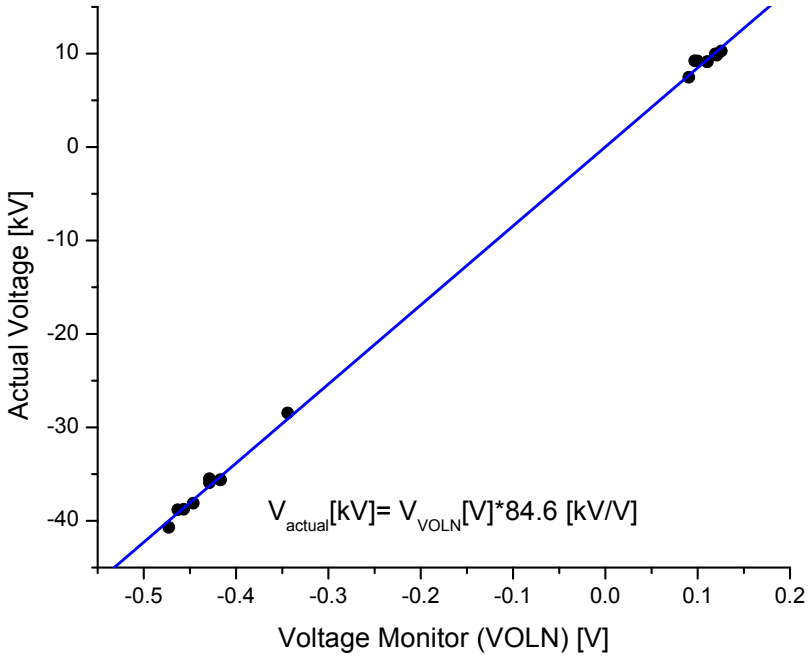

Figure 4.11 Voltage calibration for MELBA-C, performed by Brad Hoff and Nick Jordan, 03-29-2007. The R-value of the fit was 0.99.

4.5.1.2 Cathode Current

The current produced at the surface of the cathode is divided into two measurements. The primary measurement is the entrance current (ENTC) which is measured by the large (PSI installed) Rogowski coil imbedded in the magnetron side of the insulating stack. The secondary measurement is the end-loss current (PEAR), which is measured by a Pearson coil surrounding a grounding strap connected to a Poco graphite collector. This collects electrons that escape the magnetron in the axial direction.

Calibration of the Rogowski coil was conducted using the circuit shown in Figure 4.10. During the calibration, endloss is obviously not a consideration, and only the ENTC channel is calibrated, as it corresponds to the output voltage of the Rogowski coil. Two pre-calibrated Pearson coils provide a measurement of the current, which is recorded on a nearby scope. The ENTC signal is simultaneously measured in the screen room through the standard cable length, 10x attenuation, and 50 Ω termination. The Pearson coils self-integrate the signal, producing output voltage directly proportional to the current, while the Rogowski output voltage is actually proportional to dI/dt. After integrating the

ENTC signal, the currents were plotted and fitted to produce a calibration factor of 1.32 x 10^{10}, as shown in Figure 4.12; this is noticeably lower than the previously measured factor of 3.0 x 10^{10} [Lop03].

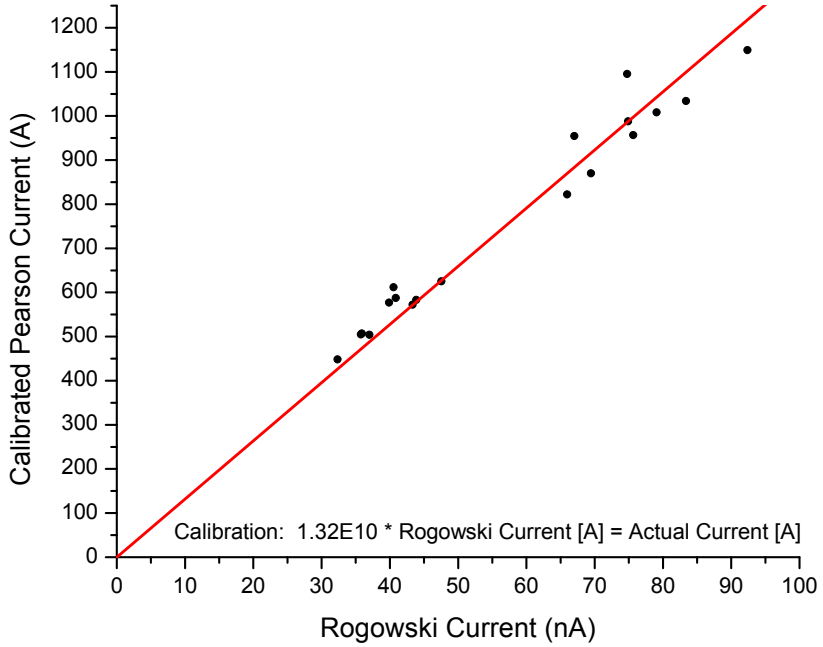

Figure 4.12 MELBA-C current calibration performed by Brad Hoff and Nick Jordan, 02-20-2007. The R-value of the fit was 0.98.

4.5.1.3 Magnetic Field

The magnet current (called BLUE) provides a measurement of the magnetic field within the magnetron. The magnet current is calibrated by charging the magnet capacitors, pulsing the magnets, and recording the internal magnetron magnetic field with a Lakeshore 420 Gaussmeter while simultaneously recording the magnet current in the screen room (via a Pearson coil). This gives a direct relation between the magnet current and the magnetic field within the magnetron, as shown in calibration data taken by B. Hoff, Figure 4.13.

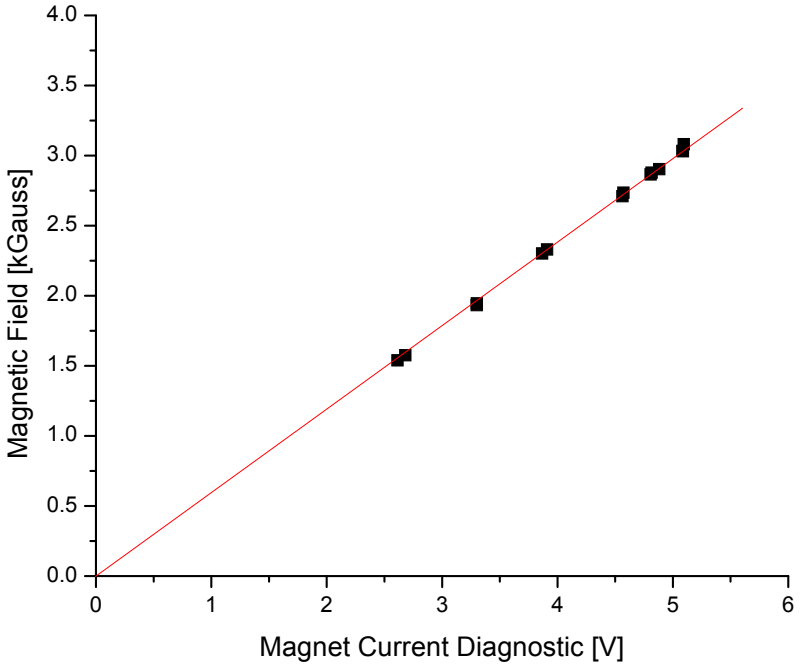

Figure 4.13 Relationship between magnetic field on-axis in the magnetron and the measured voltage from the magnet current diagnostic, 4-19-2007. The R-value of the fit was 1.00.

By observing the time of the peak current and the time of the peak magnetic field, the penetration time for the magnetic field can also be calculated, and the appropriate delay (8.2 ms) can be programmed into the MELBA-C triggering system. This will ensure the accelerator is fired in sync with the maximum magnetic field.

4.5.2 Microwave Diagnostics

Microwave signals are measured through all three extraction waveguides, and recorded as channels MPOV, MPOX, and MPOW. A directional loop-coupler placed in each extraction waveguide samples the microwaves at -50 dB, and passes the signal to the screen room, where it undergoes another -35 dB of attenuation. The resultant microwave signal is passed to a HP8472B diode detector, which rectifies it to a voltage signal readable by the oscilloscopes. Calibration of the diode detector was performed by M. C. Jones [Jon05].

The typical microwave frequency of the relativistic magnetron (1 GHz) is beyond the capability of the 500 MHz oscilloscopes. To circumvent this, a zero-area B-dot loop is placed in the MPOV extraction waveguide. The RF signal

from this B-dot loop is heterodyned with a local oscillator at a known frequency, typically between 1.1 and 1.3 GHz. This produces a difference frequency within the oscilloscope bandwidth, and the frequency of the original signal is determined by processing the heterodyned signal in a time-frequency analysis (TFA) program, provided by Quantum Signal, LLC [Pet98, Jon05].

CHAPTER 5
MATERIALS AND PLASMA ANALYSIS

The composition and characteristics of the plasma during cathode deposition can affect the surface properties of the completed cathode. Those surface properties, in turn, can greatly impact the cathodes' performance and longevity. In this chapter, we employ optical emission spectroscopy to obtain an estimate of plasma temperatures and ionization states. For the ALF cathodes, we obtain information about surface features from mechanical profilometry and Scanning Electron Microscopy (SEM). For the MOJ cathodes, film composition is also an important consideration, and we use X-ray Energy Dispersive Spectroscopy (XEDS), coupled with SEM, to gain an understanding of the film stoichiometry. X-ray diffraction provides some information about the crystal structure of the films, while capacitance-voltage measurements indicate the severity of defects both within our films and at film boundaries.

5.1 ALF Cathode Materials

The Ablation Line Focused (ALF) process results in a ring of ablation trenches approximately 300 μm wide, and 1.5-2 cm long. These trenches are separated by un-ablated regions 100 μm wide. This results in 100 ablation trenches encircling a 1.27 cm diameter cathode. Many rings can be patterned next to each other to give the desired total emission area.

Figure 5.1 Ablated region of ALF-4b cathode showing "stacked" ablation rings to give 38 cm^2 of total emission area.

A SEM image of a single trench is shown in Figure 5.2, with a depth of 40 μm below the original cathode surface, as measured by a step profilometer with a diamond-tipped stylus.

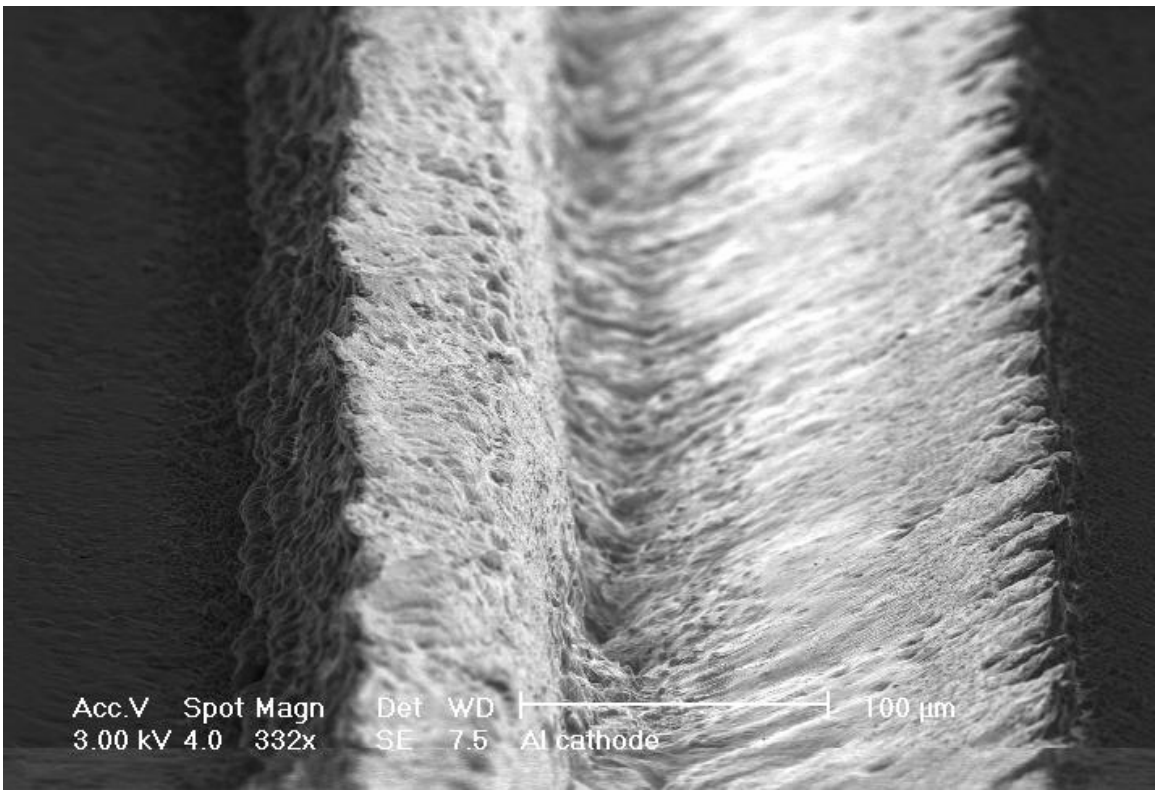

Figure 5.2 SEM image of a single trench on an ALF cathode ablated in air. Total feature width is approximately 300 μm.

If an ALF cathode is ablated in air, there is significant re-deposition of the particulate onto the cathode surface. This creates small "crater-rims" on either side of the trench, giving a total trench-to-peak height of more than 100 μm. A sample profilometer measurement is shown in Figure 5.3, where it is obvious that the two "crater-rims" are of greatly different heights.

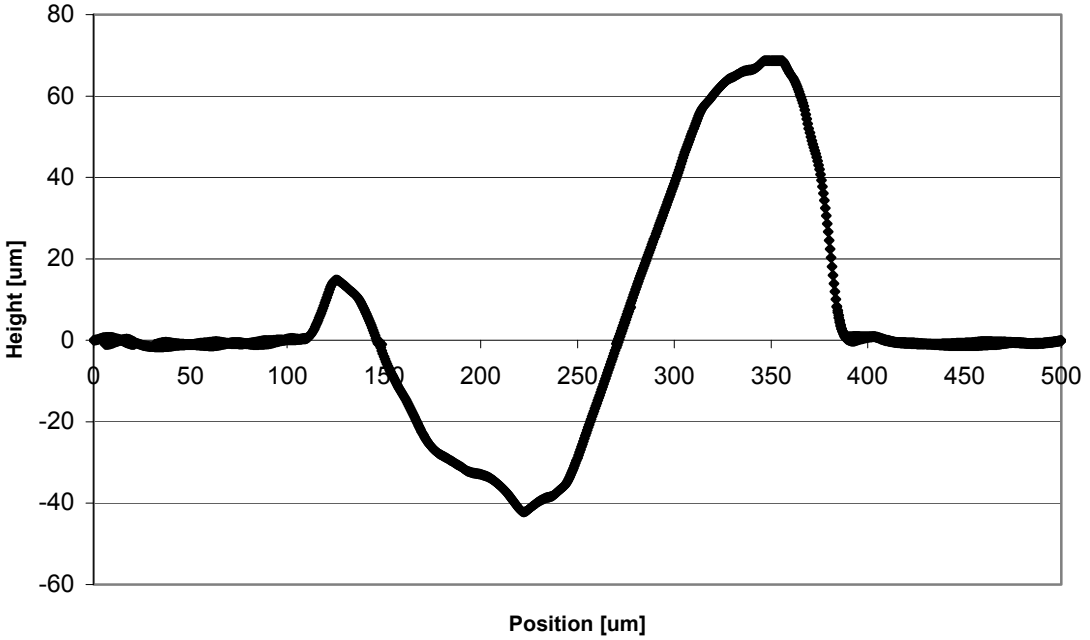

Figure 5.3 Profilometer measurement of a single trench on the surface of an ALF cathode fabricated in air.

5.2 Thin Films

5.2.1 X-ray Energy Dispersive Spectroscopy (XEDS)

X-ray Energy Dispersive Spectroscopy was performed using a UTW Si-Li Solid State X-ray Detector (with Integrated EDAX Phoenix XEDS system), coupled with a Phillips XL30 SEM, at the University of Michigan Electron Microbeam Analysis Laboratory (EMAL). The XEDS spectrum of basic Hf and HfO_2 films, shown in Figure 5.4, indicates the presence of oxygen, silicon, and hafnium; all expected quantities in the samples. Both samples were prepared using the deposition setup shown in Figure 3.1, and were deposited on silicon substrates. The first sample, shown in blue, was prepared in a 100 mTorr O_2/Ar environment, with a ratio of 20% O_2 and 80% Ar. The argon was used in this mixture to provide collisions and reduce the danger of working with a gas cylinder of pure oxygen. The second sample, shown in pink, was prepared in a $4x10^{-5}$ Torr vacuum.

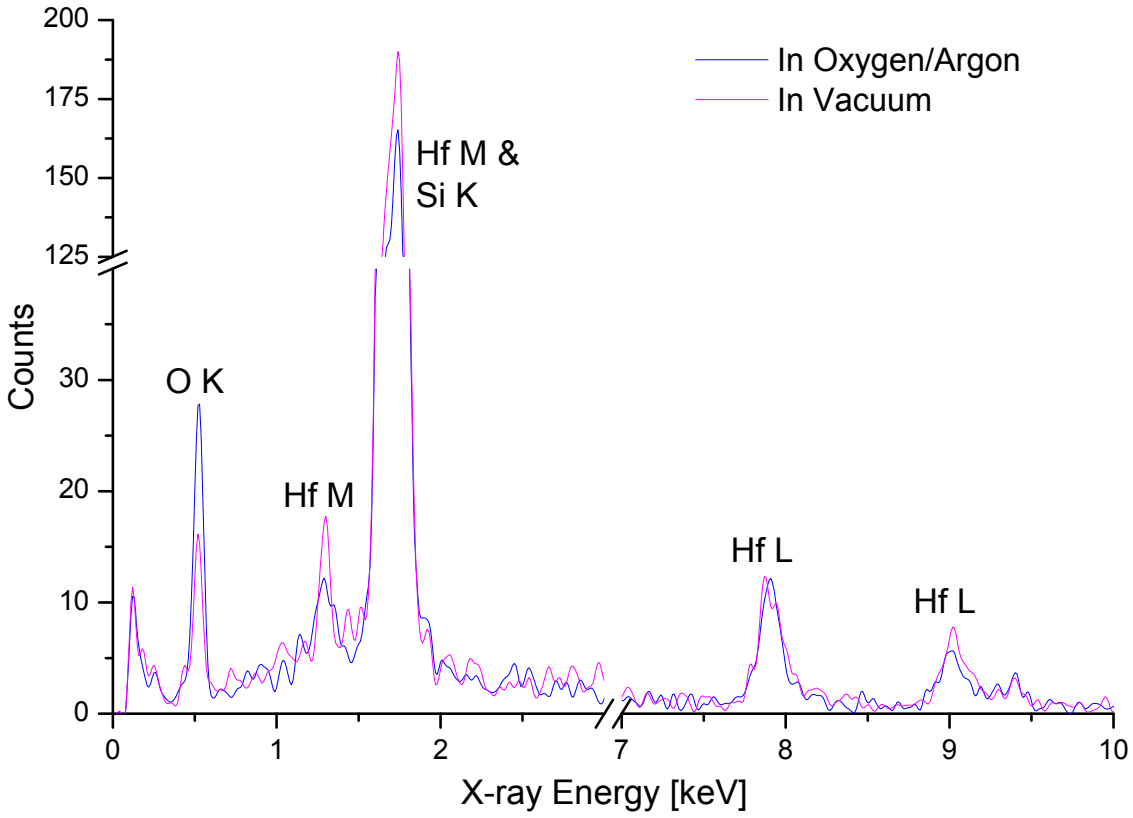

Figure 5.4 XEDS spectrum of thin films prepared in oxygen and vacuum environments.

Both samples show a strong peak at 1.74 keV, which is likely a combined peak containing the Hf lines at 1.65 & 1.7 keV, as well as the silicon peak at 1.74 keV. The hafnium signal at 1.28 keV is slightly stronger for the sample prepared in vacuum. As expected, the sample prepared in vacuum exhibits lower oxygen concentration, though we would expect the oxygen concentration to be almost zero. Many factors may contribute to the presence of oxygen in the "pure hafnium" sample. First, the hafnium target is 99.5% *metals-basis* pure. This means it may contain non-metals without lowering the reported purity. Consequently, it is quite possible that oxygen is present within the target. Secondly, the hafnium target oxidizes when exposed to air. This should only be a thin surface layer, and will be removed on the first target revolution during ablation, but oxygen will be present in the plume at this time. Additionally, the silicon substrate will form a thin oxide layer from exposure to air prior to the deposition process, and the hafnium metal (once deposited) will form a thin oxide layer from exposure to air prior to XEDS analysis. The oxygen content of these

layers may then be detected by XEDS. These oxide layers should be very thin (on the order of nanometers), compared to the ~400 nm thickness of the sample. XEDS primarily probes the material in the top 20-1000 nm of the sample [Miy02]. Lastly, a vacuum pressure of $4x10^{-5}$ Torr will still leave some oxygen within the chamber. Recoating time is estimated at 150 μs per monolayer [Cun99]. At the elevated target and substrate surface temperatures present during pulsed-laser deposition, oxidation rates will increase; making the film more susceptible to impurities present in the vacuum chamber.

5.2.2 Scanning Electron Microscopy (SEM)

A Philips XL30 Scanning Electron Microscope was used to image the surface of silicon test samples. A single dielectric island, shown in Figure 5.5, contains thousands of pieces of particulate, with a wide range of sizes. The bright spot in the center of the film is a sign of damage to the film from the 20 kV electron beam used during SEM. A close-up of one piece of particulate is shown in Figure 5.6, and it is apparent that individual particles vary widely in size, from 10's of microns to 10's of nanometers in diameter. In this image, even the particulate has particulate, with a small sphere attached to its surface. If the particulate is pure metal, these small features on top of small features could lead to a large field enhancement factor [Mil07].

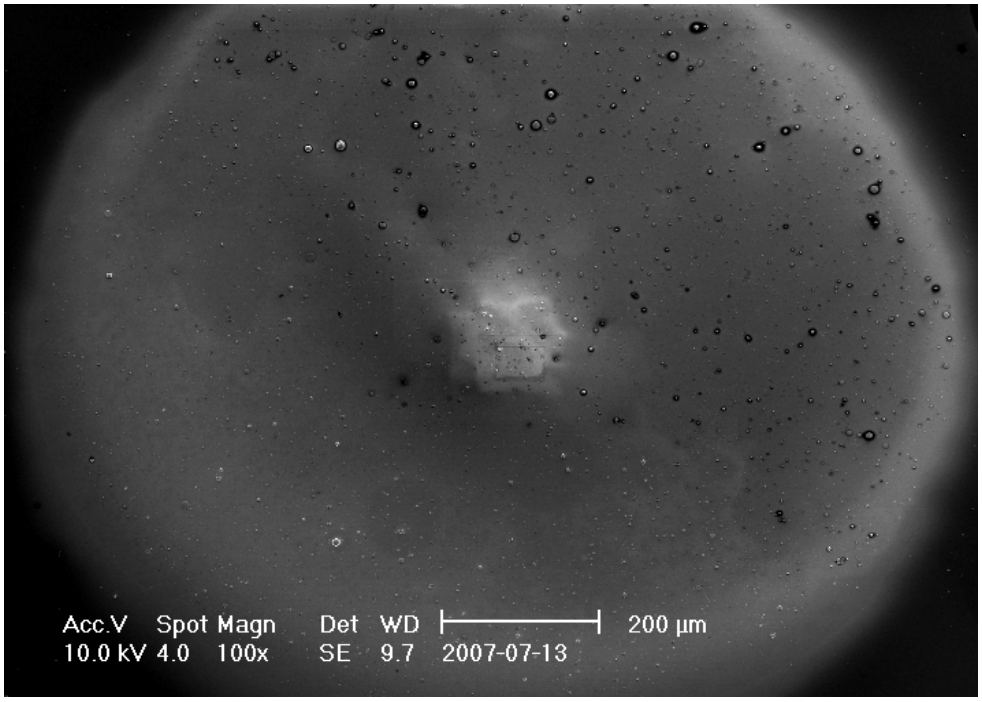

Figure 5.5 SEM image of an entire HfO_2 dielectric island, with thousands of surface particulate (light spots with dark rings surrounding them).

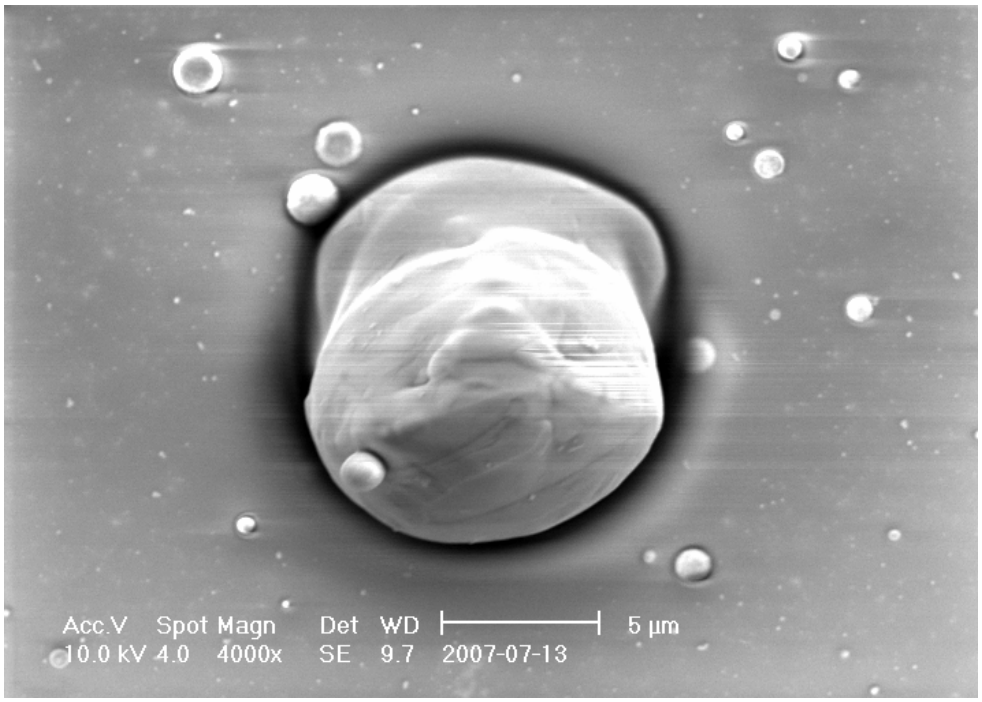

Figure 5.6 SEM image of particulate on the dielectric surface. Particulate ranges in size from 10's of microns to 10's of nanometers in diameter.

To determine the composition of the particulate, we prepared a cross-section of the hafnium oxide film and examined it using SEM.

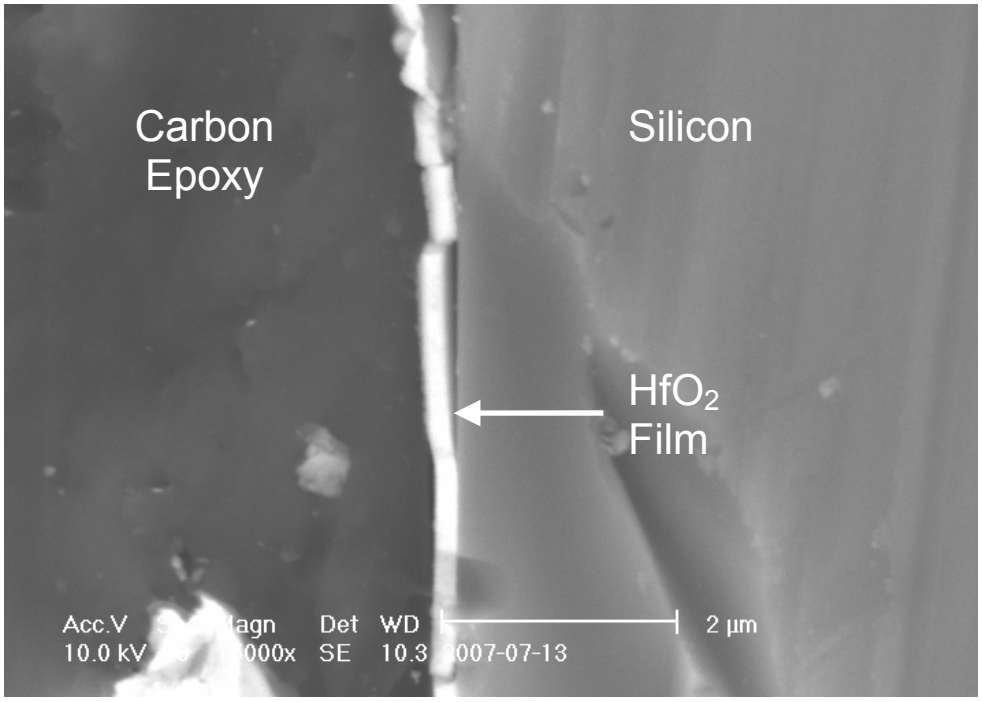

Figure 5.7 Cross-sectional SEM image of HfO_2 island on a silicon test sample. The film has separated from the silicon during sample polishing.

The white region in the center of Figure 5.7 is the HfO_2 film. In some regions, the film has separated from the silicon substrate, likely during the extensive polishing required for cross-sectional SEM. From the scale given, the film is rather thin (compared to MOJ cathode films), on the order of 100 nm. This is because the sample was cleaved through the side of a dielectric island, where the film is thinner, rather than at the peak thickness in the center.

In Figure 5.8, we see the cross-section of a piece of particulate (large bright spot) on the surface of the silicon. To the right of the particulate, we see damage (darkened regions) inside the silicon. This same "shadow" is visible in many other places along the silicon surface where particulate has deposited. This damage likely results from the thermal and kinetic energy of the particulate as it strikes the silicon surface. An alternate explanation is that the damage is somehow a result of the polishing process.

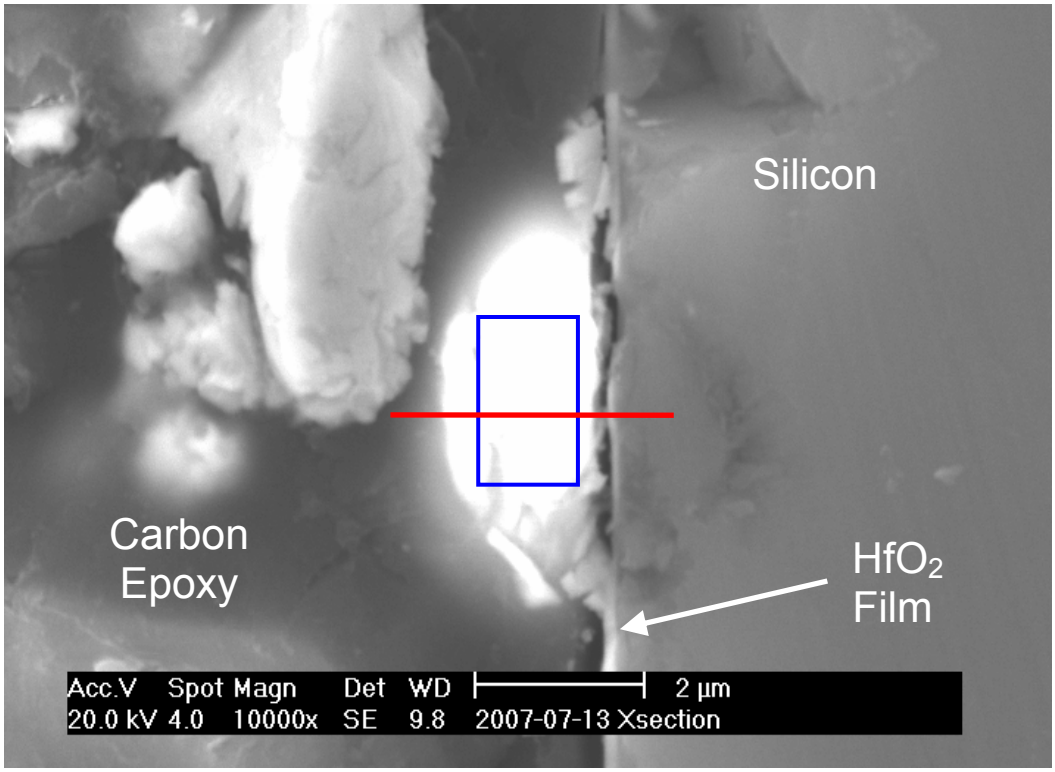

Figure 5.8 Cross-sectional SEM image of particulate on the film surface. The blue box and red line indicate the regions used for XEDS scanning in Figure 5.9 and Figure 5.10, respectively.

The blue box over the center of the particulate in Figure 5.8 indicates the region which was examined with XEDS. The results are displayed in Figure 5.9, and show that the interior of the particulate is almost entirely hafnium metal. The many hafnium transitions are marked with blue lines, with the L-shell transitions marked by dashed lines. The y-axis contains a break between 900 and 3000 counts, increasing the visibility of the smaller peaks against the intense 1.65 & 1.70 keV Hf-M lines. The data were also broken into two distinct energy regions, with the lower region containing K and M-shell transitions, and the higher region containing only Hf L-shell transitions. Peak fitting of the data give atomic percentages of 58% for hafnium, 24.5% for silicon, 10.1% for carbon, and 8% for oxygen. The carbon is from the epoxy used in preparation of the sample. Because the sample can shift slightly during XEDS data capture, the region measured may not correspond exactly to the blue box in Figure 5.7.

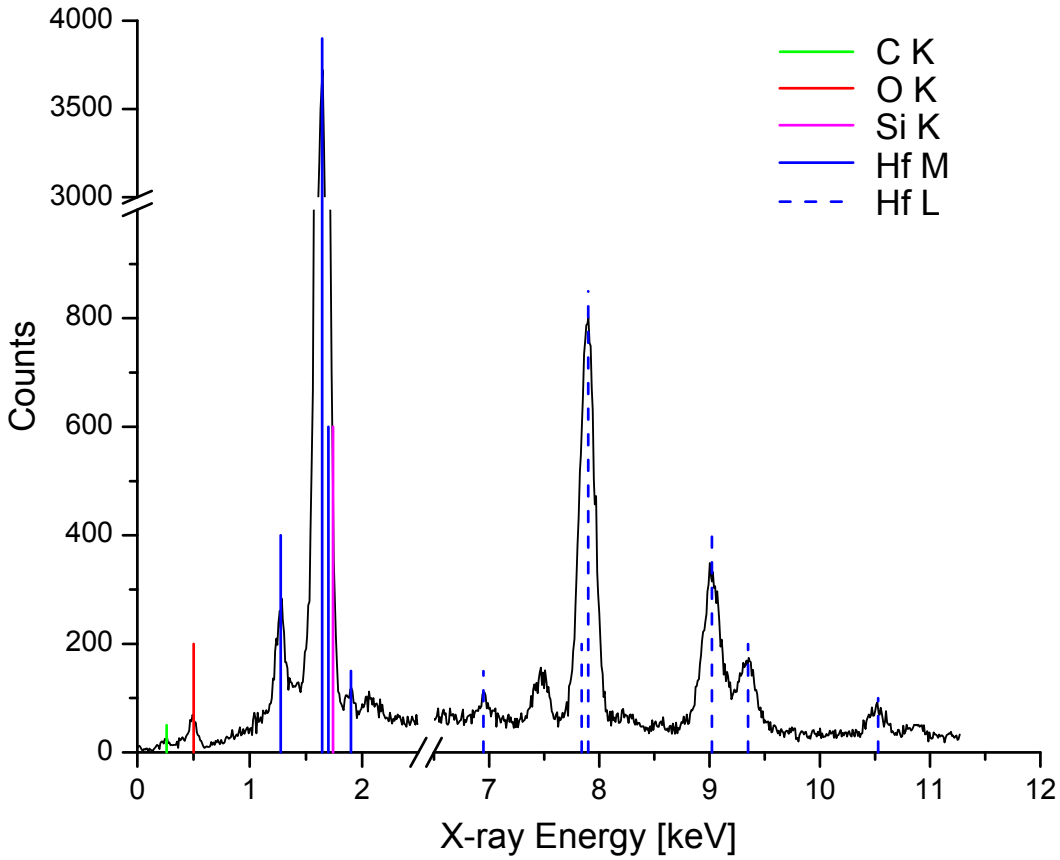

Figure 5.9 XEDS spectrum of the interior of a single piece of particulate, shows many hafnium counts and minimal oxygen signal. Note the breaks in the axes at 2.5 keV and 900 counts.

XEDS also can determine atomic fractions as a function of position along a line, the results of which are displayed in Figure 5.10. As expected, the hafnium concentration increases within the particulate, decreases around 3.2 μm, and increases again at the Si surface (where the HfO_2 film exists). Oxygen content remains roughly the same throughout the particulate, but its relative ratio to hafnium changes as the hafnium concentration changes. Near the surface of the particulate (at 0.25 μm), the oxygen to hafnium ratio is nearly 2:1, as would be expected from the chemical formula (HfO_2). This may indicate the particulate is covered with a thin oxide layer, as expected. The particulate will start as pure Hf metal, and may oxidize as it travels to the substrate, but most oxidation will occur once it has deposited. Thus, the outer surface (away from the substrate) will oxidize the most, as shown in Figure 5.10.

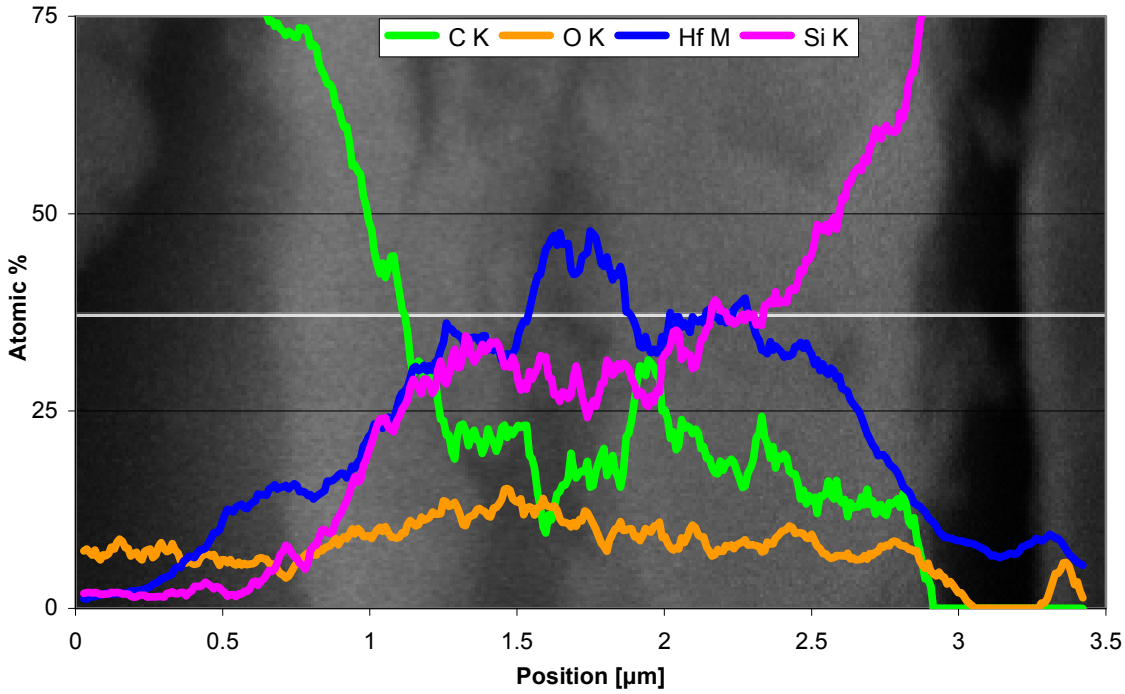

Figure 5.10 Atomic percentage as a function of position [µm] across a piece of HfO_2 particulate. The SEM image is displayed as the background, and the white line (at 37%) indicates the strip used to generate the plot.

Scanning electron microscopy detects changes in surface topology from backscattered primary electrons, photon emission, and secondary electrons [Miy02]. For our purposes, this last detection method (secondary electrons) is of particular interest, as it allows us to infer a relative secondary electron emission coefficient for hafnium oxide. By comparing the brightness of the HfO_2 and copper regions of Figure 5.11, we see that the two materials appear to have similar secondary electron emission properties. While there are many factors that contribute to SEM brightness, this at least allows us roughly estimate that the SEE coefficient of HfO_2 is less than 5. This will be important later, as we compare HfO_2 to MgO.

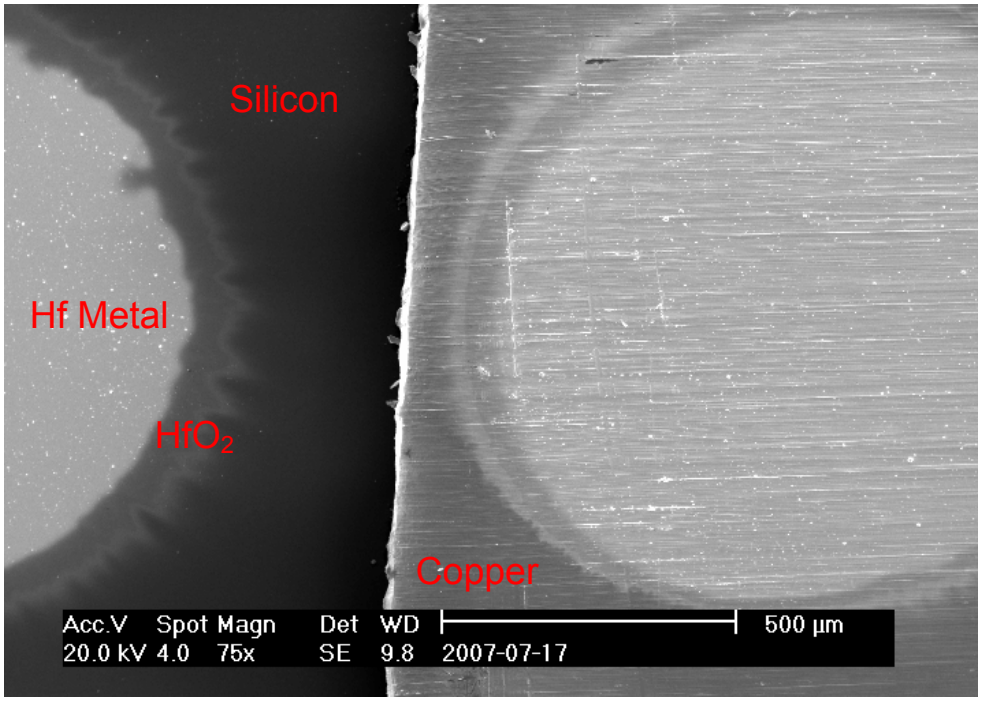

Figure 5.11 SEM image of a MIO sample, where the islands are primarily Hf metal, but the edges have oxidized. Also visible in the image is the edge of a piece of copper tape, as a reference point for secondary electron emission. From this image we can roughly estimate the SEE coefficient of HfO_2 to be close to that of copper (~2) [Bag00].

5.2.3 C-V Characteristics

An important characteristic of thin films used for semiconductor devices is the defect concentration both within the film, and at material boundaries. To measure this in our hafnium oxide films, we created a sample using a laser fluence of 31 J/cm^2, at a repetition rate of 15 Hz, for a deposition time of 12.5 min, using the setup shown in Figure 3.1. The substrate was a 3 cm x 3 cm silicon wafer, which was then coated with hundreds of small gold electrodes (3.8×10^{-4} cm^2), creating many capacitors across the film and substrate. Due to the film non-uniformity, each dot on the surface had a slightly different capacitance. Two locations on the film were measured, one corresponding to a 500 nm film thickness, and the other to a 600 nm thickness. These locations were then biased with -10 to 10 V, and the capacitance was recorded as the voltage increased, and then again as the voltage was decreased.

The voltage spacing between the forward and reverse-based cases, V_{FB}, is proportional to the density of the charges trapped in the film. In an ideal film,

there would be zero defects, and thus zero places for charge to become trapped. The resulting hysteresis curves would then lie on top of each other. As shown in Figure 5.12 and Figure 5.13, this is clearly not the case.

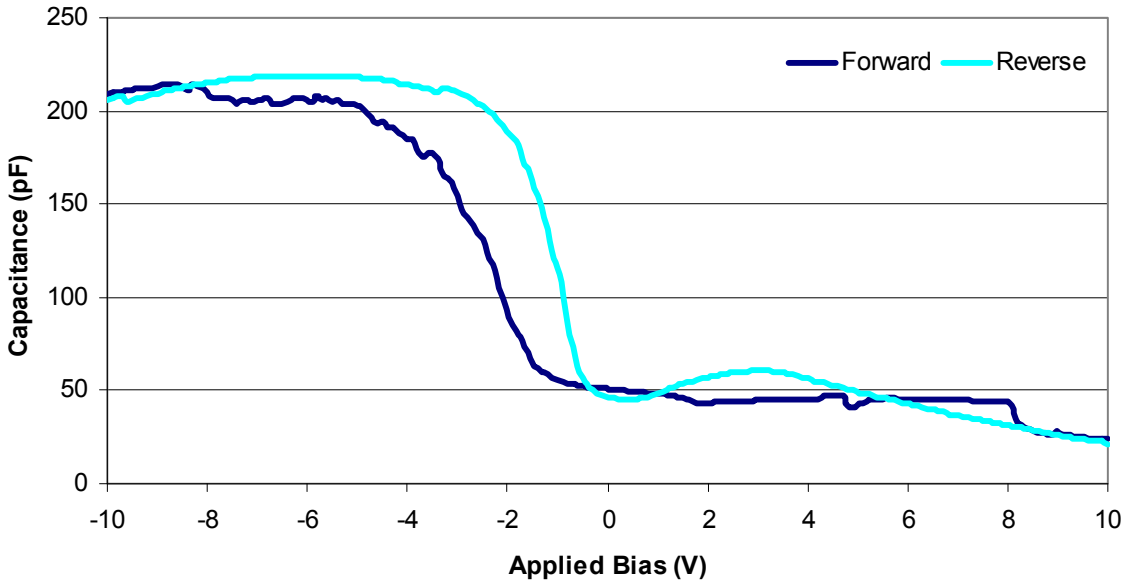

Figure 5.12 C-V measurement of 500 nm thick HfO_2 film exhibiting significant charge trapping. Measurements were made at 1 MHz.

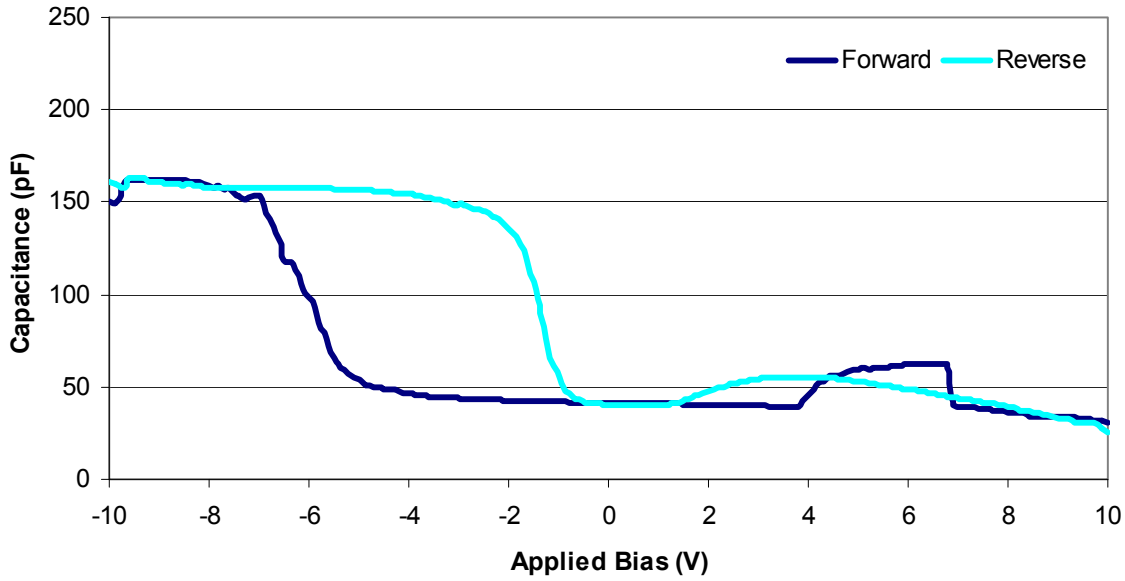

Figure 5.13 C-V measurement of 600 nm thick HfO_2 film. The increase in V_{FB} indicates increased charge trapping and defects, indicating a significant portion of the defects occur within the film. Measurements were made at 1 MHz.

The difference between these figures, however, provides some useful information. In the case of the thicker film, the charge trapping is much more severe. This indicates that significant charge trapping is occurring within the oxide, rather than just at the HfO_2-SiO_2 interface.

Creating a capacitor from the HfO_2 film is also a means of measuring the dielectric constant at frequencies of interest in the semiconductor industry. By measuring the capacitance at 1 MHz, we can determine the dielectric constant, ε_r (or κ) using the simple relation in Eq. (5.1), where *C* is the capacitance contributed by the HfO_2, *A* is the area of a gold electrode, *T* is twice the film thickness, and ε_0 is the permittivity of free space. For our "thick" sample, *C* = 36 pF, *T* = 1.2 μm, and *A* = 3.8×10^{-4} cm^2, resulting in κ = 130.

$$\kappa = \frac{C_{HfO_2} T}{\varepsilon_0 A} \tag{5.1}$$

When exposed to air at room temperature, silicon will form a native oxide layer (SiO_2) approximately 1.5 nm thick. Given a dielectric constant of 3.9 for SiO_2, this film will contribute 440 pF to the overall capacitance. As shown in Eq. (5.2), the measured capacitance is not solely due to the HfO_2 film.

$$\frac{1}{C_{measured}} = \frac{1}{C_{HfO_2}} + \frac{1}{C_{SiO_2}} \tag{5.2}$$

After correcting for this SiO_2 layer, measurements at the two film thicknesses mentioned above resulted in HfO_2 dielectric constants of 130-310. This number is considerably higher than the 20-25 typically quoted for HfO_2 thin films, perhaps partly because these measurements were made on films 100s of nanometers in thickness, while most gate oxides are 10s of nm thick. Other studies have indicated a sharp increase in dielectric constant with increasing film thickness [Nat98].

5.2.4 X-Ray Diffraction

To gain some knowledge of the crystal structure of our hafnium oxide films, we employed a technique known as X-Ray Diffraction (XRD). The

measurements were conducted on a θ/2θ Spellman/AEG FK 60-04 diffractometer in a glancing angle (3°) configuration. The only distinct peaks seen in the XRD results (Figure 5.14) were those of the silicon substrates. This indicates the film is most likely an amorphous oxide. Hafnium oxide with a cubic or monoclinic crystal structure will show many distinct peaks in the 25-40° (2θ) region [Per07].

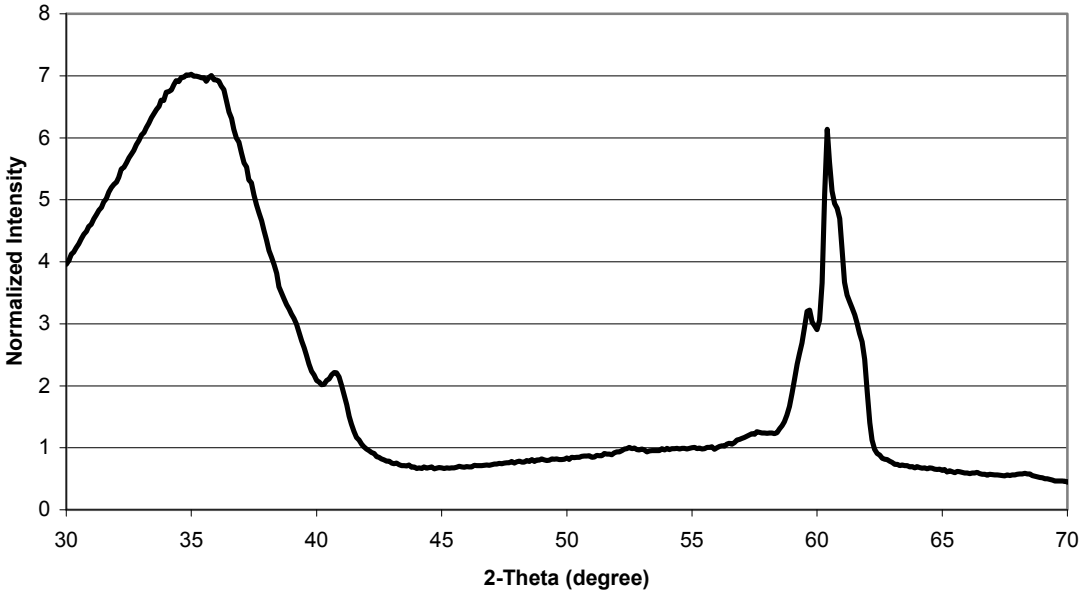

Figure 5.14 XRD spectrum from a sample of hafnium oxide. The broad peak in the 25-40° region may indicate the film is amorphous. The sharp peak at 62° corresponds to silicon.

5.3 Plasma Spectroscopy

To determine the temperature of the plasma plumes used in deposition of our thin films, we utilized plasma emission spectroscopy. The setup for this measurement is detailed in Section 4.1. As the laser strikes the surface of the hafnium and creates an ablation plume, we expect the plume to be hotter, denser, and more ionized than it will be at any later point in time. Our measurements indicate, not surprisingly, that as the plume expands, the plume temperature will decrease and the ions will recombine to form neutrals. First, in Figure 5.17, we look at a 2 μm vertical slice of the plume, 1.5 mm from the target surface, 100 ns after the laser pulse arrives, with an exposure time of 50 ns.

This is the minimum distance we are able to image, as the first 1 mm from the surface is extremely dense plasma which emits a continuum of Bremsstrahlung radiation. In terms of temporal resolution, 50 ns is the best our equipment allows. This spectrum shows many strong singly-ionized hafnium lines (Hf II - red), but only a few neutral hafnium lines (Hf I - blue). As expected, at early stages the plume is primarily ionized. It is possible that higher ionization states of hafnium exist in the plume, but their relative concentrations and lifetimes make them difficult to detect. We were not able to definitively identify any Hf III lines in any of our spectra.

Figure 5.18 shows a spectrum taken 9 mm from the target surface, 900 ns after the laser pulse arrives. At this point the plume has cooled, expanded, and many of the ions have recombined. Only a few strong Hf II lines (red) remain.

To determine plume temperatures, the data shown in Figure 5.17 and Figure 5.18 were calibrated for intensity variations as a function of wavelength. This was done using an Optronics Laboratories Model 65 Precision Current Source, and OL-245A Standard of Spectral Irradiance. The current source generates 6.5 A, creating a known filament temperature, and thus a known blackbody spectrum.

The expected intensity of each spectral line in a plasma plume is given by Eq. (5.3). However, if we plot $\frac{E_k}{k_B}$ against the natural log of $\frac{g_k A_{ki}}{I_{ki}\lambda_{ki}}$ and create a linear fit, the negative inverse slope of this line gives the temperature, in Kelvin, of the plume [Mar68, Hud65, Hol68, Sar74]. This assumes an optically thin source, an assumption that we did not verify.

$$I_{ki} = \left(\frac{hcN_o L}{4\pi Z}\right)\left(\frac{g_k A_{ki}}{\lambda_{ki}}\right)\exp\left(\frac{-E_k}{k_B T}\right) \tag{5.3}$$

This method allows the use of relative intensities, rather than requiring absolute values. It also allows us to ignore the constant, $\frac{hcN_o L}{4\pi Z}$, as this merely changes the y-intercept of the fit, and does not affect the slope. After compensating for any uneven spectrograph response, the peaks are identified, fitted in

OriginPro 7.5©, and cross-referenced with the NIST database [NIST]. Transition probabilities (g_k, A_{ki}, E_k) for hafnium were not available through NIST, so alternate sources were used [Duq86, Law07].

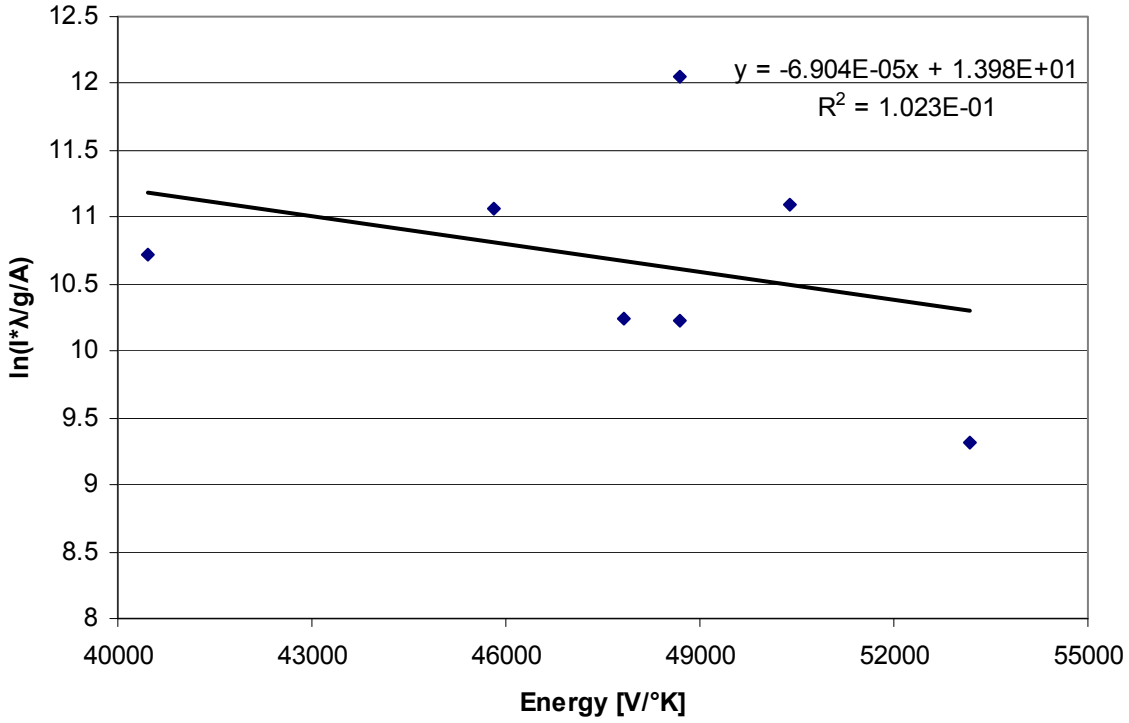

Figure 5.15 Atomic Boltzmann plot for the spectrum shown in Figure 5.17, measured 1.5 mm from target, 100 ns after laser pulse arrives. Resulting plasma temperature is ~15000 °K.

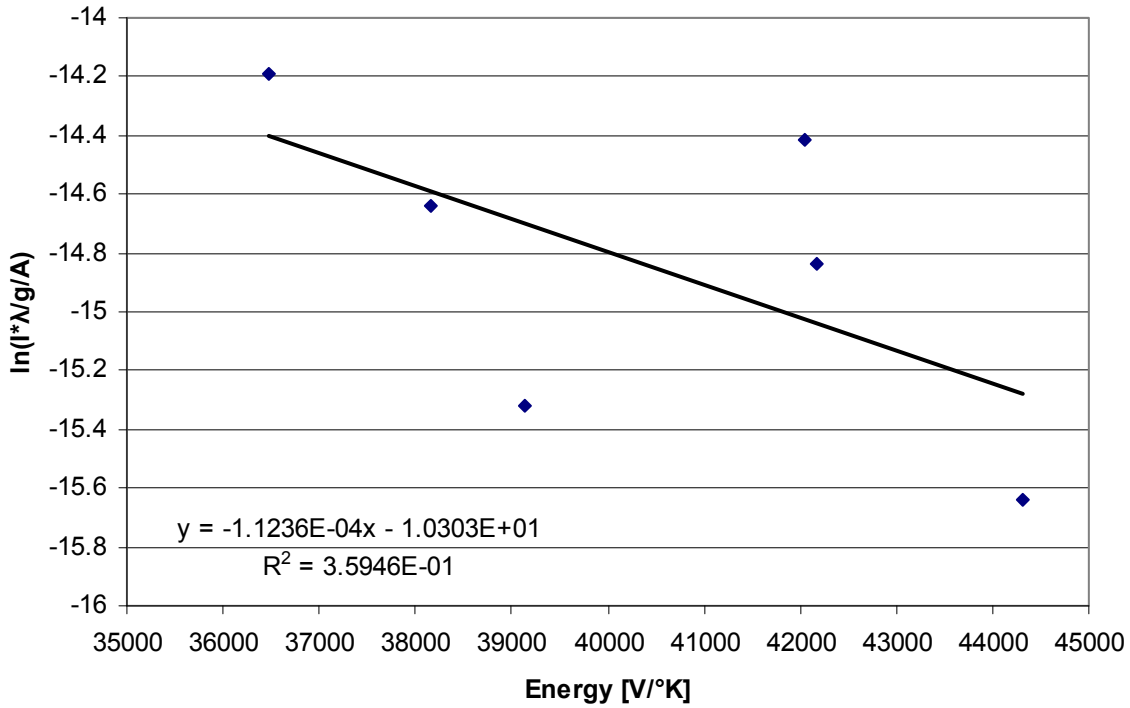

Figure 5.16 Atomic Boltzmann plot for the spectrum shown in Figure 5.18, measured 9 mm from target, 900 ns after laser pulse arrives. Resulting plasma temperature is ~9000 °K.

Using this technique, and assuming local thermal equilibrium prevails, we estimate the plasma temperature for the first case (Figure 5.17) to be ~15000 °K (2.3 ev), while the temperature in the second case (Figure 5.18) decreases to ~9000 °K (0.8 eV).

At any given distance from the target, we see the light emission from the plasma rise and fall, as the plume expands, recombines, and dissipates. In Figure 5.19, the relative intensity of each spectrum is shown as a function of time. For early times (50 ns), the plume is still expanding and most of it has not yet reached the area we are imaging. The intensity peaks at 100ns, which is why that time is analyzed in Figure 5.17. At later times, most of the plume has moved past the measurement point, and the remaining plasma has lower density.

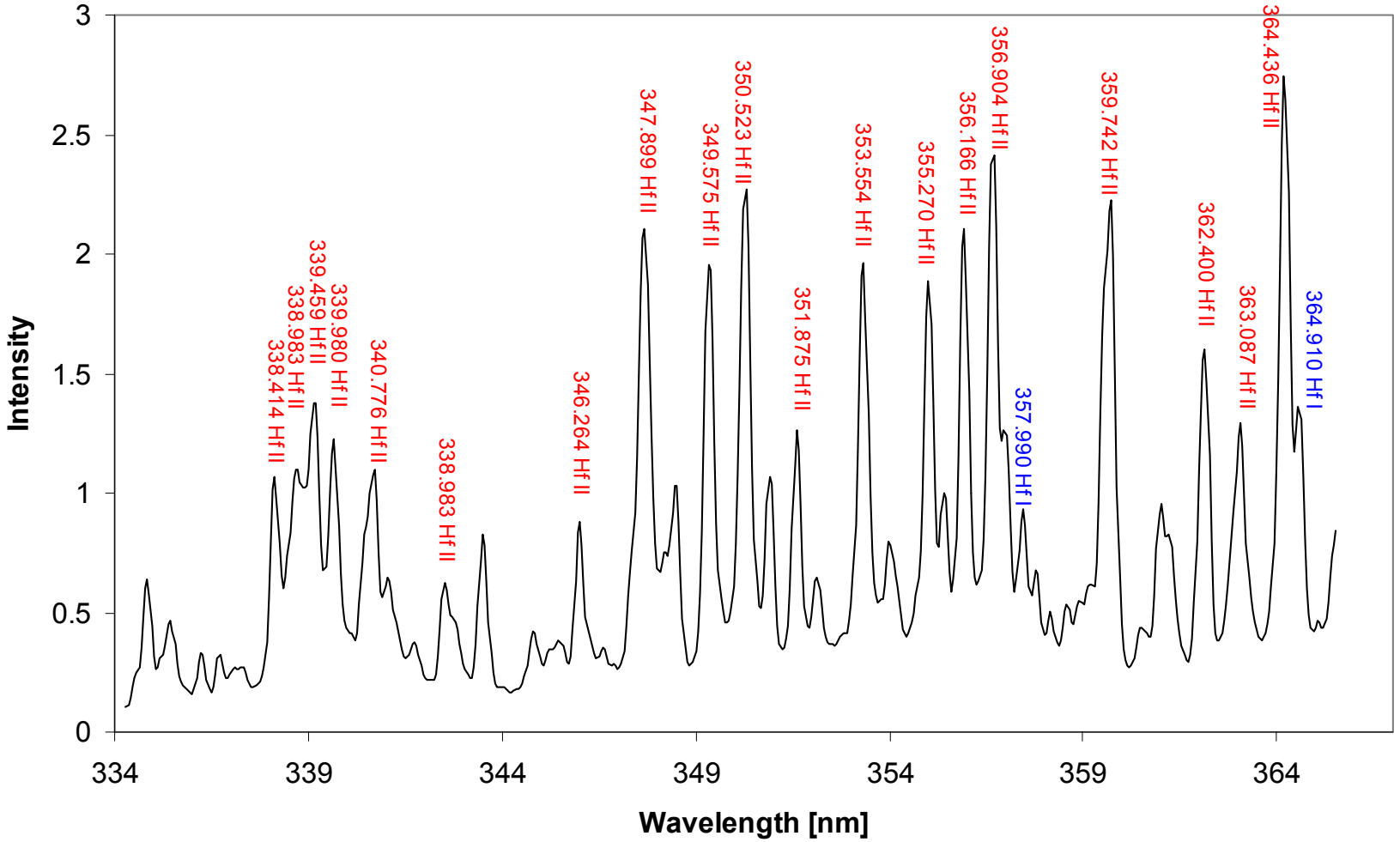

Figure 5.17 Laser Induced Breakdown Spectroscopy of hafnium plume. Measured 1.5 mm from target, 100 ns after laser pulse arrives. Blue labels indicate neutral Hf lines, while red labels indicate singly-ionzed Hf. The plume is primarily ionized hafnium.

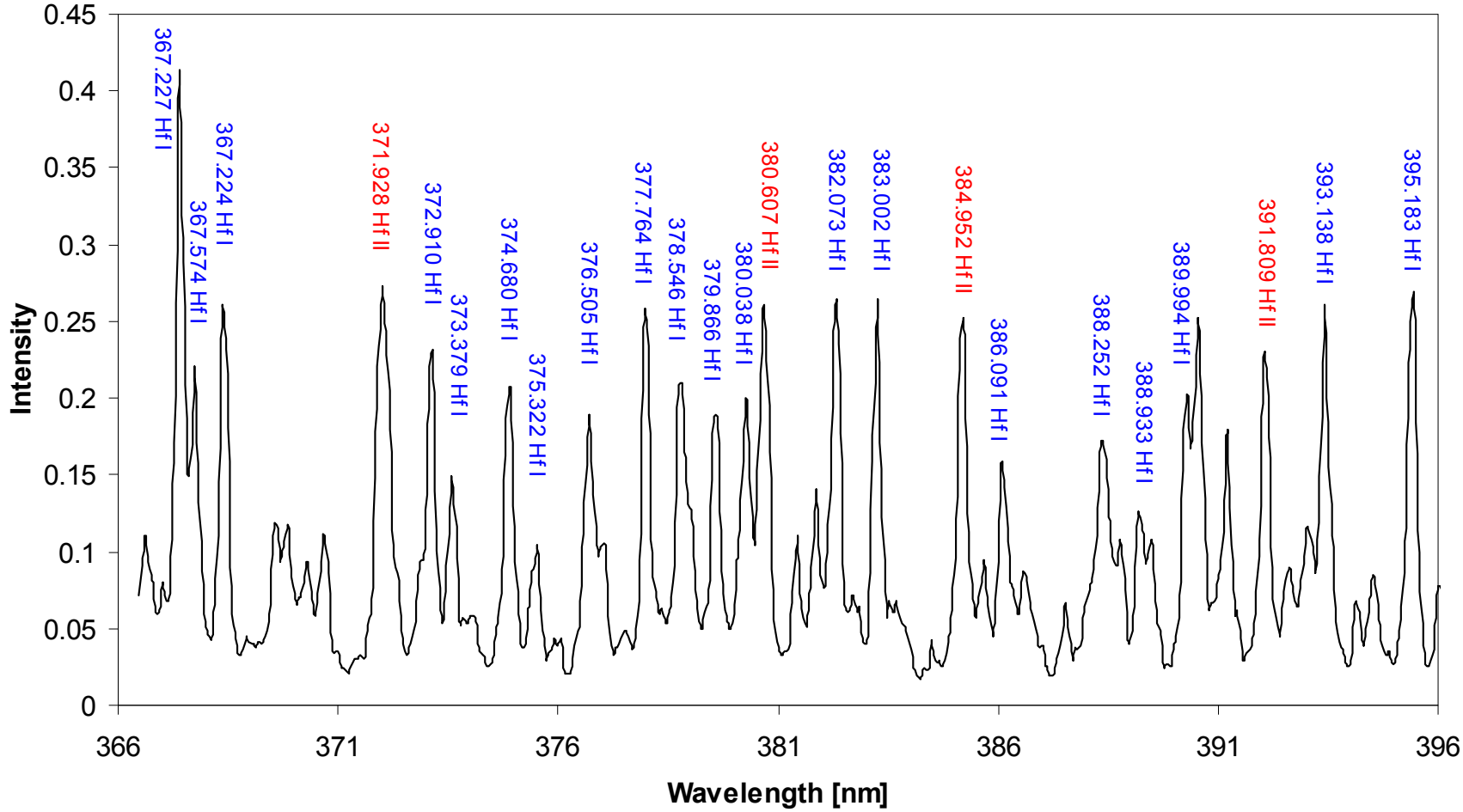

Figure 5.18 Laser Induced Breakdown Spectroscopy of hafnium plume. Measured 9 mm from target, 900 ns after laser pulse arrives. Blue labels indicate neutral Hf lines, while red labels indicate singly-ionzed Hf. The plume is primarily neutral hafnium.

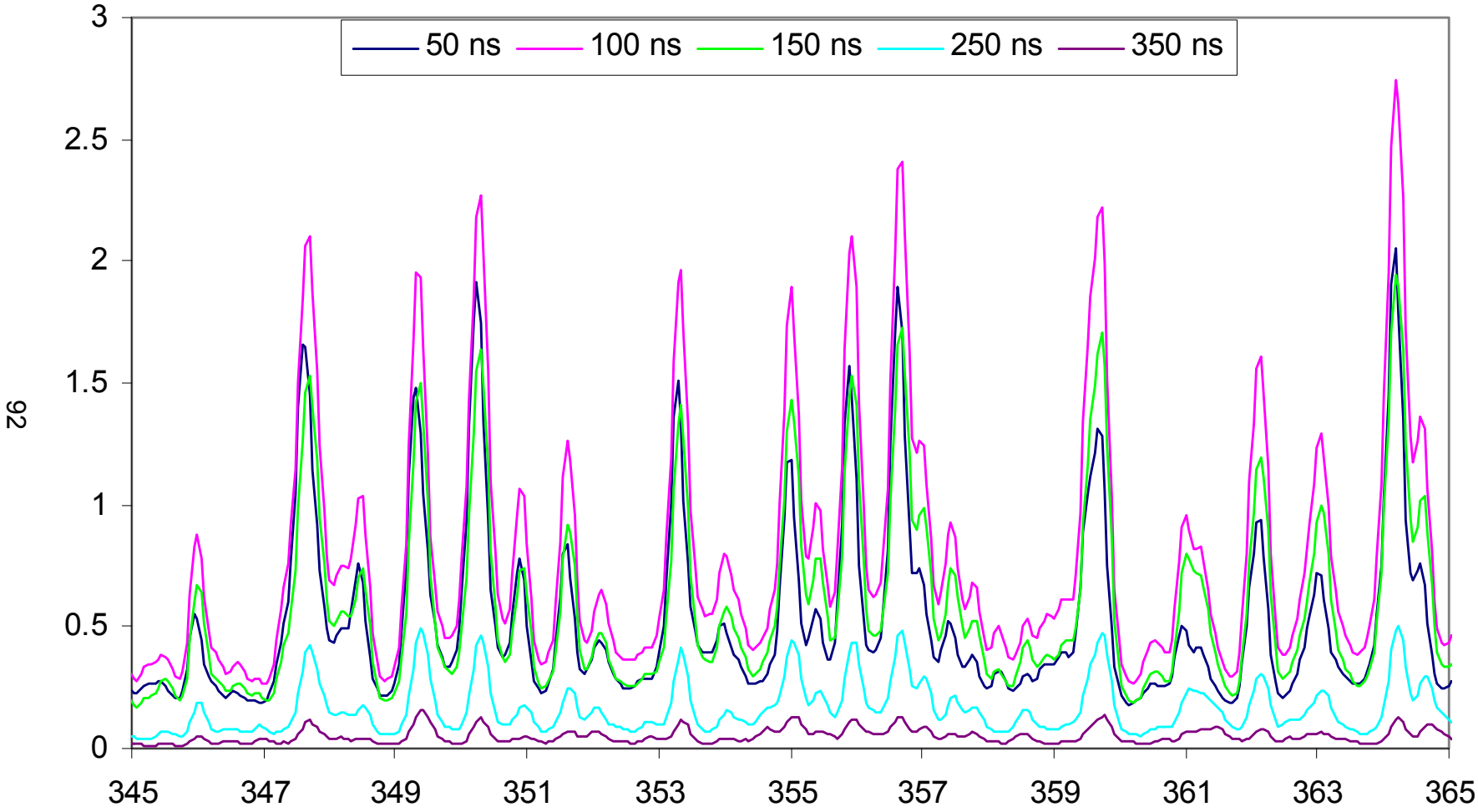

Figure 5.19 Laser Induced Breakdown Spectroscopy of hafnium plume 1.5 mm from the target, measured at various times after the laser pulse arrives. Figure 5.17 is the “100 ns” case on this plot, and was chosen for analysis because of its intensity.

CHAPTER 6
EXPERIMENTAL RESULTS OF LASER FABRICATED CATHODES ON THE UM RELATIVISTIC MAGNETRON

This chapter presents the results of 400 cathode pulses on the U of M relativistic magnetron. The cathode results are categorized into two main types: ALF cathodes and MOJ cathodes. Within these major categories, we consider a number of design variations and baseline (comparison) cathodes. For each cathode tested, the results are also divided into high (~2.82 kG) and low (~2.35 kG) magnetic field cases. We will focus primarily on the low magnetic field tests, as the high magnetic field tests do not show any additional information, and complicate the analysis. Table 6.1 lists the cathodes tested, as well as the dates and shot numbers of each testing run. For all cathode tests, the applied voltage is set to -300 kV, and the voltage, entrance current, magnet current, microwave power, and microwave frequency are recorded.

Table 6.1 Laser fabricated cathode tests on the UM/Titan relativistic magnetron.

MELBA-C Shot #'s	Cathode Type	Test Date	Fabrication Date
11027-11056	Tri-ALF	6-6-2005	6-3-2005
11057-11077	Tri-ALF	6-8-2005	"
11078-11112	Tri-ALF	6-9-2005	"
11113-11161	Tri-ALF	6-10-2005	"
12207-12227	Tri-ALF*	11-15-2007	"
11416-11442	ALF-2	11-17-2006	6-2-2005
11587-11605	Polished SS	12-12-2006	12-12-2006
12111-12127	Polished SS 2	10-25-2007	10-25-2007
12143-12162	Polished SS 3	11-1-2007	11-1-2007
11609-11623	Dielectric Coated	12-14-2006	12-13-2006
12050-12070	MIO	10-18-2007	7-9-2007
11558-11584	MOJ-01	12-11-2006	11-27-2006
12183-12206	MOJ-01	11-13-2007	"
11775-11808	MOJ-02	5-30-2007	4-12-2007
11855-11879	MOJ-03	6-6-2007	5-9-2007
12031-12049	MOJ-04	10-11-2007	7-13-2007
12071-12090	MOJ-05	10-19-2007	10-16-2007
12163-12182	MOJ-06	11-2-2007	10-29-2007

6.1 ALF Cathodes

The Ablation Line Focused (ALF) cathodes are the descendants of the Projection Ablation Lithography (PAL) cathodes previously tested at the University of Michigan [Jon05]. The two designs employ similar fabrication techniques, and both have the benefit of being entirely metal, which reduces plasma formation. This also gives them increased longevity, as our results indicate the emission characteristics do not degrade with use.

Previous MAGIC 2D simulations indicate that magnetron operation can be improved through a technique known as cathode priming. This consists of fabricating $N/2$ emission regions on the cathode surface, where N is the number of vanes (6 for our magnetron). This stimulates electron bunching into the π-mode, resulting in faster microwave startup. This concept was validated experimentally using PAL cathodes [Jon04]. Subsequent experiments have sought to improve this technique with the ALF cathode.

6.1.1 ALF-2

The “baseline” case for this test is the ALF-2 cathode. The simplest ALF pattern, ALF-2 consisted of a ring of ablation lines, 1.5 cm long, encircling the cathode. With a cathode circumference of 4 cm, this gives a total emission area of 6 cm^2. This cathode was tested at a variety of magnetic fields, ranging from 2.24 to 2.96 kGauss. Data from a typical shot are presented in Figure 6.1.

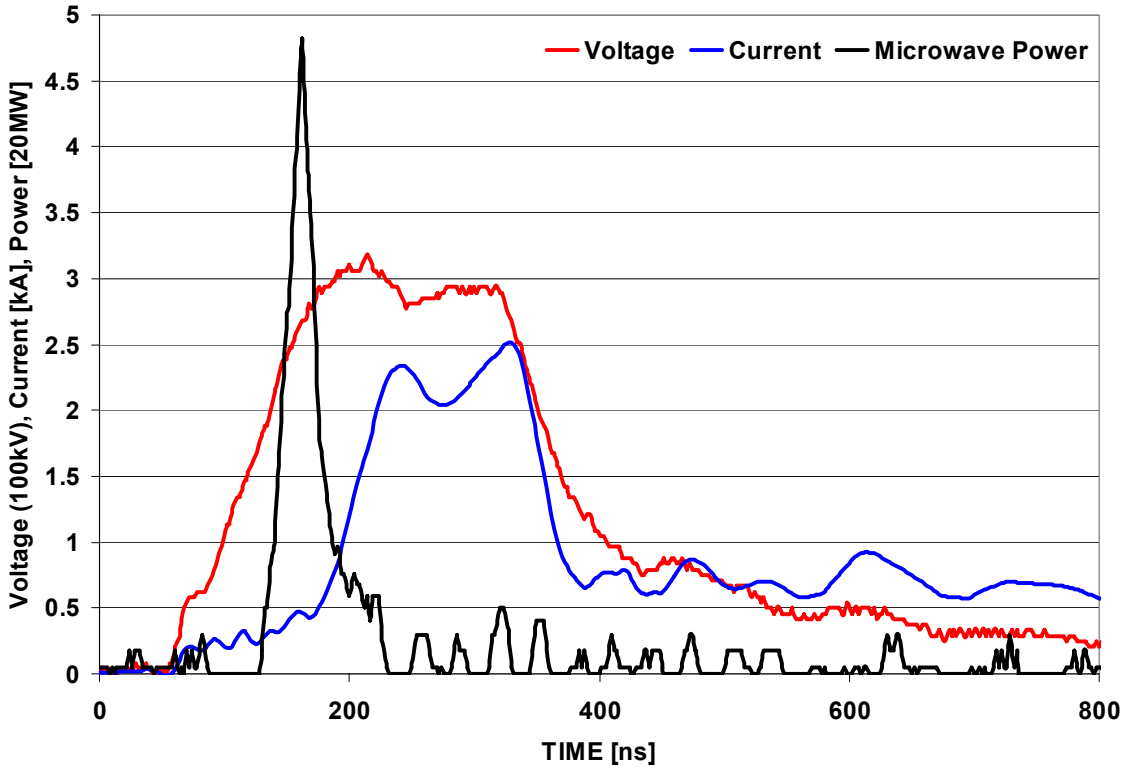

Figure 6.1 Ninth shot fired with the ALF-2 cathode, MELBA-C Shot 11424. Voltage, current, and microwave power traces are shown.

The first 200-300 ns of the voltage pulse are very consistent on a shot-to-shot basis, with similar rise times and peak voltages for all shots. After the voltage overshoot, it returns to ~-300 kV and plateaus. The length of the voltage pulse can vary widely from day-to-day or even on a per-shot basis, dependent on the breakdown of the spark-gap crowbar. If the cathode produces plasma, the length of the voltage pulse often determines the maximum current. The plasma expands away from the cathode at the plasma closure velocity, v_c, and draws increasingly large currents (according to Child-Langmuir space charge limited emission, Eqn. (1.3)) as the effective cathode radius increases. This effect is

clearly seen in Figure 6.5. By necessity, this analysis ignores the magnetic field, as C-L SCL emission is valid only in the absence of a magnetic field.

The ALF-2 cathode produced little plasma, and closure velocities were approximately 1-2 cm/μs, as shown in Figure 6.2. The closure velocity was determined from a comparison of the theoretical and experimental perveances. The purple line indicates a linear fit to the theoretical perveance. The closure velocity and effective emission length were varied to fit the theoretical perveance to the measured value. This technique is explained further in Appendix B.2.

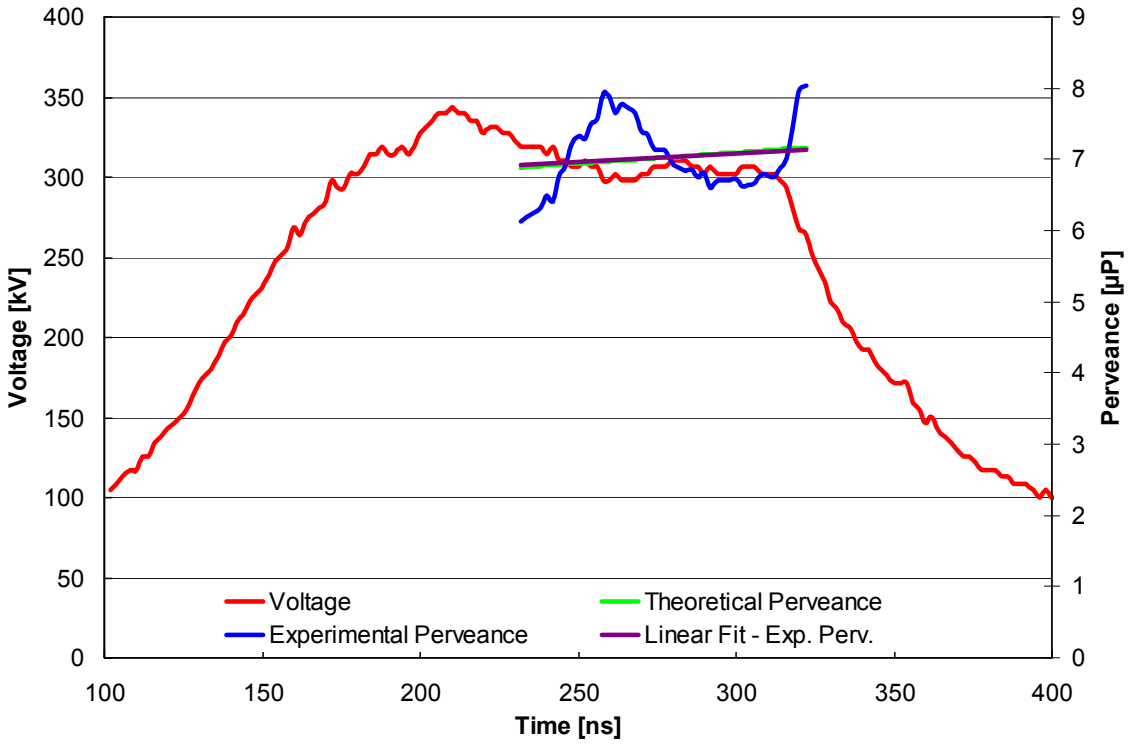

Figure 6.2 Closure velocity calculation for ALF-2, shot 11421. Closure velocity is 1.1 cm/us with an effective emission length of 1.25 cm.

Considering now the microwave signal in Figure 6.1, we see the microwave pulse begins very early in time, typically at (or before) the voltage peak and often at low current (< 0.5 kA). The microwave signal is also heterodyned with a local oscillator, typically at 1.1 GHz, to produce the signal seen in the top half of Figure 6.3. The bottom half of the figure shows the time-frequency analysis (TFA) of this signal [Wil07, Pet98], which gives the peak

microwave frequency for each shot. Dark red indicates regions of high intensity, while dark blue indicates low intensity. The frequency for this shot was 995 MHz, indicating that the magnetron was operating in the π-mode (f > 988 MHz).

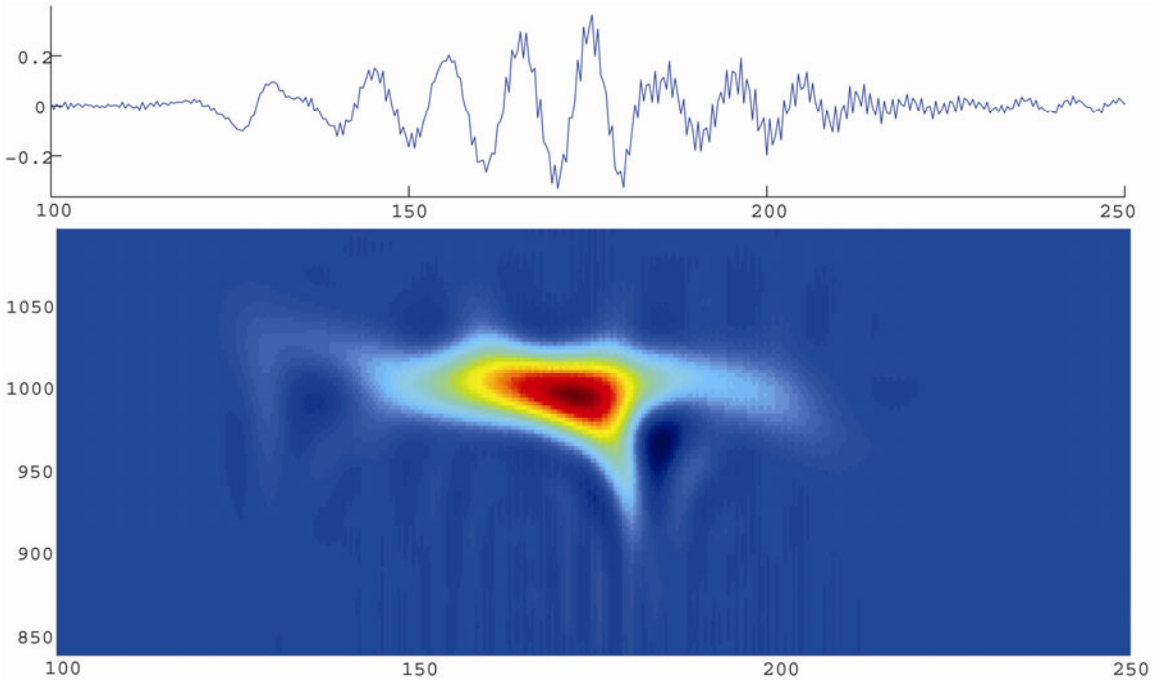

Figure 6.3 Heterodyne signal (top) and corresponding TFA (bottom) for ALF-2, shot 11424. The x-axis is Time [ns], and the y-axes are Amplitude and Microwave Frequency [MHz] for the top and bottom plots, respectively. The highest intensity regions are shown in dark red, lowest intensity is dark blue.

6.1.2 Tri-ALF Cathode

The Tri-ALF cathode was designed for cathode priming, with three patterned emission regions. Each region is 2 cm^2, for a total of 6 cm^2, equivalent to the area of the ALF-2 cathode. Between the emission regions, the cathode was milled out and sprayed with carbon paint, in an attempt to suppress electron emission in those regions. Over 150 shots were taken on this cathode, at a similar range of magnetic fields, 2.24 to 2.90 kGauss. For better comparison with ALF-2 data, the shots used for analysis correspond as closely as possible to the magnetic fields used for ALF-2. Data from a typical shot are presented in Figure 6.4.

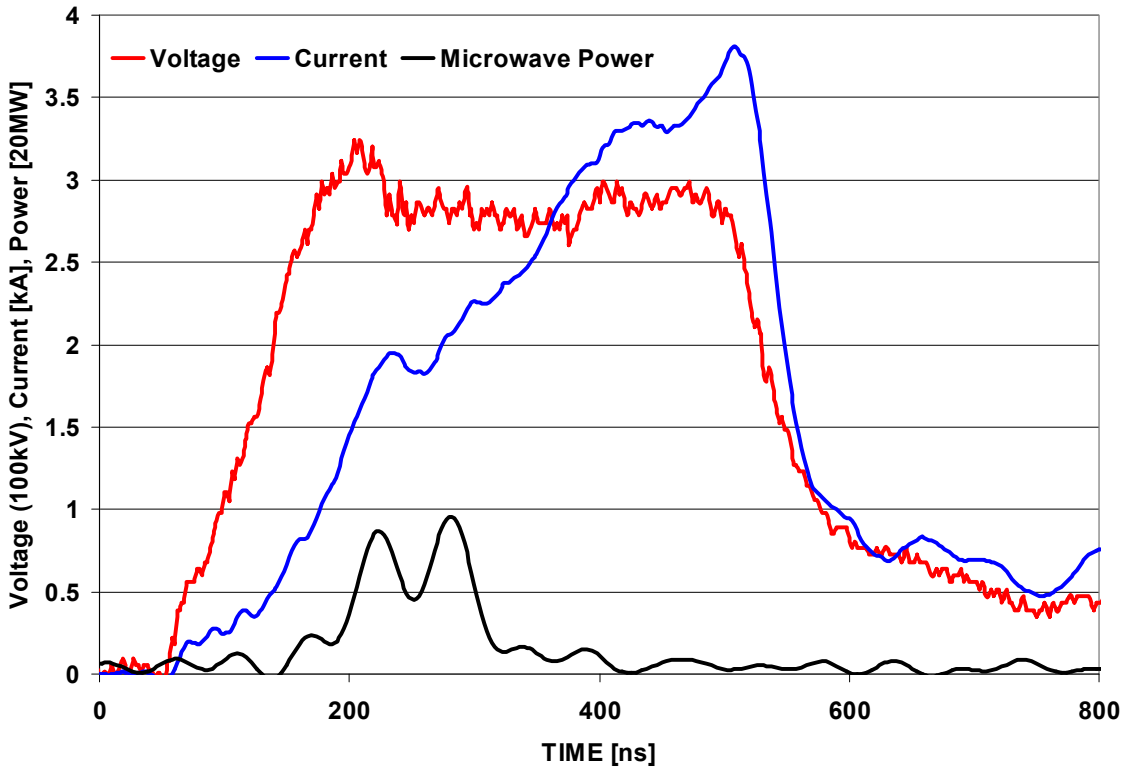

Figure 6.4 The 39th shot fired with the Tri-ALF cathode, MELBA-C shot 11065. Voltage, current, and single waveguide microwave power traces are shown. The microwave power trace is shown after 20 MHz filtering.

From this voltage and current trace, we clearly see the plasma-closure effects described previously. The voltage pulse is ~400 ns long, and very consistent. The current, however, ramps up at a relatively constant rate. In Figure 6.5, we determine the closure velocity for this shot to be 4.3 cm/μs, with an effective emission length of 2.75 cm. The higher closure velocities for the Tri-ALF series, compared to ALF-2, likely results from sharp corners and removal of the carbon paint. Back-bombardment of the cathode surface will cause some ablation of the carbon, potentially creating plasma at the cathode surface. Examination of the cathode after ~150 shots revealed some regions where the carbon paint had been completely removed.

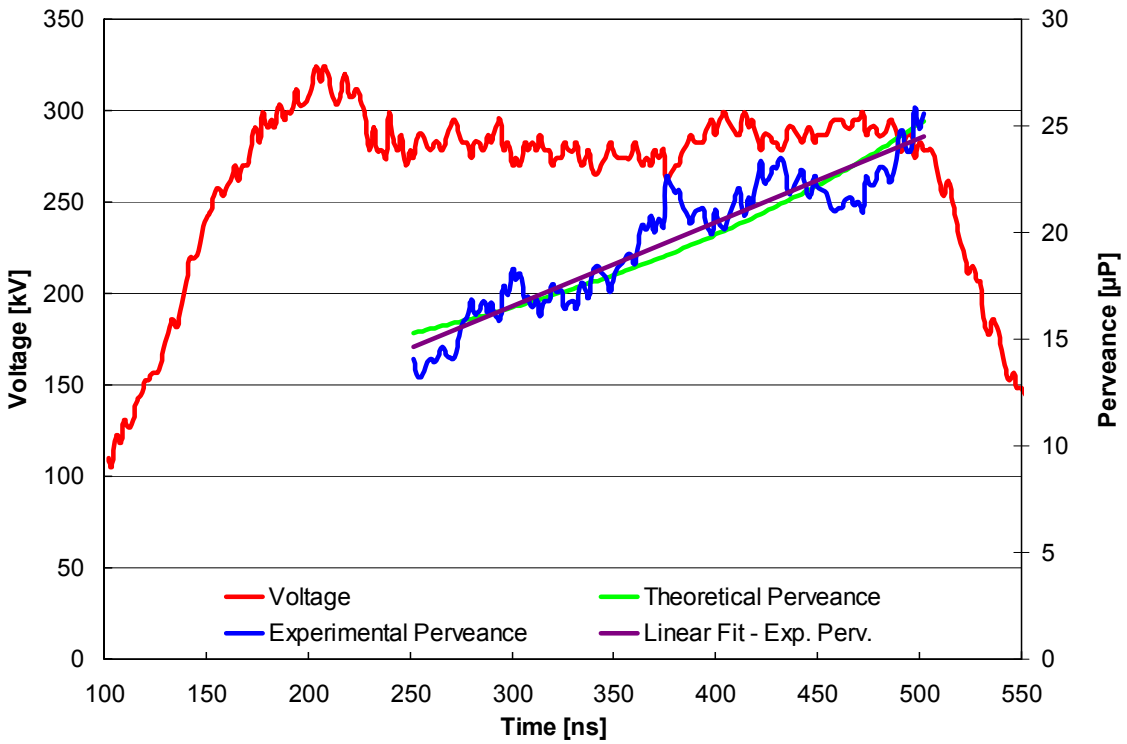

Figure 6.5 Closure velocity calculation for Tri-ALF, shot 11065. Closure velocity of 3.8 cm/us with an effective emission length of 2.8 cm.

6.1.3 Tri-ALF* Cathode

The original tests of the Tri-ALF cathode were conducted before the addition of power couplers on all three microwave extraction waveguides, so microwave power data were only available from a single waveguide (MPOW). To improve the quality of comparisons of microwave characteristics, the Tri-ALF cathode was re-tested more than two years after the original run. Data from this run are denoted Tri-ALF*, and include a microwave coupler in all three extraction waveguides. The long delay between tests is less than ideal, as the magnetron's performance may have changed, but it should still result in a more valid comparison of microwave performance. The magnetic fields used to test this cathode are consistent with those used in testing ALF-2.

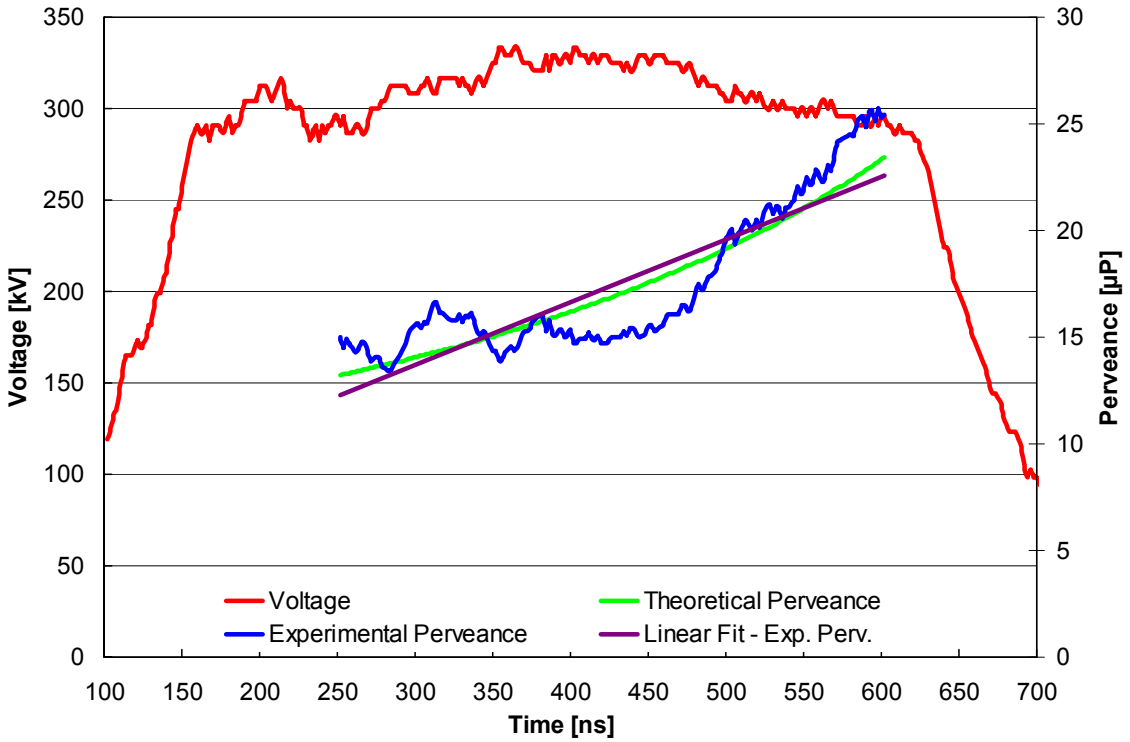

Figure 6.6 Closure velocity calculation for Tri-ALF*, shot 12213. Closure velocity of 2.9 cm/us with an effective emission length of 2.35 cm.

6.1.4 ALF Cathode Analysis

In this section we will compare the results of the ALF cathodes, evaluating if the design objectives were met. The section concludes with a summary of all relevant parameters in Table 6.2. First, we consider the microwave performance of the cathodes. When using the ALF-2 cathode, the magnetron operated in the π-mode (f > 980 MHz) for 68% of the shots, compared to only 17% for the Tri-ALF and Tri-ALF* cathodes, as shown in Figure 6.7. By this measurement, the Tri-ALF patterning is not successful in priming the magnetron into the desired mode.

One other interesting result in Figure 6.7 is the fact that Tri-ALF* obeys the Buneman-Hartree resonance condition (Appendix B.1), while the other two cathodes do not. All three shots taken above 3 kGauss (two shots share the same frequency and lie on top of each other in the figure) produced π-mode oscillation, while all other shots did not. Three data points are hardly conclusive, but an interesting result nonetheless. It is also a possibility that the milled out

sections of cathode are shifting the π-mode of the magnetron when a Tri-ALF cathode is installed. While this information might be obtainable from a cold-test of the cavity, the plasma production at the cathode surface may alter the π-mode frequency beyond what a cold-test can predict. Phase measurements during each shot (a capability currently being added) would be the best way to accurately determine when a cathode is operating in the π-mode.

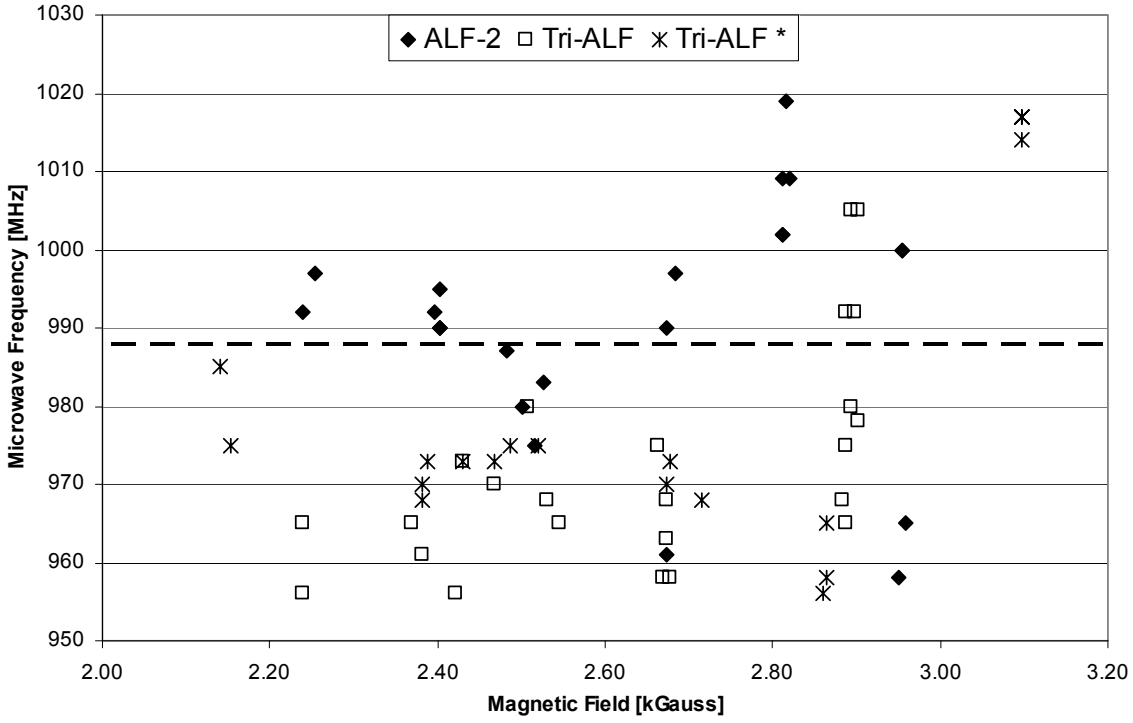

Figure 6.7 Microwave frequency as a function of magnetic field for ALF-2 ,Tri-ALF and Tri-ALF*. The dashed line indicates the lower frequency threshold for π-mode operation. ALF-2 shows a higher percentage of π-mode shots.

Another intended priming effect of the Tri-ALF cathode was a reduction in microwave oscillation start-up time. All times in this thesis are measured relative to V = -100 kV. This point is defined as t =100 ns. There are several reasons this method was chosen. First, the voltage pulse often has a small "bump" that occurs before the voltage begins to rise, choosing a lower threshold value would cause all time measurements to fluctuate with this bump. Second, the voltage rise-time is consistent on a shot-to-shot basis, and overlays of many shots show a consistent pulse shape when anchored at this voltage threshold (Figure 6.12).

Lastly, defining this point as t = 100 ns allows the entire pulse to occur in positive time.

Consequently, we measure the time to current startup, time to microwave startup, and time to peak microwave power. Current startup is defined as the time at which the current rises above 0.3 kA and microwave startup is defined as the time at which the total microwave signal rises above 6 MW. The average values for these quantities are shown in Figure 6.8. Based on the first run, the Tri-ALF cathode was not successful in reducing the startup time of the microwave pulse, or improving the microwave performance of the magnetron. The microwave performance of the cathode greatly improved in the second run, with the Tri-ALF* cathode producing slightly faster microwave startup, and roughly equivalent time to peak microwave power, when compared to ALF-2. Additionally, the peak power of ALF-2 was higher, at 84 ± 24 MW, compared to 27 ± 9 MW for Tri-ALF (this total power is estimated by tripling the single waveguide measurement) and 72 ± 12 MW for Tri-ALF*. The corresponding pulse width was 128 ± 18 ns for ALF-2, compared to only 66 ± 60 ns for Tri-ALF and 102 ± 19 ns for Tri-ALF*.

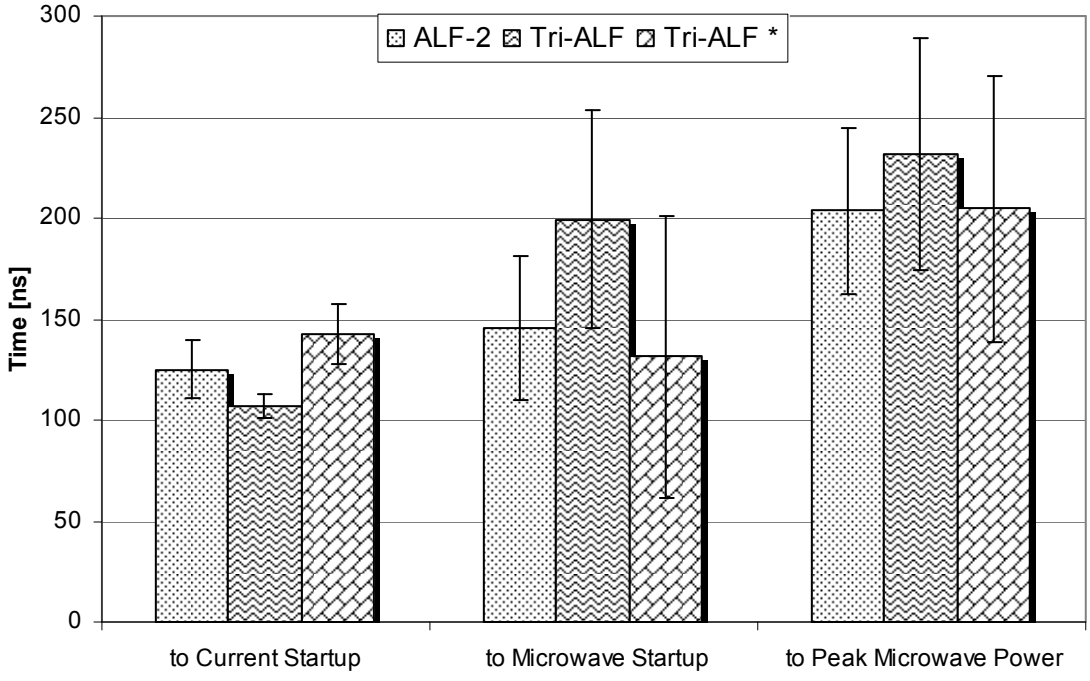

Figure 6.8 Average startup times for ALF cathodes. The Tri-ALF cathode shows an increase in microwave startup time.

The Tri-ALF cathode did show a slight improvement, however, in current startup time. This is not surprising, considering the current results presented in Figure 6.9. The Tri-ALF cathode emitted larger average currents than the ALF-2 cathode at all points of comparison, though no results are statistically significant as there was significant variance in the data. This current performance did not persist for the Tri-ALF* testing, with the current decreasing at most points of measurement. This is partly due to the faster microwave startup. The microwave pulse typically starts during the initial current ramp up. Consequently, earlier microwave startup will result in lower startup current for similar current pulses.

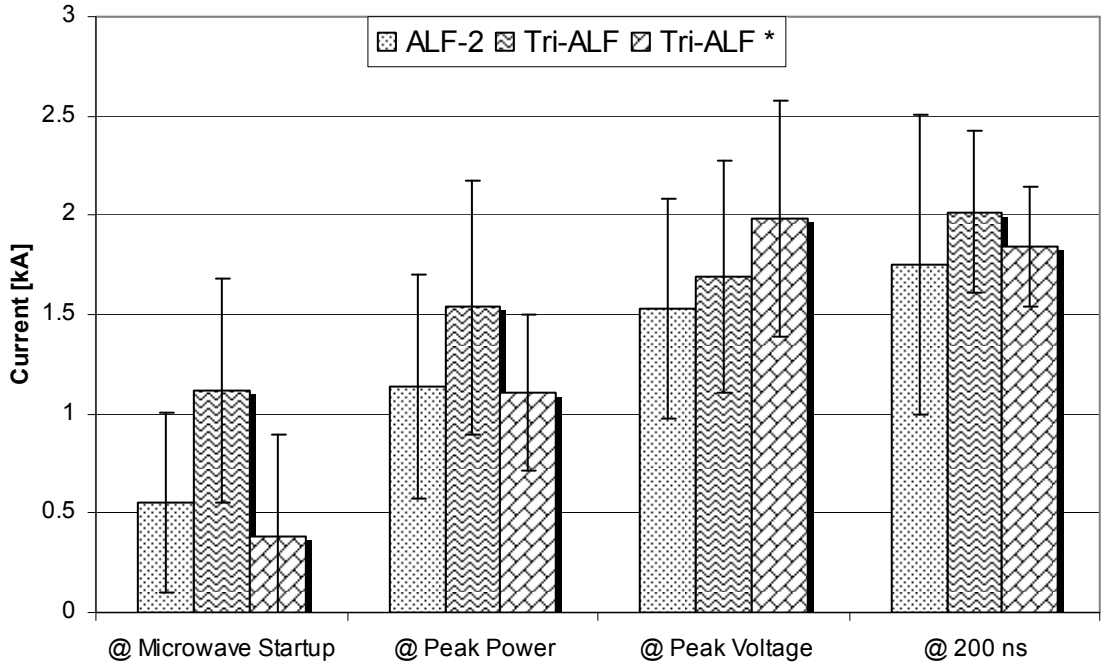

Figure 6.9 Average current results for ALF cathodes. The Tri-ALF cathode emitted higher average currents at all four measurement times.

Given the increased plasma closure velocities, inconsistent microwave priming, and higher emission currents of the Tri-ALF cathode, it is likely the cathode was producing plasma in the milled-out regions. The carbon paint intended to suppress emission was instead fueling plasma creation. Inspection of the cathode after 150+ shots revealed much of the carbon paint had been removed during testing, further reinforcing this hypothesis. The results of Tri-

ALF* also support this, as the carbon paint was not re-applied before this run. The plasma production increases the effective radius of the cathode and, consequently, the space-charge limited current increases. The creation of a plasma cathode also masks the priming effect of three-region patterning, as the magnetron sees a plasma column, rather than three distinct emission regions.

Table 6.2 Summary of average parameters for ALF cathodes.

	ALF-2	Tri-ALF	Tri-ALF*
Time to Microwave Startup [ns]	143 ± 37	198 ± 53	131 ± 70
Time to Peak Power [ns]	202 ± 41	230 ± 57	205 ± 66
Pulse Width [ns]	128 ± 18	22 ± 20	102 ± 19
Peak (Total) Microwave Power [MW]	84 ± 24	27 ± 9	72 ± 12
Microwave Frequency [MHz]	991 ± 16	973 ± 14	978 ± 19
Current at Peak Voltage [kA]	1.55 ± 0.56	1.71 ± 0.58	1.98 ± 0.59
Current at Microwave Startup [kA]	0.53 ± 0.46	1.11 ± 0.56	0.38 ± 0.52
Current at Peak Power [kA]	1.11 ± 0.56	1.52 ± 0.63	1.11 ± 0.39
Current at 200 ns [kA]	1.74 ± 0.73	2.01 ± 0.40	1.85 ± 0.30
Magnetic Field at Microwave Startup [kG]	2.64 ± 0.24	2.65 ± 0.23	2.63 ± 0.30
Voltage at Microwave Startup [kV]	202 ± 77	292 ± 27	149 ± 93

As mentioned at the beginning of this section, the ALF cathodes do not show any decrease in electron emission as a function of shot number. Figure 6.10 shows there is virtually no correlation between current and shot number. These results should not be extrapolated to the thousands of shots necessary in a repetitively pulsed system, but for our testing in a single-shot (<< 1 Hz) environment, they indicate we can expect the cathode to perform similarly at the beginning and end of an experimental run. The slight increase in current may indicate some amount of cathode conditioning takes place, but the correlation is extremely weak (R^2 values of 0.4 for ALF-2 and 0.05 for Tri-ALF) and the plot does not account for any trends due to magnetic field.

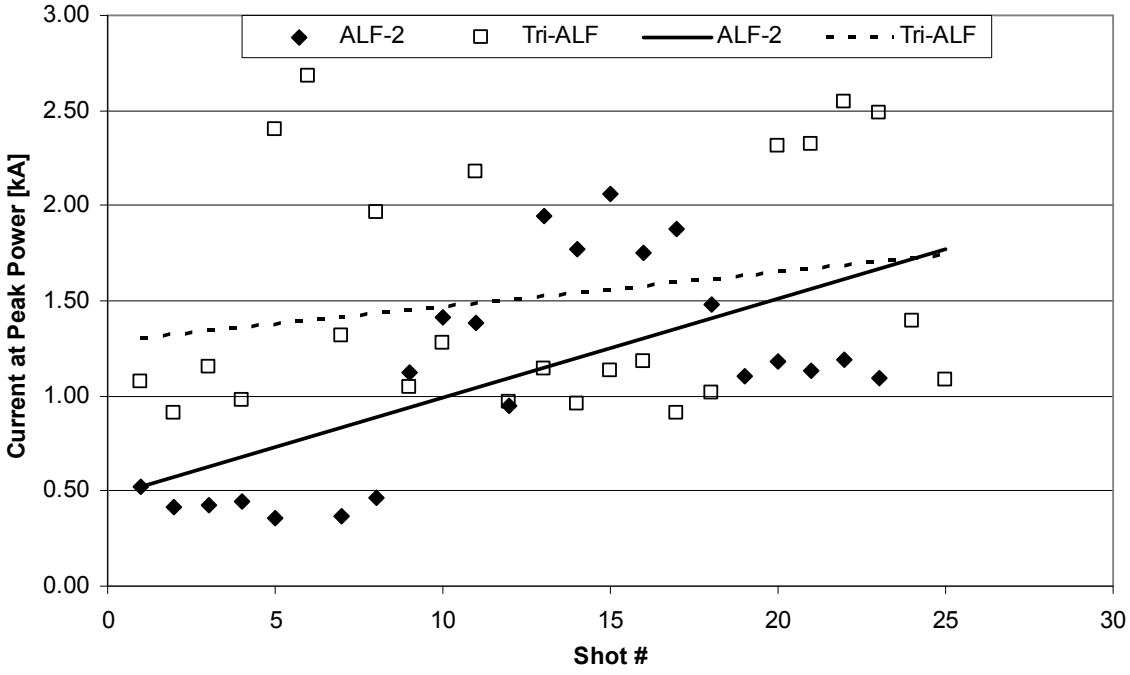

Figure 6.10 ALF cathode current measured at peak microwave power, as a function of shot number. The solid and dashed lines are linear trendlines for the ALF-2 and Tri-ALF cathodes, respectively. Cathodes show a slight increase in emission over the small number of shots tested.

ALF cathode tests at the University of Wisconsin have reported a sharp decrease in emission after many thousands of shots and/or long term exposure to ambient air [Sch07]. Possible explanations include oxidation of the cathode surface and deterioration/removal of triple points and field-enhancing emission sites on the cathode.

6.2 MOJ Cathodes

Six metal oxide junction cathodes were tested in a series of seven cathode runs over a span of nearly a year. In addition to being a challenging environment for cathode studies, MELBA-C and the relativistic magnetron do not always maintain consistent performance over such extended timescales; MELBA-C is typically “rebuilt” on a yearly basis. To establish points of comparison, four baseline cathodes were tested in a series of five runs spanning a similar year-long timeframe. In this section we will discuss the baseline cathode and the MOJ cathode results, concluding with a performance analysis.

6.2.1 Baseline Cathodes

As mentioned in Chapter 3, a polished stainless steel (PSS) rod is the starting point for all MOJ cathode fabrication. As such, it is a logical baseline. With an applied voltage of -300 kV, a bare metal cathode with no patterning will still emit some current. With this in mind, we tested PSS1 immediately following the first run of MOJ-01. PSS1 was later used to fabricate the dielectric coated (DiCoat) cathode. Nearly a year later, we sought to re-establish our baseline, and ensure nothing in the magnetron operation or diagnostics had changed. Though PSS1 had been coated with dielectric, we sanded away the dielectric coating and returned the cathode to its original 2500-grit surface finish. This cathode is denoted PSS2, and produced currents far below its original performance, as shown in Figure 6.11.

While the data in Figure 6.11 appear to indicate that the magnetron operation or diagnostics had changed, it is also possible coating the cathode with dielectric and then re-finishing the surface had an adverse affect on its current emission performance. Another possibility is that the additional sanding increased the smoothness of the surface (compared to PSS1). To test this, PSS3 was created from a new piece of stainless steel tubing, and was only sanded to a 1500-grit finish. At best, this cathode surface would still be rougher than the original PSS1 surface, and we could expect similar (or improved) emission. Still, the results indicated reduced emission in comparison with PSS1. From the comparison of these three PSS cathodes, we can draw three conclusions: 1) Cathode results in earlier tests cannot be directly compared with later tests. 2) Polishing a stainless steel rod with a consistent procedure does not lead to consistent cathode performance. 3) Misalignment of the anode vanes in the first generation of experiments increased the peak electric field in the earlier data.

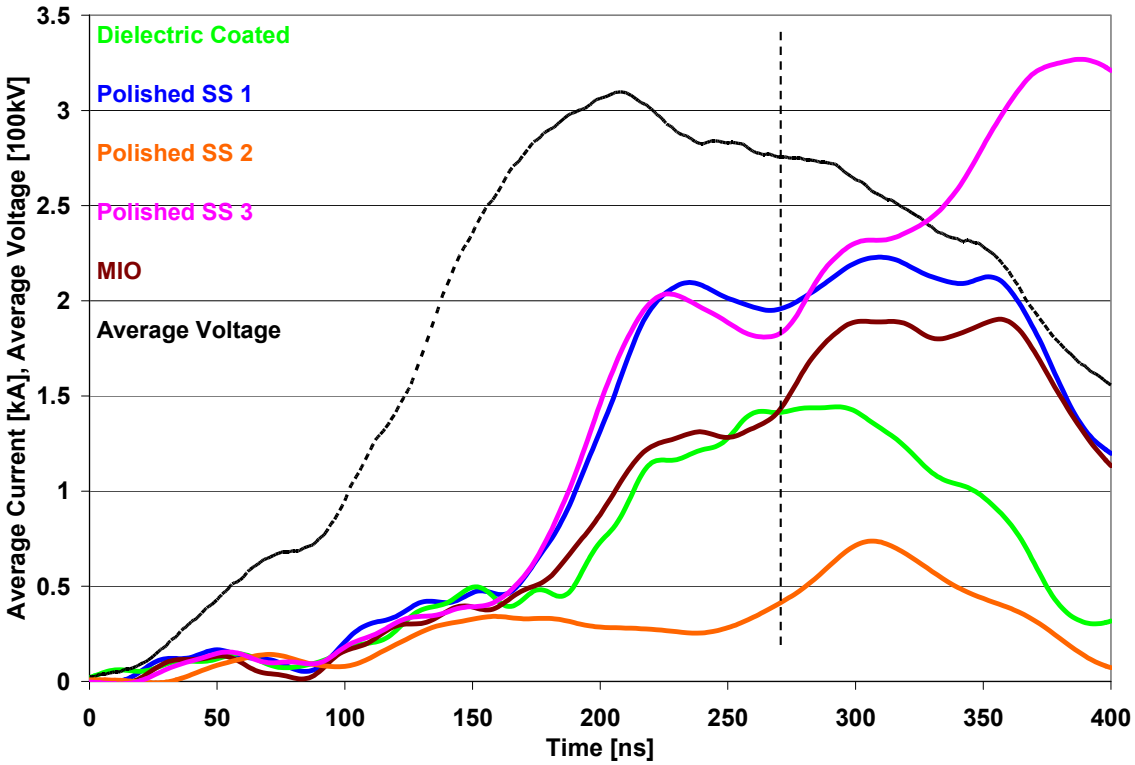

Figure 6.11 Averaged current traces for baseline DiCoat, PSS, and MIO cathodes, B ≈ 2.35 kG. Average voltage is shown in black.

Figure 6.11 is produced by averaging the current traces of all "low" magnetic field shots for each cathode, where the magnetic field is 2.35 ± 0.05 kG. This average is based on approximately 10 shots for each cathode. The first 200-300 ns of the voltage pulse are consistent on a shot-to-shot basis, but the pulse length varies from 350-600 ns. As a result, the latter half of the current trace varies widely, and the average in this region is not meaningful. Figure 6.12 displays an example of this effect, where the current and voltage traces show a similar shape in every shot, but only at times earlier than 300 ns. The dashed vertical line in Figure 6.11 is a visual indicator that data to the left of the line are more representative of each individual shot.

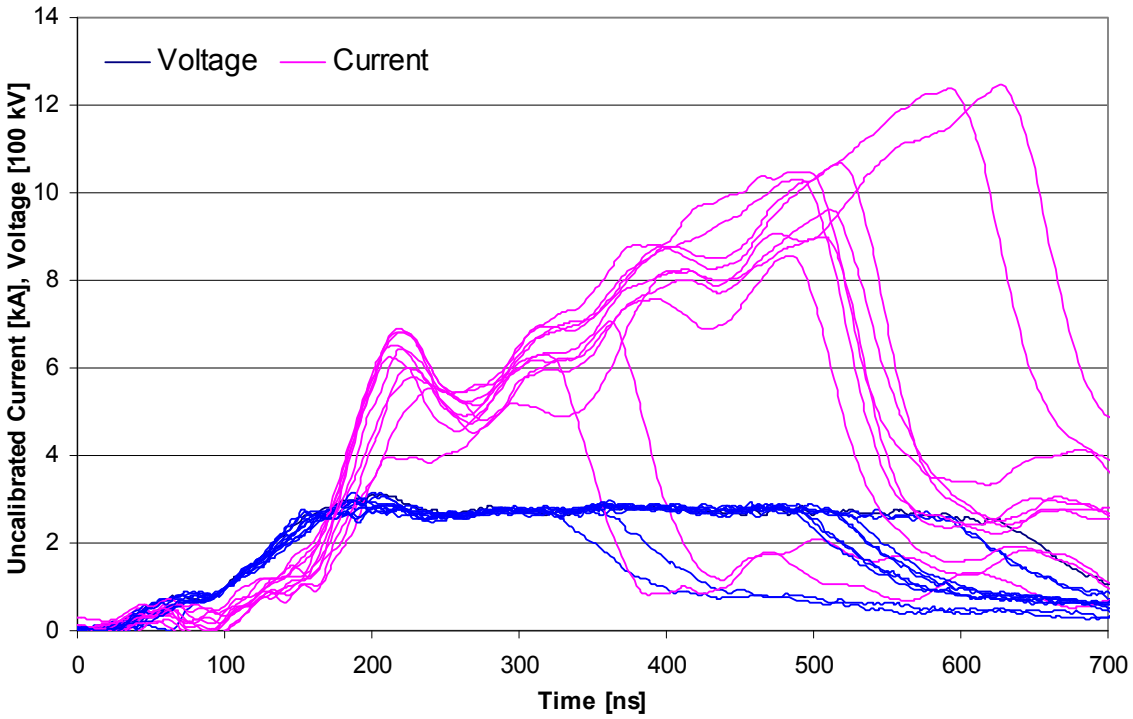

Figure 6.12 Current and voltage traces of MOJ-01 (Low B field) before averaging. Voltages are very consistent from 0 to 300 ns.

The sample-to-sample variation in emission thresholds for stainless steel cathodes has been noted previously [Lem88]. Those experiments, conducted at AFRL, found emission thresholds of stainless steel to vary from 230-380 kV/cm, compared to the narrower range of 220-250 kV/cm for copper. When the stainless steel was “greened” (by heating to near-melting temperatures in a wet hydrogen environment) to form a thin chromium oxide coating, samples obtained threshold fields of up to 425 kV/cm.

Simulations of the UM/Titan relativistic magnetron, performed by D. M. French using Maxwell 2D, show the peak electric field on the cathode surface is 290 kV/cm at peak voltage (-300 kV). This indicates, without additional field enhancement, field emission may not occur for some stainless steel cathodes. Data from PSS1 and PSS2, however, exhibit current turn on for voltages as low as -80 kV. For PSS1 this could be attributed to electric field enhancements from the misaligned anode vanes, but this problem was corrected for the test of PSS2. PSS3 exhibited emission at any non-zero voltage level (within the capabilities of our measurement setup). However, it should be noted that the UM cathodes

were tested in coaxial crossed *E* & *B* fields rather than a planar geometry with *B*=0 at AFRL. Consequently, the UM experiments exhibited significant electron back-bombardment, which would lower the electron emission threshold electric field.

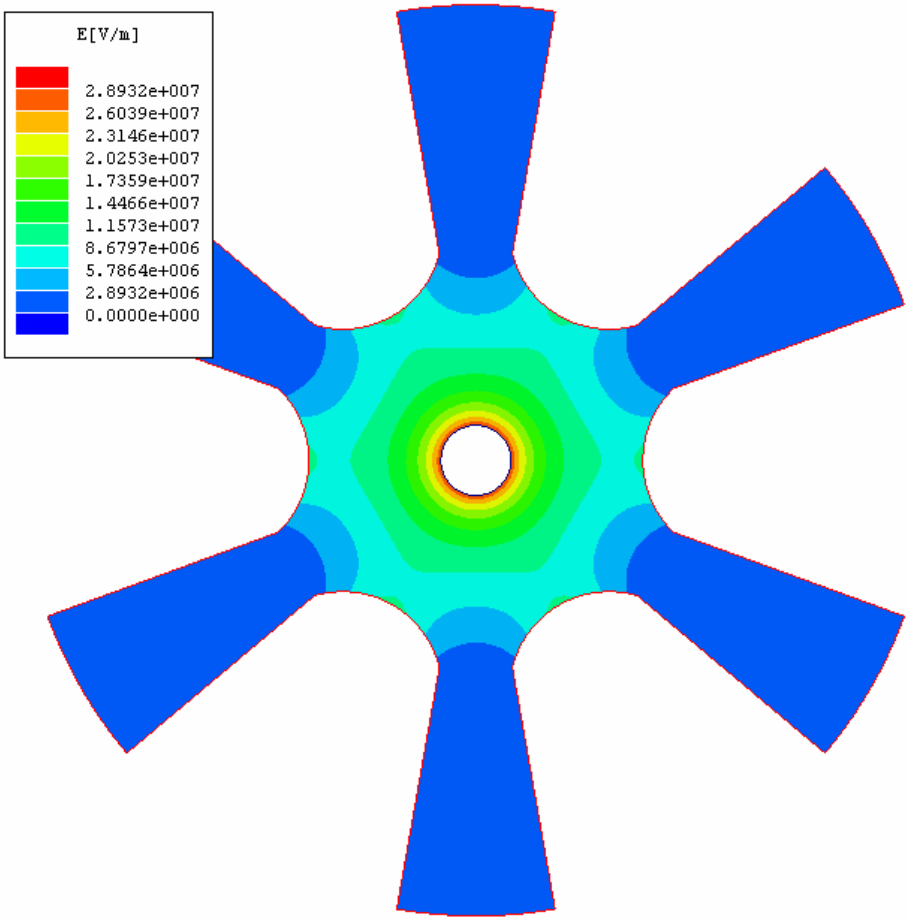

Figure 6.13 Maxwell 2D simulation of electric fields inside the UM/Titan relativistic magnetron. Cathode is biased to -300 kV.

6.2.2 MOJ-01, 02, & 03

The first "generation" of MOJ cathodes was tested from December 2006 to June 2007. The key variations between the designs were the mesh and laser fluence used during fabrication. MOJ-01 used a woven wire mesh, creating poor surface contact during deposition and indistinct dielectric islands, but also utilized a laser fluence of 30 J/cm^2, resulting in large amounts of surface particulate. MOJ-02 (Figure 3.13) & 03 (Figure 3.14) both used perforated meshes and ~3 J/cm^2 laser fluence for greatly reduced surface particulate (Figure 3.10 &

Figure 3.11). The mesh used for MOJ-02 (Mesh B) created the largest dielectric "islands" and the best island separation of any mesh tested.

Similar to the previous section, we present the results of these tests as a set of averaged current traces. The polished stainless steel case is also included for comparison, as it was tested in roughly the same time period. We see from Figure 6.14 that MOJ-01 & 02 produced the most current, while MOJ-03 was no better than PSS1. MOJ-01 was inadvertently tested at a slightly lower magnetic field (2.27 kG) than MOJ-02 & 03 (2.35 kG). This is relevant because current production for all cathodes was inversely proportional to magnetic field strength (Figure 6.18). The dashed red line in Figure 6.14 indicates the current corrected for the magnetic field. This correction is based on the scaling shown in Figure 6.18.

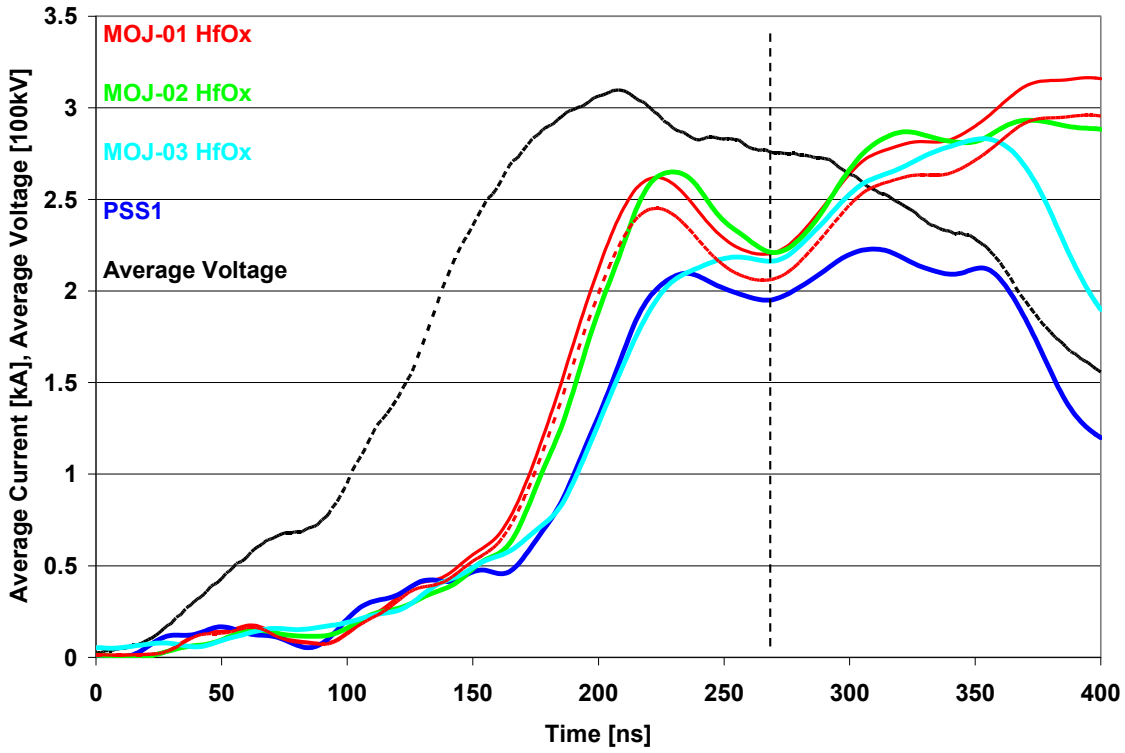

Figure 6.14 Averaged current traces for MOJ-01, 02 & 03 cathodes, B ≈ 2.35 kG. The PSS cathode is shown for comparison. Average voltage is shown in black. The dashed red line is MOJ-01 adjusted for magnetic field.

After accounting for magnetic field differences, MOJ-02 produced the highest average current, likely due to the improved dielectric separation its mesh

provided. MOJ-01, however, had poor separation of its dielectric islands, yet still produced a large amount of current. This is likely due to its large quantity of surface particulate. In section 5.2.1 we examined an individual piece of particulate, and found it to be primarily hafnium. If the dielectric islands on the cathode surface contain large amounts of particulate, they are each a source of additional triple points. Moreover, the particulate diameter is much larger than the film thickness, and creates triple points with $\theta < 0$, as diagrammed in Figure 6.15. In Chapter 2, this angle was shown to be favorable for field enhancement and secondary electron emission.

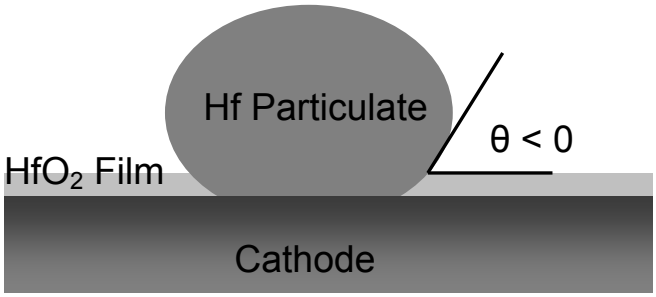

Figure 6.15 Diagram of triple points caused by surface particulate. Film thickness is <1 μm, particulate diameter ranges from 1-15 μm.

The poor performance of MOJ-03 is attributable to both its poor dielectric island separation, and lack of surface particulate. Given that MOJ-01 had even less distinct islands but still produced high current, the particulate may be the dominant factor.

6.2.3 MIO and DiCoat

While we have established that MOJ cathodes improve current production beyond that of polished stainless steel, we have not yet eliminated particulate field enhancement as the source of the increased emission. To rule this out, we tested the Metal Island Only (MIO) cathode. The MIO cathode was fabricated in the same setup as the MOJ-01 cathode, but at 10^{-6} Torr, rather than 100 mTorr O_2/Ar background. This results in large amounts of particulate, but no dielectric to form triple points. Some surface oxidation will still occur when the cathode is exposed to air, but that thin oxide layer is likely to be removed in the first cathode test.

Another possible source of current is plasma production from the dielectric. To ensure that the bulk dielectric is not the source of the additional current, we tested the Dielectric Coated (DiCoat) cathode. The DiCoat cathode is simply a polished stainless steel cathode coated with a layer of hafnium oxide dielectric. We would expect this dielectric coating to insulate the cathode, reducing electron emission. This is verified in the results shown in Figure 6.16.

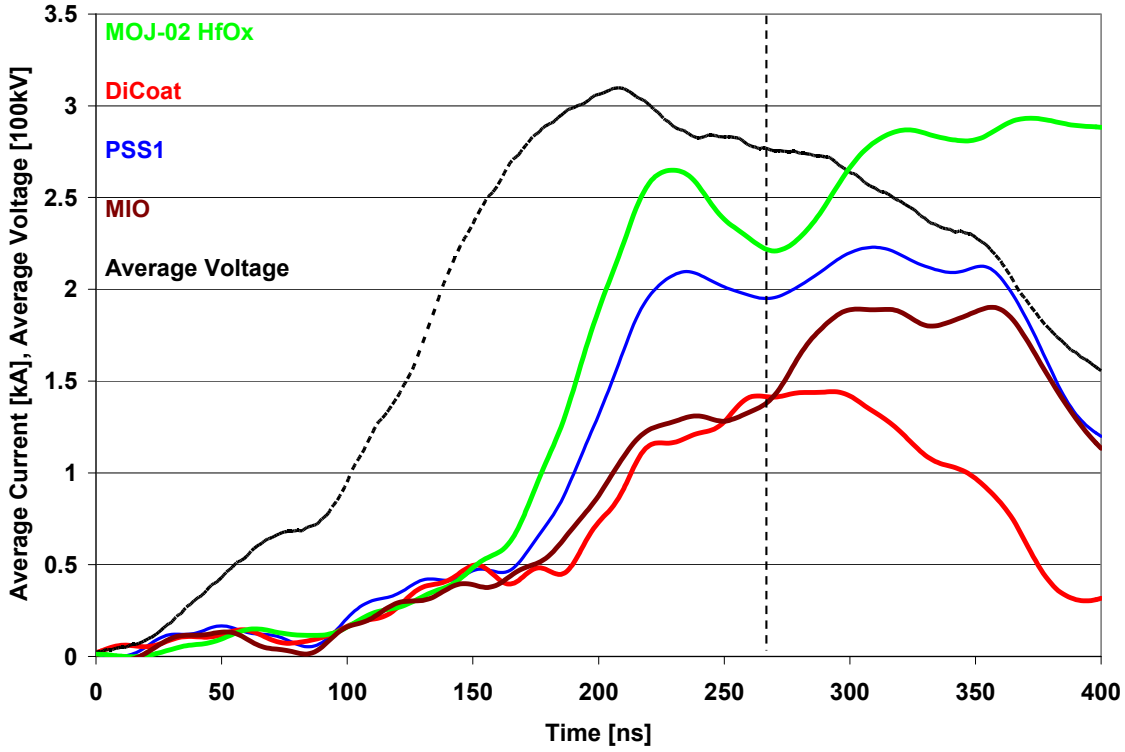

Figure 6.16 Averaged current traces for MIO and DiCoat cathodes, B ≈ 2.35 kG. PSS1 and MOJ-02 are shown for comparison. Average voltage is shown in black.

As expected, the dielectric coated cathode performed worse than PSS1. While the MIO results verify that particulate field enhancement is not the source of the increased emission, it is somewhat unexpected that the results are also below that of PSS1. It should be noted that the MIO cathode was tested much later than the "first generation" cathodes, the importance of which will be discussed further in the following section.

6.2.4 MOJ-04, 05, & 06

The second “generation” of MOJ cathodes was tested from October to December 2007. In August 2007, between testing of the first and second generation of MOJ cathodes, the magnetron was partially disassembled for an unrelated experiment. Following the reassembly, all cathodes in the magnetron appeared to be producing reduced currents. Consequently, this adds a large degree of uncertainty to any direct comparisons between the two generations of cathodes. In an attempt to quantify the change in magnetron performance, PSS2 and PSS3 were tested, as outlined in section 6.2.1. The reduced current of PSS2 (compared to PSS1) revealed that the mis-aligned vanes during testing of the first generation significantly impacted the measured current. PSS3 was tested within a week of PSS2, with corrected alignment for both, but still produced vastly different results. From this, we discovered the surface treatment of the PSS cathodes, and possibly even the batch of stainless steel used, could have a large effect on their emission properties.

In another attempt to correlate the first and second generations, we retested the MOJ-01 cathode (these data are labeled MOJ-01b). This cathode had not shown a decrease in current as a function of shot number, and should not have deteriorated in any way during the year it was unused and stored in air, under protective plastic. As such, it was a viable choice for verifying suspected changes in magnetron operation or diagnostics. As Figure 6.17 shows, the retesting of MOJ-01 resulted in greatly reduced current.

The second generation of cathodes was designed to test possible emission theories resulting from the first generation. First, particulate is an important source of additional triple points. This was tested in MOJ-04, which used the same mesh as MOJ-02 (for good separation of the dielectric islands), while also using a high laser fluence for increased particulate. Second, MOJ-05 reduced the triple point length-density, a measure of the triple point length per unit area solely attributable to the edges of the dielectric islands. Finally, MOJ-06 tested the role of secondary electron emission, using MgO as the dielectric instead of HfO_2. MgO has a secondary electron emission coefficient of 17-25

[Whe58], higher than the SEE coefficient of ~2 for hafnium oxide that we estimated in Section 5.2.2.

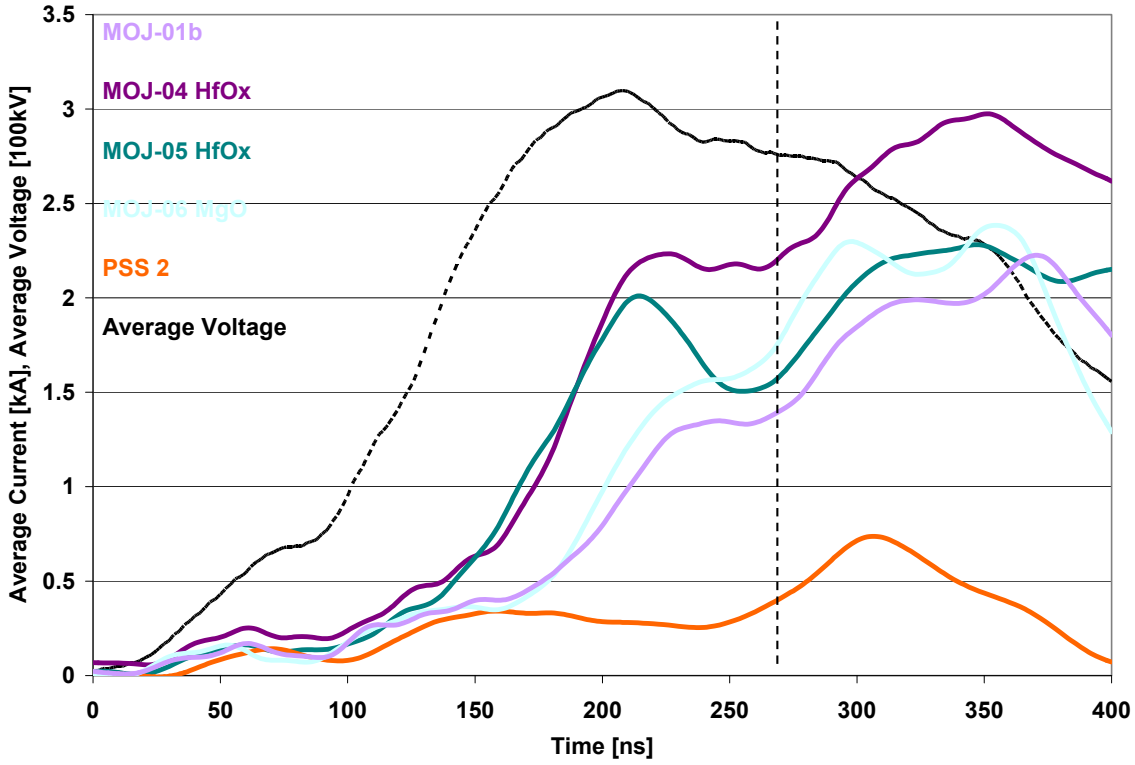

Figure 6.17 Averaged current traces for MOJ-04, 05, & 06 cathodes, B ≈ 2.35 kG. PSS2, PSS3, and MOJ-01b are shown for comparison. Average voltage is shown in black. MOJ-01b indicates the second test of the original MOJ-01 cathode.

While the current of MOJ-01b is considerably lower than the magnetic field corrected MOJ-01 (1.35 kA vs. 2.45 kA @ 225 ns, Figure 6.14), all of the second generation cathodes appear to improve on the original. When compared to MOJ-01b, MOJ-04 shows the largest increase in current, with MOJ-05 closely behind. Both cathodes also have faster current rise times, a characteristic that leads to higher currents at microwave turn-on, as shown in section 6.2.5 below.

MOJ-06, testing secondary electron emission, produces only slightly more current than MOJ-01b, but also provides the best measure of current attributable to cathode patterning. The justification of that statement is as follows. PSS2, shown in orange in Figure 6.17, had very poor performance. This polished stainless steel cathode was tested, removed from the magnetron, and immediately used in the fabrication of MOJ-06. MOJ-06 was tested the very next

day, so nothing had changed in the magnetron and we had an ideal baseline for comparison. While MOJ-04 & 05 could be compared to PSS2, as they were all tested in roughly the same timeframe, they are not guaranteed to possess the exact same surface roughness or bulk metal composition.

6.2.5 Additional MOJ Comparisons

To this point, we have focused almost solely on the average current performance of each cathode, as that is the primary goal of these cathodes. In this section we will discuss a few other methods of quantifying emission current, as well as other metrics used to characterize cathode performance.

We begin by considering the average magnetic field, Figure 6.19. While this is not a function of the cathode (Figure 6.18 shows that it impacts emitted current for all MOJ cathodes), a consistent magnetic field increases the quality of comparisons between cathodes.

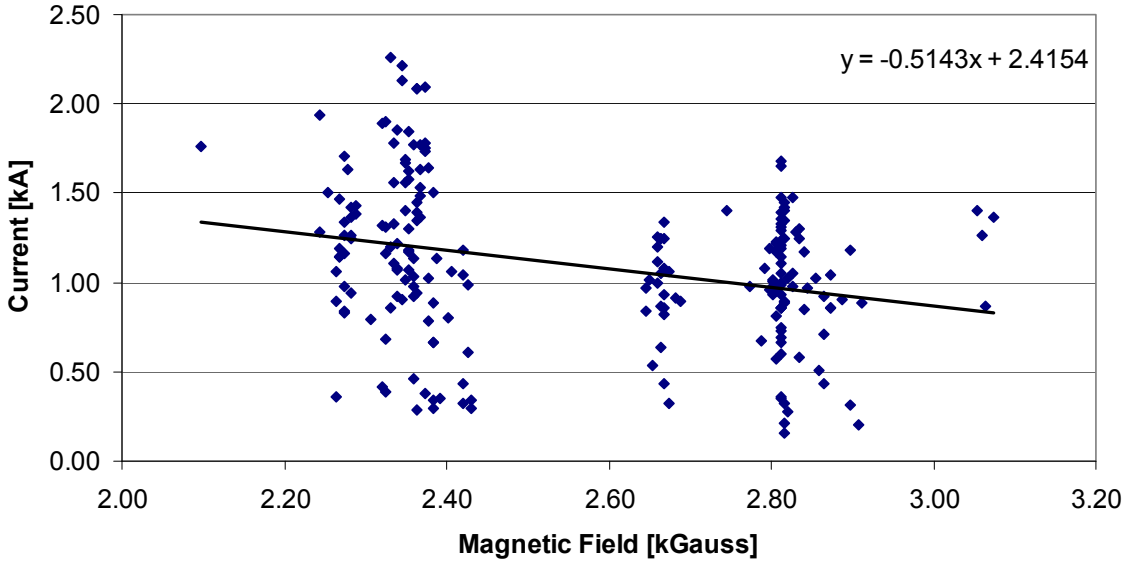

Figure 6.18 Current vs. magnetic field for all MOJ and baseline cathodes. The linear fit shows current to be inversely proportional to magnetic field. High and low magnetic field tests were conducted on alternating shots for every cathode, to eliminate any trends that might arise as a function of shot number.

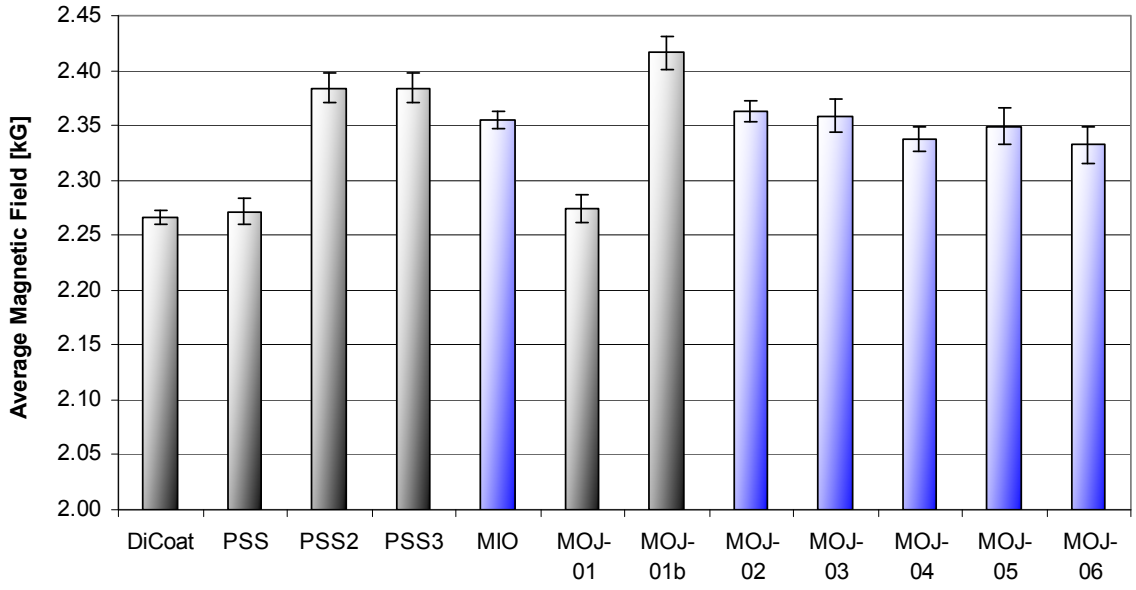

Figure 6.19 Average (low) magnetic field for each cathode. Each cathode was tested with magnet charging voltages of 3.6 kV (low) and 4.32 kV (high) to produce target magnetic fields of ~2.35 kG and ~2.82 kG, respectively. Cathodes with magnetic fields not significantly different from the target field are shown in blue.

At a 0.05 significance level, a T-test reveals the B-fields used to test MOJ-02 through MOJ-06, as well as MIO, are not significantly different. As mentioned previously, the magnetic fields used in testing DiCoat, PSS1, and MOJ-01 are all significantly lower than the intended 2.35 kG field, while PSS2, PSS3, and MOJ-01b are all significantly higher. This result, coupled with the trend shown in Figure 6.19, should be taken into consideration when comparing current results.

Microwave oscillation frequency is an important concern for relativistic magnetron operation. It is usually desirable for the magnetron to operate in the π-mode, which lies above 980 MHz in our magnetron. The Buneman-Hartree condition stipulates that for π-mode operation we must apply a magnetic field of approximately 3 kG. These cathodes are all tested at fields well below 3 kG, but this critical field value is a function of the magnetron geometry, and will change if the cathode radius changes. The physical radius is unchanged, since all the cathodes use the same 1.77 cm diameter stainless steel, but the effective radius will increase if plasma is produced. Analyzing the oscillation frequency of each cathode may give an indication of how much plasma it is producing.

Figure 6.20 shows the average microwave oscillation frequency. Cathodes shown in blue indicate π-mode operation, as determined by a T-test at a 0.05 significance level. There was no distinct trend among the MOJ cathodes with respect to π-mode operation (and, consequently, plasma production), though the PSS cathodes operated at lower frequencies as expected.

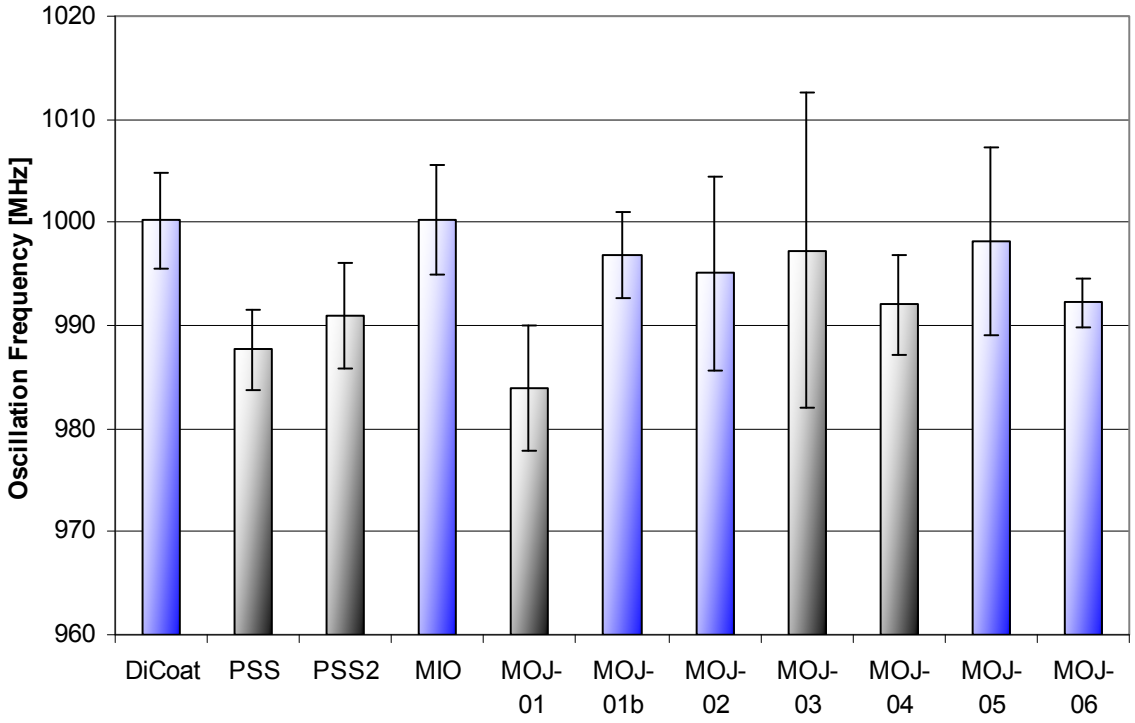

Figure 6.20 Average microwave oscillation frequency for each cathode. Cathodes with significant π-mode oscillation are shown in blue.

In previous sections, we compared the average current traces for each cathode. If we are to measure the current at a specific time, the peak microwave power is a sensible place to do so. While the microwave startup time may be an even better choice in some respects, the drawback is the increased sensitivity to noise. The current at the peak microwave power gives a measurement of the current available to the magnetron for conversion into RF energy.

Figure 6.21 displays the current for each cathode when the microwave power for that cathode is at its peak. The results are relatively consistent with what we have seen previously. The MOJ cathodes produce higher currents than the baseline cases, and MOJ-05 & MOJ-06 perform worse than the first test of

MOJ-01, but better than MOJ-01b. Note that none of these currents have been adjusted for deviations in magnetic field.

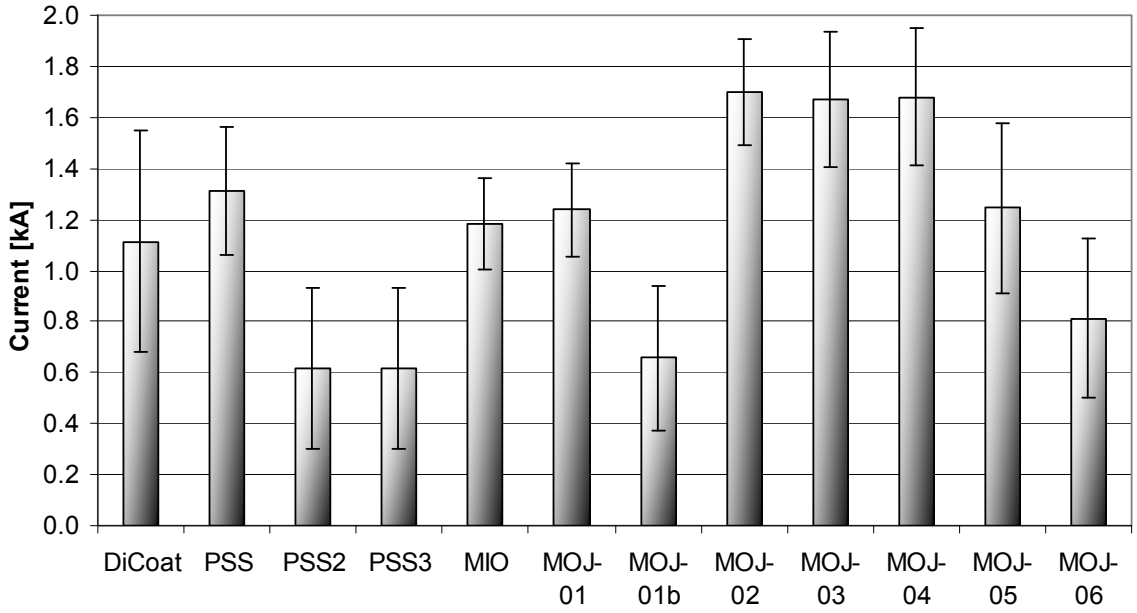

Figure 6.21 Average current at peak microwave power for each cathode.

For nearly every shot on every cathode, the microwave pulse begins (and usually also peaks) during the initial current rise. Consequently, cathodes with fast current rise times will have higher currents in Figure 6.21.

Another factor that could influence these results is the microwave startup time for each cathode. Delayed microwave startup would give "better" results in Figure 6.21, since the cathode current would be measured later in the current rise. Figure 6.22 shows there are not large variations in startup time. Performing a one-sample T-test on the data and comparing to the overall mean of 203 ns, only 4 cathodes are significantly different at a 0.05 confidence level, and only MIO is significantly different at a 0.01 level.

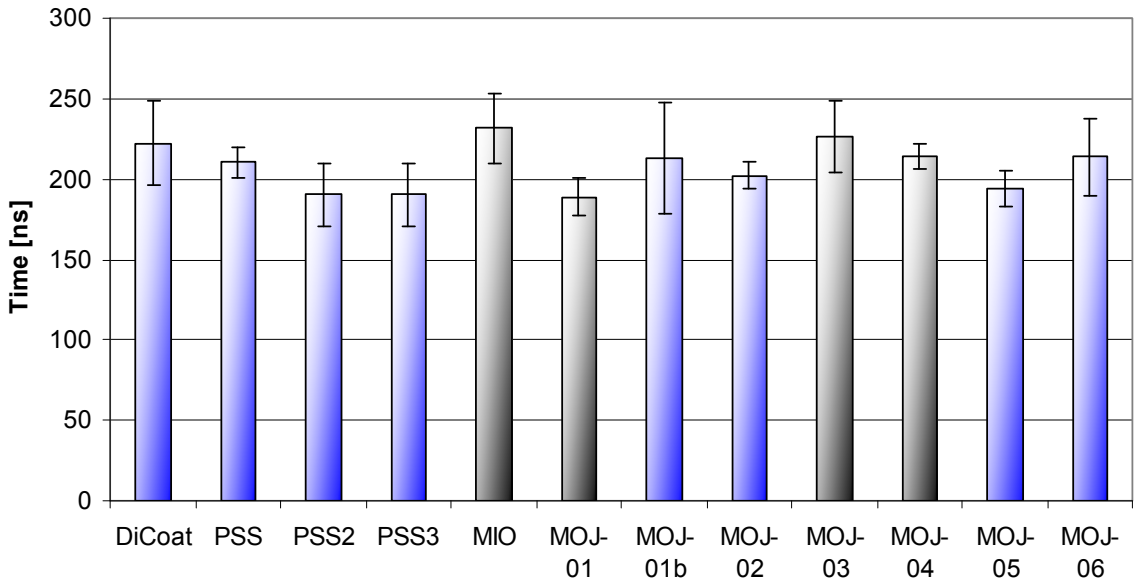

Figure 6.22 Time to peak microwave power (t=100 ns when V=100 kV, as previously defined). Cathodes which are not significantly different from the mean are shown in blue.

As a final comparison of all cathodes, we present Table 6.3, Figure 6.23 and Figure 6.24. This table gives the relevant fabrication parameters, as well as the current density of each cathode. The current density is calculated by subtracting the baseline current from the MOJ cathode current and dividing by the patterned area. The two current density values for each cathode indicate low and high magnetic field tests, respectively. Figure 6.23 and Figure 6.24 show the average current traces for low and high magnetic fields tests, respectively. The high field results have not been discussed in detail because they are virtually the same as the low field results, but with reduced emission currents.

Table 6.3 Summary of relevant MOJ cathode parameters. For current density, if the cathode produced less current than the baseline case, the current density reduction is shown in red.

	MOJ-01	MOJ-02	MOJ-03	MOJ-04	MOJ-05	MOJ-06	Dielectric Coated
Patterned Area [cm2]	7	12	28	34	28	20	50
Feature Size [µm]	950	1200	850	1200	1400	1200	N/A
Feature Spacing [µm]	0-300	250	50-250	250	1400	250	N/A
Peak Dielectric Thickness [nm]	900	300	450	900	900	900	500
Laser Fluence [J/cm2]	30	1.5	3.8	30	26	7	30
Sections	8	6	6	6	4	6	4
Pulses per Section	18000	18000	18000	18000	18000	18000	9000
Current Density [A/cm2]	77 - 79	29 - 48	0 - 2	4-6	2 - 11	65 - 35	12 - 19

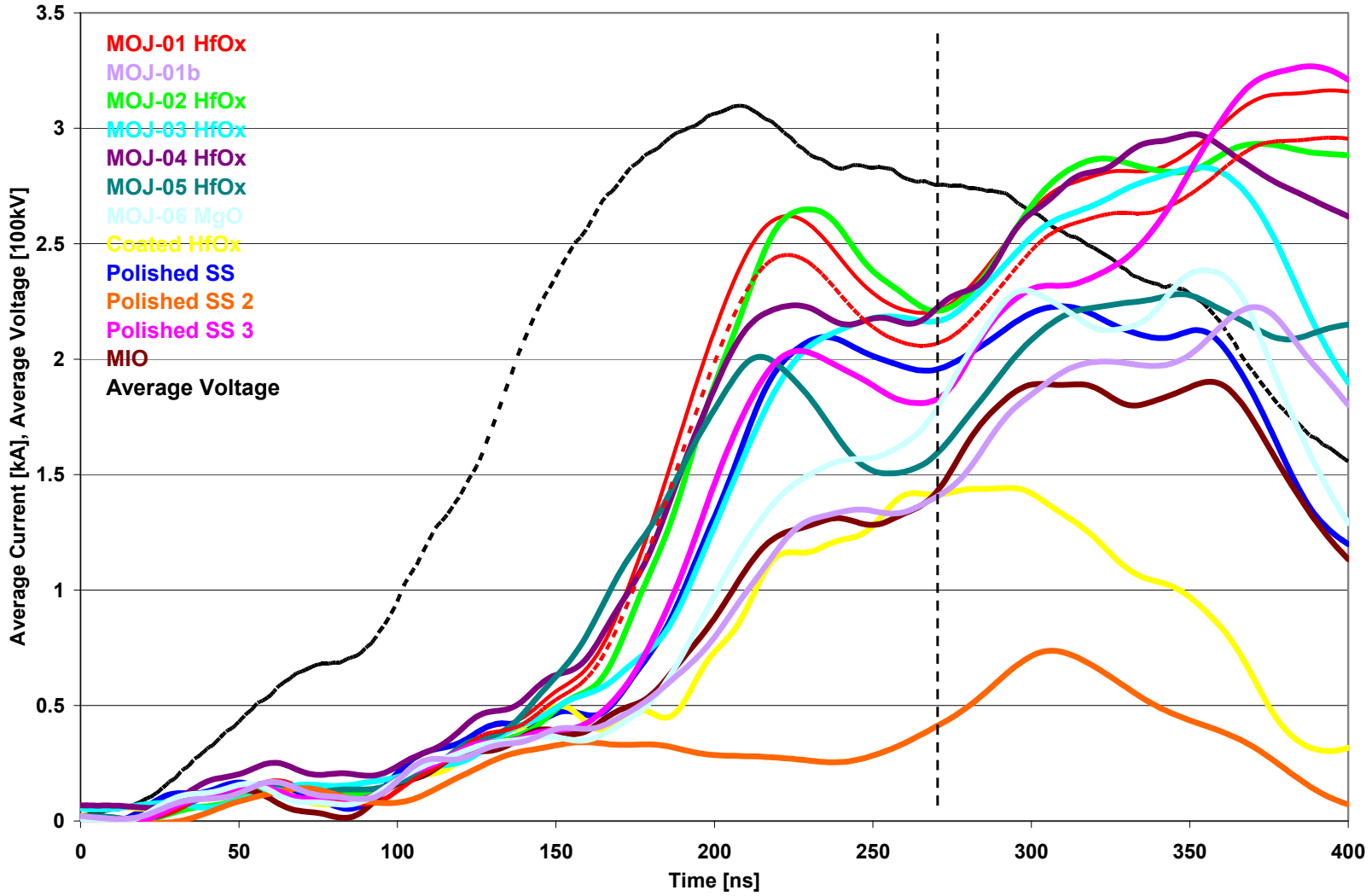

Figure 6.23 Average current traces for all MOJ and baseline shots at low magnetic field (≈2.35 kG).

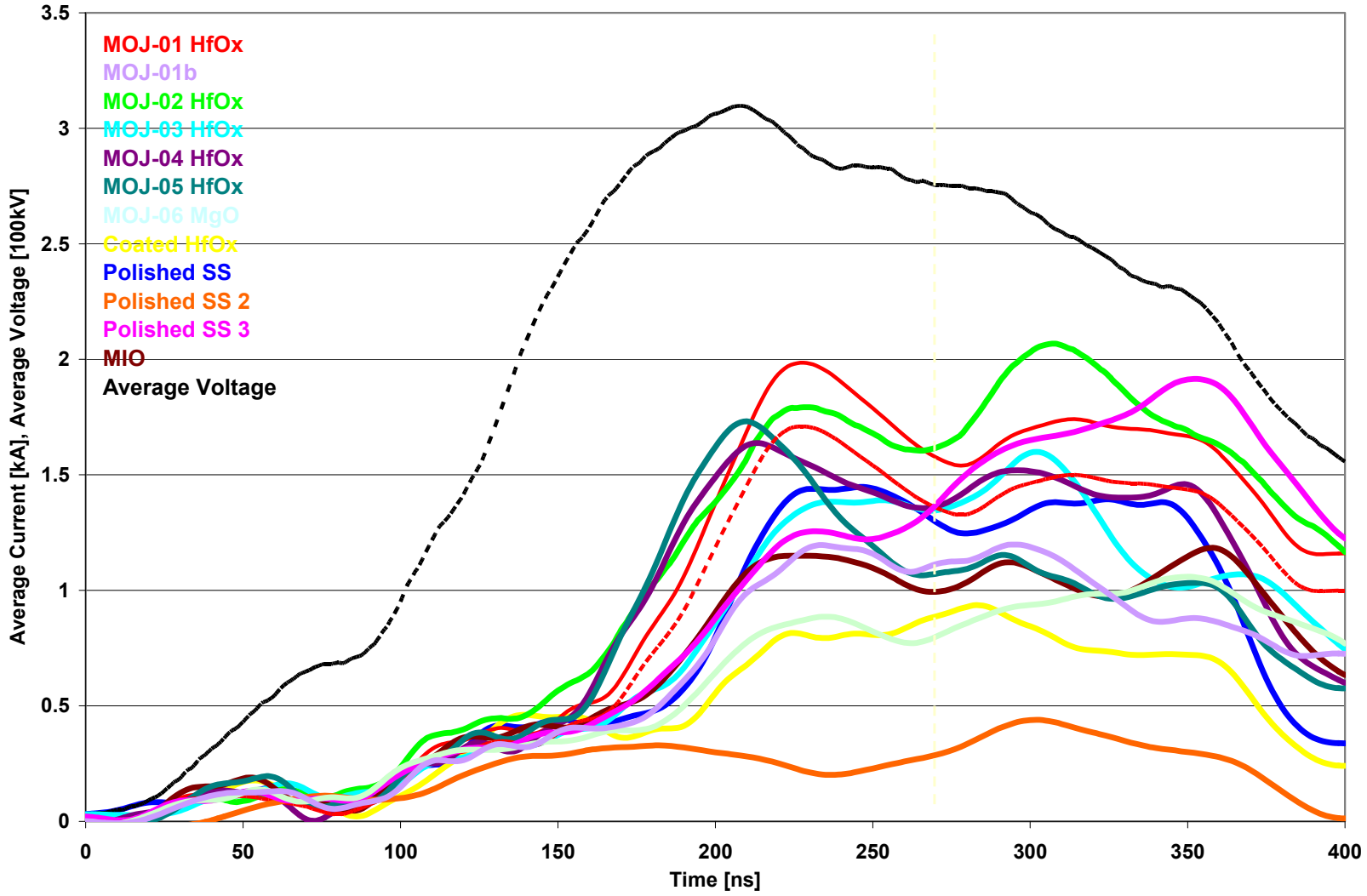

Figure 6.24 Average current traces for all MOJ and baseline shots at high magnetic field (≈2.82 kG).

CHAPTER 7
SUMMARY AND CONCLUSIONS

Two new cathode designs for cold cathode emission in a relativistic magnetron were presented, both theoretically and experimentally. We began with an overview of HPM and relativistic magnetron research, and followed with a brief summary of important emission fundamentals and recent work.

We then discussed the theory of field enhancement and electron emission at triple points. We calculated the orbit of the first generation electrons, the seed electrons. We found that, despite the mathematically divergent electric field at the triple point, significant electron yield most likely results from secondary electron emission when the seed electrons strike the dielectric. We also provided an explanation on why certain dielectric angles are more favorable to electron generation over others, as observed in previous experiments. As our analysis considers only seed electrons, we ignored dielectric charging and space charge effects, and did not account for initial velocity distributions or initial spatial distributions.

To test this theory in practice, we fabricated six metal oxide junction (MOJ) cathodes. These cathodes were created by ablating a Hf or MgO target in a 100 mTorr O_2/Ar environment, and depositing the resulting oxide through a mask. This creates many dielectric “islands” on the cathode surface, the edges of which form triple points. The ablation process, when executed at sufficiently high laser fluence, will generate large quantities of particulate. The particulates deposit on the cathode surface and proved to be an important contributor to the emission characteristics of the cathodes.

The first generation of cathodes consisted of MOJ-01, 02, & 03. MOJ-01 possessed large quantities of particulate, but poor dielectric island separation. Conversely, MOJ-02 had small amounts of particulate and distinct dielectric

islands. MOJ-03, however, had small amounts of particulate and dielectric separation slightly worse than MOJ-02. The final three MOJ cathodes comprised the second generation. MOJ-04 had both distinct dielectric islands and large quantities of surface particulate. MOJ-05 tested a different masking pattern, with decreased triple point length-density. Lastly, in MOJ-06 the dielectric material was changed from HfO_2 to MgO because a material with a high secondary electron emission coefficient was desired.

The cathode tests were divided into two generations, based on the date of testing, and further sub-divided into “low” (2.35 kG) and “high” (2.82 kG) magnetic field cases. Within the first generation, we verified the concept of the triple point cathode, showing 30% greater emission current when compared to either a polished stainless steel or dielectric coated cathode. Comparisons of the MOJ-01 & 03 cathodes indicated surface particulate may play a large role in current production through the creation of additional triple points. Comparing MOJ-02 & 03 revealed that distinct dielectric islands improve electron emission, likely due to the enhanced triple point length-density. We also found that the emission current is inversely proportional to magnetic field strength, and corrections were proposed for cathode tests with deviant magnetic fields.

Between the first and second generations the magnetron was disassembled, and it was discovered that the anode block was not seated properly. This resulted in non-uniform radial electric fields at the cathode surface, invalidating direct comparisons of the two cathode generations.

The second generation cathodes tested several theories of electron emission stemming from results of the first generation. First, however, we established a point of comparison between the two generations by re-testing the MOJ-01 cathode (these data are referred to as MOJ-01b). The second test of this cathode produced 50% lower currents when measured at the peak microwave power. Comparisons of MOJ-04 to MOJ-01b indicated that large amounts of particulate, coupled with distinct dielectric islands, improved the electron emission of the cathodes. MOJ-05, with lower triple point length density than other cathodes, showed that emission current is not directly proportional to

the total triple point length, suggesting edge/end effects may be important. MOJ-06 displayed the importance of secondary electron emission, by replacing the HfO_2 dielectric with MgO, which has a considerably higher secondary electron emission coefficient. While this cathode exhibited the least emission of the second generation of cathodes, direct comparisons with its stainless steel baseline resulted in a 30-500% current increase (depending strongly on the point of comparison).

In another method of linking the two generations of cathodes, we retested the cathode used in the original polished stainless test. The results changed dramatically, exhibiting a 60% reduction in current at peak microwave power, and as much as a 6x reduction in current at other points of measurement. To analyze the importance of cathode surface preparation, we prepared another polished stainless steel cathode which foregoes the final sanding step to ensure the roughest surface finish of any polished stainless steel cathode tested. This had a substantial impact on the emission, increasing the current by up to a factor of 8. We found that the exact composition and surface treatment of the stainless steel can have a significant impact on the final cathode performance.

Another design, the Ablation Line Focused (ALF) cathode, was also presented. This cathode is created by ablating 100 μm deep channels into the surface of a cathode stalk, using a 600 mJ (peak) KrF excimer laser. This increases the β of the surface, enhancing field emission. This was established as the baseline case, ALF-2.

Combining the ALF process with previous work on cathode priming, we presented two datasets from the Tri-ALF cathode. This cathode exhibited plasma closure and higher currents than ALF-2, but had mixed results with respect to microwave output. The first dataset, tested with microwave power measured out of only one waveguide, had poor microwave performance in all categories. The second dataset, with three power measurements, displayed greatly improved microwave performance, but inconclusive evidence of cathode priming. Carbon paint, designed to suppress electron emission on the cathode surface, may aid in plasma formation, inhibiting any cathode priming effects.

Analyses of the cathode surfaces were offered, with additional attention given to the hafnium oxide films used for MOJ cathodes, and a brief discussion of the plasma plumes generated during deposition. ALF cathodes were analyzed with mechanical profilometry, as well as scanning electron microscope (SEM) imaging. The hafnium oxide films were analyzed with SEM, X-ray Energy Dispersive Spectroscopy (XEDS), X-ray Diffraction (XRD), and profilometry. Additionally, film quality was examined through Capacitance-Voltage (C-V) testing.

The experimental configurations used for plasma spectroscopy, as well as the major components of the accelerator and relativistic magnetron, were also outlined. An explanation of the diagnostics associated with cathode voltage, cathode current, magnetic field, and microwave power were presented. Where applicable, the calibration procedures for these diagnostics were given.

APPENDICES

APPENDIX A
MELBA-C Circuit Diagram

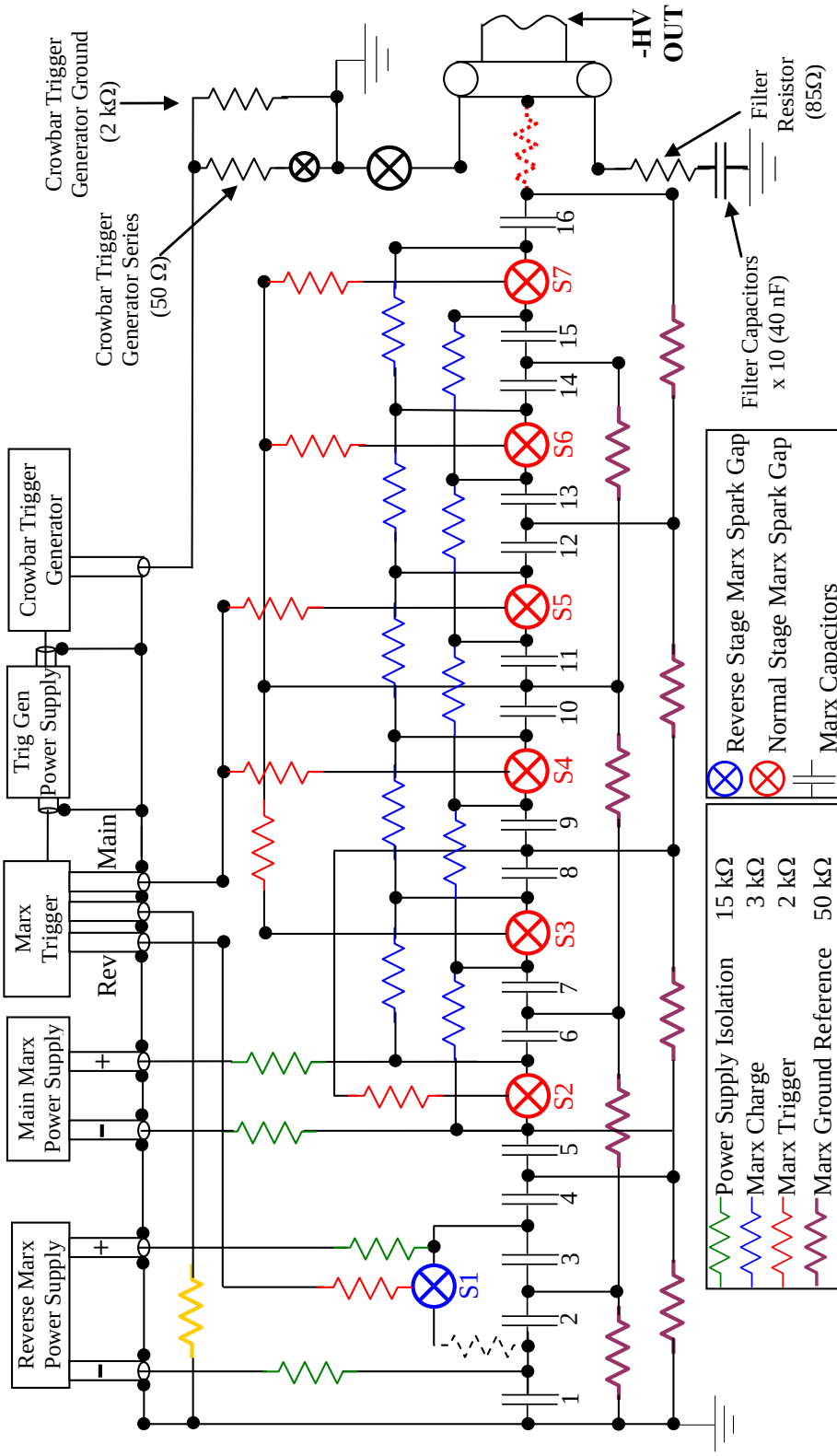

Figure A.1 MELBA circuit diagram from [Jon05].

APPENDIX B
Supplemental Theory

B.1 Magnetron Operation

A very brief overview of magnetron operation is given here. For more detailed explanations, see [Lop03, Jon05, Whi05]. A magnetron is a crossed-field device, meaning that the electric and magnetic fields are perpendicular to each other. A magnetron is classified as "relativistic" when the applied voltage is on the order of 511 keV, the rest mass enregy of an electron.

In the magnetron, electrons are emitted from the cathode surface and accelerated toward the anode by the electric field. Because a magnetic field is present, the electrons experience a Lorentz force ($q\left(\vec{E}+\vec{v}\times\vec{B}\right)$), and are accelerated back toward the cathode. This insulates the gap, and prevents current from streaming directly to the anode, Figure B.1.

The magnetic field required to insulate the diode is known as the Hull Cutoff, which is given in Eqn. (B.1) for a cylindrical geometry, accounting for relativistic effects [Ben07].

$$B_{Hull}=\frac{mc}{eD_{eff}}\sqrt{\frac{2eV}{mc^2}+\left(\frac{eV}{mc^2}\right)^2} \tag{B.1}$$

where D_{eff} is the effective gap, and all other symbols have their usual meanings.

For efficient interaction between the electron beam and RF wave, the magnetron must operate within a specific voltage-dependent magnetic field range. The most efficient, and usually most desirable, mode is the π-mode, where a 180° RF phase shift occurs between each anode cavity. The Buneman-Hartree resonance condition defines the relationship between the applied voltage and magnetic field, if synchronism is desired between the RF wave and electron beam. Equation (B.2) is the Buneman-Hartree resonance condition for a cylindrical geometry, accounting for relativistic effects [Ben07].

$$B_{BH}=\frac{mc^2n}{e\omega_n r_a D_{eff}}\left[\frac{eV}{mc^2}+1-\sqrt{1-\left(\frac{r_a\omega_n}{cn}\right)^2}\right] \tag{B.2}$$

where n is the mode number, ω_n is the frequency of the n^{th} mode, r_a is the anode radius, and D_{eff} is the effective gap. A diagram of the Buneman-Hartree condition and Hull Cutoff for the UM/Titan relativistic magnetron is provided in Figure B.2. For our operating voltage of 300 kV, a magnetic field of 1.4 kG is required for diode insulation, and a field of ~3 kG is desired for efficient π-mode operation.

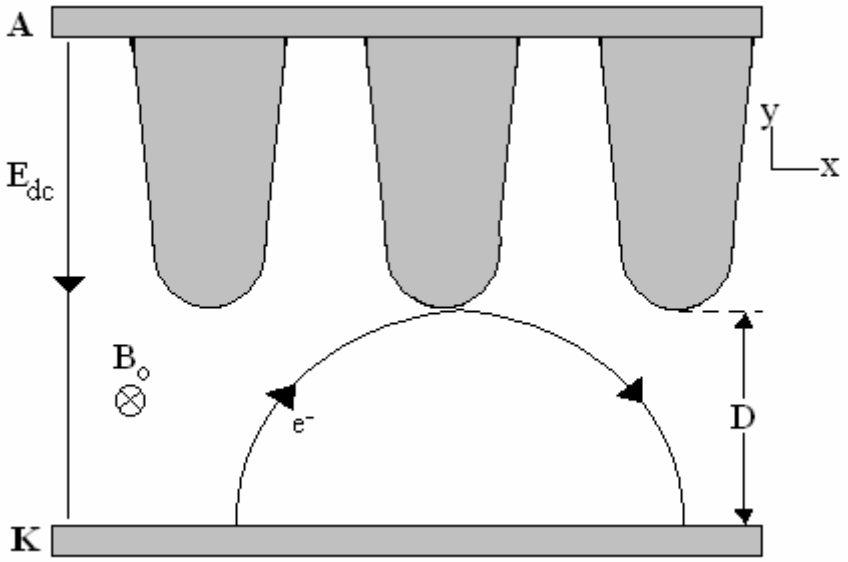

Figure B.1 Diagram of a planar magnetron showing the electron motion and relevant fields (image from [Whi05]). Though the actual magnetron is a cylindrical geometry, the motion is easier to visualize in planar format.

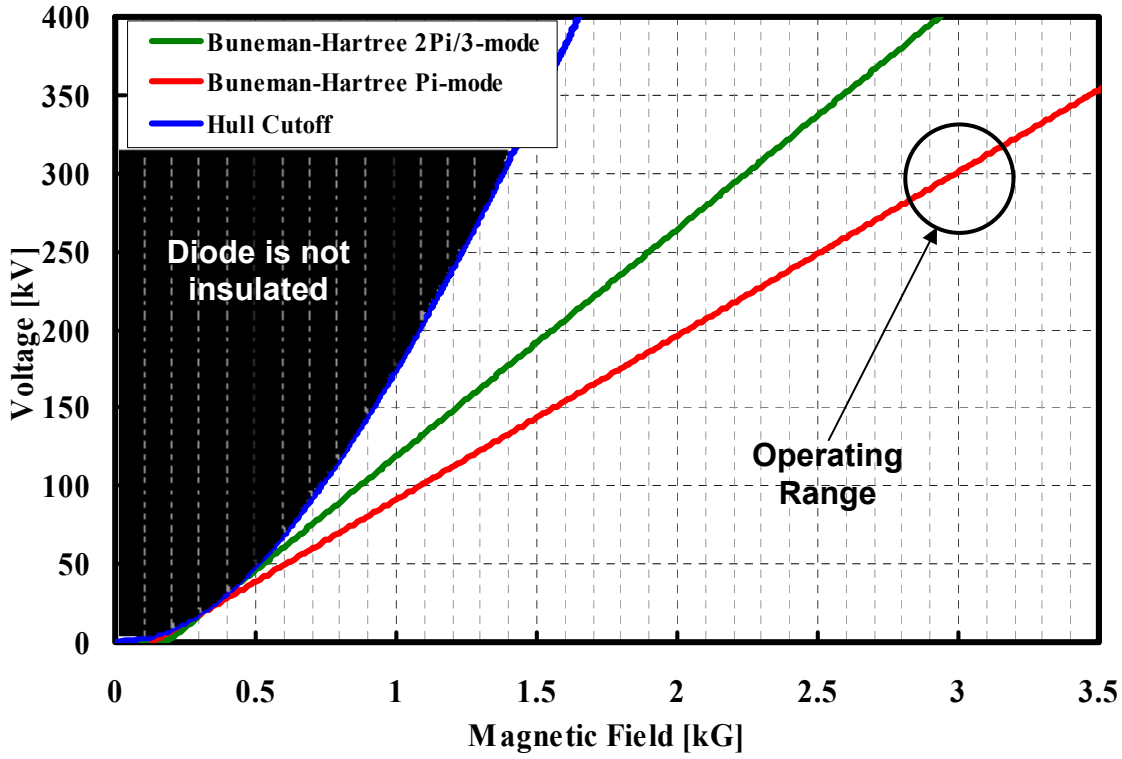

Figure B.2 Buneman-Hartree resonance conditions for the 2π/3- and π-modes, as well as the Hull cutoff condition for the UM/Titan relativistic magnetron (image from [Jon05]).

B.2 Inferred Plasma Closure Velocity Calculations

If a cathode has formed a plasma, and is operating according to space-charge limited emission in the absence of a magnetic field, the plasma closure velocity traditionally has been inferred from measurements of the perveance ($I / V^{3/2}$). We can compare this measured perveance to the theoretical perveance (derived from the Space Charge Limited Child-Langmuir law) [Lan22, Dow52],

$$P = \frac{I}{V^{3/2}} \approx 14.68 \times 10^{-6} \frac{L}{r_a \beta_1^2}$$
$$\beta_1 = y - \frac{2}{5} y^2 + \frac{11}{120} y^3 - \frac{43}{3300} y^4 + \ldots \qquad y = \ln\left[\frac{r_a}{r_c + v_c t}\right] \tag{B.3}$$

where L is the effective length of the emission region, r_a is the anode radius, r_c is the cathode radius, v_c is the plasma closure velocity, and t is time elapsed since plasma formation.

To determine the closure velocity, the experimental and theoretical values of $1/\sqrt{P}$ are plotted over the voltage flat-top. The experimental value is then fit with a linear trendline and the effective length and plasma closure velocity are adjusted to achieve the best match of the theoretical curve. Adjustment of the closure velocity primarily affects the slope of the line, while the effective length primarily affects the y-intercept.

This analysis makes the (often questionable) assumption of Space Charge Limited emission, but is particularly useful in long voltage pulse shots with obvious plasma closure. While the effective emission length is hard to predict, we would expect it to be consistent for any given cathode, but this is not always the case. These analyses must be taken with a grain of salt, as the effect of the crossed magnetic field is not included.

APPENDIX C
Directory of Program Code

This appendix contains descriptions of programs I have written as well as their electronic locations. All my data, program code, and electronic copies of presentations and thesis, can be found on the fileserver (plasma-fs), under student data.

A program to control the rotary stage during ablation of ALF cathodes is contained in a LabVIEW 8.2 library titled *ALF Automation.llb*. The program has 3 modes: one that simply rotates the cathode, one that rotates and fires the laser a set number of times, and one that just fires the laser. The program is designed to be used in conjunction with a BNC-555 pulse generator, to control when the laser will be fired, as well as the rep rate.

The LabVIEW UIs to analyze MELBA data are contained in the Data Analysis Tools\MELBA Labview folder. These UIs replace the function of Megagui, allowing the user to view the voltage, current, magnetic field, and microwave power data. The *Phase Math* VI is designed for use with a 4 channel phase discriminator, to calculate the phase of the microwave oscillation.

All Excel macros are in Word file called “Excel Macros”. Most macros have a description of their functions within the macro comments.

BIBLIOGRAPHY

Abr77 E. A. Abramyan, B. A. Altercorp, and G. D. Kuleshov, “Microsecond intensive electron beams,” Proceedings of the Second International Topical Conference on High Power Electron and Ion Beam Research and Technology, vol. 2, pp. 755-760, 1977.

Adl85 R. J. Adler, G. F. Kiuttu, B. E. Simpkins, D. J. Sullivan, and D. E. Voss, “Improved electron emission by use of a cloth fiber cathode”, Review of Scientific Instruments, vol. 56, no. 3, pp.766-767, 1985.

And80 R. A. Anderson and J. P. Brainard, Journal of Applied Physics, vol. 51, pp. 1414, 1980.

And94 W. A. Anderson, Journal of Vacuum Science and Technology, B11, 383, 1993; Y. Y. Lau, Y. Liu, and R. K. Parker, Physics of Plasmas, vol. 1, pp. 2082, 1994.

Ang98 L. K. Ang, Y. Y. Lau, R. A. Kishek, and R. M. Gilgenbach, IEEE Transactions on Plasma Science, vol. 26, 290, 1998.

Ans07 Ansoft Corporation; http://www.ansoft.com.

Bag00 V. Baglin, Y. Bozhko, O. Gröbner, B. Henrist, N . Hilleret , C. Scheuerlein, M. Taborelli, Proceedings of 7th European Particle Accelerator Conference, Vienna, Austria, pp. 217-221, 2000.

Bar01 R. J. Barker and E. Schamiloglu, *High-Power Microwave Sources and Technologies* (IEEE Press, New York, 2001).

Ber77 K. D. Bergeron, Journal of Applied Physics vol. 48, 3073, 1977.

Ben07 J. Benford, J. A. Swegle, E. Schamiloglu, *High Power Microwaves*, Taylor & Francis, New York, 2007.

Boo07 J. H. Booske, X. He, R. L. Miller, D. M. Morgan, J. E. Scharer, V. Vlahos, R. M. Gilgenbach, N. M. Jordan, Y. Y. Lau, Y. Feng, and J. B. Verboncoeur, *Proceedings of the 34th IEEE International Conference on Plasma Science, Albuquerque, NM* (IEEE, Piscataway, NJ, 2007), p.350.

Chr94 D.B. Chrisey and G.K. Hubler, *Pulsed Laser Deposition of Thin Films*, Wiley, New York, 1994.

Chu04 M.S Chung, B.G. Yoon, P.H. Cutler, N.M. Miskovsky, Journal of Vacuum Science and Technology, B22, p. 1240, 2004.

Cun99 M. E. Cuneo, IEEE Transactions on Dielectrics and Electrical Insulation, vol. 6, 469, 1999.

Det73 C. H. De Tourreil and K. D. Srivastava, IEEE Transactions on Electrical Insulation EI-8, vol. 17, 1973.

Dow52 W. G. Dow, *Fundamentals of Engineering Electronics*, Wiley, New York, 1952.

Duq86 D.W. Duquette, E.A. Den Hartog, and J.E. Lawler, Journal of Quantitative Spectroscopy and Radiative Transfer, vol. 35, No. 4, pp. 281-301, 1986.

Edm06 G. Edmiston, J. Krile, A. Neuber, J. Dickens, and H. Krompholz, IEEE Transactions on Plasma Science, vol. 34, p. 1782, 2006.

Fow28 R. H. Fowler and L. Nordheim, Proc. R. Soc. London Ser A, vol. 119, p. 173, 1928.

Gam93 G. Gammie, R. Kozlowski, R. Mallavarpu, and A. Palevsky, "Field Emission Arrays for Microwave Applications", *IEEE Electron Devices Technical Digest*, Washington, DC, 1993.

Gil85 R. M. Gilgenbach, L. D. Horton, R. F. Lucey, S. Bidwell, M. Cuneo, J. Miller, and L. Smutek, "Microsecond electron beam diode closure experiments", 5th IEEE Pulsed Power Conference, June 1985.

Gil86 A. S. Gilmour, *Microwave Tubes* (Artech house, Norwood, MA, 1986.

Gil05 R. M. Gilgenbach, Y. Y. Lau, H. McDowell, K. L. Cartwright, and T. A. Spencer, in *Modern Microwave and Millimeter Wave Power Electronics*, Eds.: R. J. Barker, J. H. Booske, N. C. Luhmann, and G. S. Nusinovich (IEEE Press, Piscataway, 2005); Ch. 6, p. 289.

Hac59 O. Hachenberg and W. Brauer, *Secondary Electron Emission from Solids*, Ed.: L. Marton, Advances in Electronics and Electron Physics Vol. XI (Academic Press, New York 1959), pp. 413-499.

He07 X. He, J. Scharer, J. Booske, V. Vlahos, S. Sengele, N. M. Jordan, and R. M. Gilgenbach, "Measurements and Analysis of Advanced Field Emission Cold Cathodes", IEEE International Vacuum Electronics Conference, May 2007.

Hen07 The Hendrix Group, http://www.hghouston.com/ss_comp.html.

Her87 M. E. Herniter and W. D. Getty, IEEE Transactions on Plasma Science, vol. 15, pp. 351-360, 1987.

Hin85 D. Hinshelwood, “Explosive emission cathode plasmas in intense relativistic electron beam diodes”, Ph.D. Thesis, Massachusetts Institute of Technology, 1985.

Hof08 B. W. Hoff, R. M. Gilgenbach, N.M. Jordan, Y.Y. Lau, E. Cruz, D. French, M.R. Gomez, J.C. Zier, T.A. Spencer, and D. Price, IEEE Transactions on Plasma Science, Special Issue on High Power Microwave Generation, T.B.P June 2008.

Hol68 W. L. Holtgreven, *Plasma Diagnostics*, North-Holland Publishing Co., Amsterdam, 1968.

Hud65 R.H. Huddlestone and S.L. Leonard, *Plasma Diagnostic Techniques*, Academic Press, New York, 1965.

Jon04a M. C. Jones, V. B. Neculaes, Y. Y. Lau, R. M. Gilgenbach, and W. White, Applied Physics Letters, vol. 85, pp. 6332-6334, 2004.

Jon04b M. C. Jones, V. B. Neculaes, W. White, Y. Y. Lau, and R. M. Gilgenbach, Applied Physics Letters, vol. 84, pp. 1016-1018, 2004.

Jon04c M. C. Jones, V. B. Neculaes, R. M. Gilgenbach, W. M. White, M. R. Lopez, Y. Y. Lau, T. A. Spencer, and D. Price, Review of Scientific Instruments, vol. 75, p. 2976, 2004.

Jon05 M. C. Jones, Ph. D. dissertation, University of Michigan, Ann Arbor, 2005.

Jor07 N. M. Jordan, R. M. Gilgenbach, Y. Y. Lau, B. W. Hoff, E. J. Cruz, D. M. French, M. R. Gomez, P. Pengvanich, and J. Zier, *Proceedings of the 34th IEEE ICOPS, Albuquerque, NM* (IEEE, Piscataway, NJ, 2007), p.380.

Jor07b N. M. Jordan, Y.Y. Lau, D. M. French, R. M. Gilgenbach, and P. Pengvanich, Journal of Applied Physics, vol. 102, 033301, 2007.

Kis98 R. A. Kishek and Y. Y. Lau, Physical Review Letters, vol. 80, p. 103 1998.

Kim06 H. C. Kim, J. P. Verboncoeur, Y. Chen, and Y. Y. Lau, *Proceedings of the Seventh IEEE International Vacuum Electronics Conference*, Monterey, CA (IEEE, Piscataway, NJ, 2006), p. 359; Y. Y. Lau, J.

P. Verboncoeur, and H. C. Kim, Applied Physics Letters, vol. 89, 261501, 2006.

Lan22 I. Langmuir and K. B. Blodgett, “Currents limited by space charge between coaxial cylinders”, Physical Review, vol. 22, pp. 347-356 1922.

Lau01 Y.Y. Lau, Physical Review Letters, vol. 87, 278301 2001.

Law07 J.E. Lawler, E.A. Den Hartog, Z.E. Labby, C. Sneden, J.J. Cowan, I.I. Ivans, The Astrophysical Journal Supplement Series, 169:120-136, March 2007.

Lem88 R. Lemke, D. Voss, and L. Miner, *Materials Test Experiments Report*, October 4, 1988.

Lem99 R.W. Lemke, T.C. Genoni, T.A. Spencer, “Three-dimensional particle-in-cell simulation study of a relativistic magnetron,” Physics of Plasmas, vol. 6, num. 2, pp. 603-613, 1999.

Lem00 R. W. Lemke, T.C. Genoni, and T.A. Spencer, “Effects that limit efficiency in relativistic magnetrons,” IEEE Transactions on Plasma Science, vol. 28, issue 3, pp. 887-897, June 2000.

Lop03 M. R. Lopez, Ph. D. dissertation, University of Michigan, Ann Arbor, 2003.

Lug96 J.W. Luginsland, Y. Y. Lau, R. M. Gilgenbach, “Two-dimensional Child-Langmuir law,” Physical Review Letters, vol. 77, pp. 4668-4670, 1996. There is a mistake in this paper: The number 1 should be added to the right-hand side of Eq. (2).

Lug02 J. W. Luginsland, Y. Y. Lau, R. J. Umstattd, and J. J. Watrous, Physics of Plasmas, vol. 9, 2371, 2002.

Mar68 G.V. Marr, *Plasma Spectroscopy*, Elsevier Publishing Co., New York, 1968.

Mes89 G. A. Mesyats and D. I. Proskuvosky, *Pulsed Electrical Discharge in Vacuum* (Spinger-Verlag, Berlin, Germany, 1989).

Mil95 H. C. Miller, in *High Voltage Vacuum Insulation*, Ed.: R. V. Latham, (Academic Press, London, UK, 1995); Ch. 8, p.299.

Mil98 R. B. Miiller, “Mechanism of explosive electron emission for dielectric fiber (velvet) cathodes”, Journal of Applied Physics, vol. 84, Issue 7, pp. 3880-3889, 1998.

Mil07 R. Miller, Y.Y. Lau, and J. Booske, Applied Physics Letters, vol. 91, 074105, 2007.

Miy02 K. Miyoshi, *Surface Analysis and Tools*, NASA Report, 211815, August 2002.

Nal78 E. Nalos, “New developments in electromagnetic energy beaming”, IEEE Proceedings, vol. 55, p. 276, 1978.

Nat98 K. Natori, D. Otani, and N. Sano, “Thickness dependence of the effective dielectric constant in a thin film capacitor,” Applied Physics Letters, vol. 73, pp. 632-634, 1998.

Neu01 A. A. Neuber, L. Laurent, Y. Y. Lau, and H. Krompholz, in [Bar01], Ch. 10, p.325.

Nec03 V. B. Neculaes, R. M. Gilgenbach, and Y. Y. Lau, Applied Physics Letters, vol. 83, pp. 1938-1940, 2003.

Nec05 V. B. Neculaes, Ph.D. Dissertation, University of Michigan, Ann Arbor, 2005.

NIST http://physics.nist.gov/PhysRefData/ASD1/choice.html

NTIA http://www.ntia.doc.gov/osmhome/allochrt.pdf

Par04 K. L. G. Parkin, L. D. DiDomenico, F. E. C. Culick, “The microwave thermal thruster concept,” *AIP Conference Proceedings 702: Second International Symposium on Beamed-Energy Propulsion*, Melville, NY, pp. 418, 2004.

Pen05 P. Pengvanich, V. B. Neculaes, Y. Y. Lau, R. M. Gilgenbach, M. C. Jones, W. M. White, and R. D. Kowalczyk, “Modeling and experimental studies of magnetron injection locking,” Journal of Applied Physics, vol. 98, 114903, 2005.

Per07 T.V. Perevalov, V.A. Gritsenko, S.B. Erenburg, A.M. Badalyan, H. Wong, C.W. Kim, Journal of Applied Physics, vol. 101, 053704, 2007.

Pet98 C. W. Peters, R. L. Jaynes, Y. Y. Lau, R. M. Gilgenbach, W. J. Williams, J. M. Hochman, W. E. Cohen, J. I. Rintamaki, D. E.

Vollers, and T. A. Spencer, “Time-frequency analysis of modulation of high power microwaves by electron-beam voltage fluctuations”, Physical Review E, vol. 58, pp. 6880-6883, 1998.

Pet05 J. J. Petillo, E. M.Nelson, J. F DeFord, N. J.Dionne, and B.Levush, IEEE Transactions on Electron Devices, vol. 52, p. 742, 2005.

Pra04 R. Prather, Heating and current drive by electron cyclotron waves, Physics of Plasmas, vol. 11, p. 2349, 2004.

Poz98 D. M. Pozar, *Microwave Engineering*, (Addison-Wesley Publishing Company, 1998).

Ric23 O. W. Richardson, Phil. Mag., vol. 28, p. 633, 1914; S. Dushman, Physical Review, vol. 21, p. 623, 1923 and Review of Modern Physics, vol. 2, p. 381, 1930; W. Schottky, Z. Phys., vol. 14, p. 63, 1923 and Ann. Phys. (Leipzig), vol. 44, p. 1011, 1914.

Sar74 Sargent, Murray, M.O. Scully, and W.E. Lamb, *Laser Physics*, Addison Wesley Publishing Co., Reading, MA, 1974.

Sch98 L. Schachter, Applied Physics Letters, vol. 72, p. 421, 1998.

Sch07 J. E. Scharer, *private communication,* 2007.

Shi00 D. A. Shiffler, M. J. LaCour, M. D. Sena, M. D. Mitchell, M. D. Haworth, K. J. Hendricks, and T. A. Spencer, “Comparison of carbon fiber and cesium iodide-coated carbon fiber cathodes” IEEE Transactions on Plasma Science, vol. 28, No. 3, pp. 517-522, June 2000.

Shi01a D. Shiffler, M. Lacour, K. Golby, M. Sena, M. Mitchell, M. Haworth, K. Hendricks, and T. Spencer, “Comparison of velvet- and cesium iodide-coated carbon fiber cathodes”, IEEE Transactions on Plasma Science, vol. 29, pp. 445-451, 2001.

Shi01b D. Shiffler, M. Ruebush, M. LaCour, K. Golby, R. Umstattd, M. C. Clark, J. Luginsland, D. Zagar, and M. Sena, “Emission uniformity and emission area of explosive field emission cathodes”, Applied Physics Letters, vol. 79, pp. 2871-2873, 2001.

Shi02a D. Shiffler, M. Ruebush, D. Zagar, M. LaCour, M. Sena, K. Golby, M. Haworth, and R. Umstattd, “Cathode and Anode Plasmas in Short-Pulse Explosive Field Emission Cathodes,” Journal of Applied Physics, 1 May 2002.

Shi02b D. Shiffler, M. LaCour, M. Ruebush, K. Golby, D. Zagar, M. Haworth, T. Knowles, and R. Umstattd, “Novel Carbon Velvet Field Emission Cathode,” Review of Scientific Instruments, vol. 73, issue 12, pp. 4358-4362, December 2002.

Shi04a D. Shiffler, J. Heggemeier, M. LaCour, K. Golby, and M. Ruebush, “Low level plasma formation in a carbon velvet cesium iodide coated cathode”, Physics of Plasma, vol. 11, pp. 1680-1684, 2004.

Shi04b D. Shiffler, J. Luginsland, M. Ruebush, M. LaCour, K. Golby, K. Cartwright, M. Haworth, and T. Spencer, “Emission uniformity and shot-to-shot variation in cold field emission cathodes”, IEEE Transactions on Plasma Science, vol. 32, pp. 1262-1266, 2004.

Shi04c D. Shiffler, “Field Emission Carbon Cathode,” Patent # 6,683,399, January 27, 2004.

Shi05 D. Shiffler, T. K. Statum, T. W. Hussey, O. Zhou, and P. Mardahl, in *Modern Microwave and Millimeter Wave Power Electronics*, Eds.: R. J. Barker, J. H. Booske, N. C. Luhmann, and G. S. Nusinovich (IEEE Press, Piscataway, NJ, 2005); Ch. 13, p. 691.

Shi07 D. Shiffler, S. Heidger, K. Cartwright, R. Vaia, D. Liptak, G. Price, M. LaCour, K. Golby, “Materials Characteristics and Surface Morphology of a Cesium Iodide-Coated Carbon Velvet Cathode,” Journal of Applied Physics, vol. 103, 013302, 2008.

Tur89 R. E. Turner, *Vacuum Microelectronics* (Institute of Physics Publishing, Bristol, England, 1989).

Ums05 R. J. Umstattd, D. Abe, J. Benford, D. Gallaghar, R. M. Gilgenbach, D. M. Goebel, M. S. Litz, and J. A. Nation, in Ref. 3, Ch. 9, p. 284; R. J. Umstattd, in *Modern Microwave and Millimeter Wave Power Electronics*, Eds.: R. J. Barker, J. H. Booske, N. C. Luhmann, and G. S. Nusinovich (IEEE Press, Piscataway, 2005); Ch. 8, p. 393.

Vau93 J. R. M. Vaughan, IEEE Transactions on Electron Devices, vol. 40, p. 830, 1993.

Wha07 D. R. Whaley, R. Duggal, C. M. Armstrong, C. L. Bellew, C. E. Holland, C. A. Spindt, “TWT Operation with Low-Voltage Field Emitter Array Cathode”, IEEE IVEC, May 2007.

Whe58 N. R. Whetten and A. B. Laponsky, Journal of Applied Physics, vol. 30, p. 432, 1958.

Whi05 W. M. White, Ph. D. dissertation, University of Michigan, Ann Arbor, 2005.

Wil07 Time Frequency Toolbox developed by W.J. Williams and licensed by Quantum Signal, LLC (http://www.quantumsignal.com), 2007.